Towards Integrated Single-Photon Sources Exploiting Inhomogeneous Spectral Properties of the Silicon-Vacancy Center in Nanodiamonds

DISSERTATION

Dissertation
zur Erlangung des Grades
des Doktors der Naturwissenschaften
der Naturwissenschaftlich-Technischen Fakultät
der Universität des Saarlandes

von

Sarah Christina Barbara Lindner

Saarbrücken, 2018

Tag des Kolloquiums: 08.11.2018

Dekan: Prof. Dr. Guido Kickelbick

Berichterstatter: Prof. Dr. Christoph Becher, Prof. Dr. Christophe Couteau

Vorsitz: Prof. Dr. Rolf Pelster

Akad. Mitarbeiter: Dr. Christoph Pauly

Abstract

Due to their favorable optical properties, silicon-vacancy (SiV) centers have recently emerged as promising candidates for the realization of reliable on-demand single photon sources. Such non-classical light sources are key to applications in quantum computing, quantum cryptography, and quantum metrology. In the latter single photon sources are a prerequisite for a quantum-based redefinition of the candela.

This thesis contributes to the development of single photon sources with a high applicability in practice through researching SiV centers along two main approaches: First the luminescence properties of a large set of nanodiamonds containing SiV centers are established. This yields a novel strongly inhomogeneous distribution yielding two clusters with regard to the center wavelengths and the linewidth of the zero-phonon-line at room temperature. One of these clusters is consistently explained by strain in the diamond lattice, the other might be due to modified SiV centers.

Second, we work towards the goal of developing integrated high-intensity and narrow linewidth single photon sources exploiting the investigated SiV center properties. Using pick-and-place methods, SiV centers are coupled to two different nano-structures. By placing a nanodiamond on top of a vertical-cavity surface emitting laser (VCSEL), we attempt to realize a controllable hybrid-integrated single photon source. By coupling SiV centers with plasmonic nano-antennas we aim to enhance their photoluminescence intensity. We are able to report significant progress towards this goal.

Our contributions add momentum to the research of integrated, high-intensity, narrow linewidth single photon sources, to the development of novel calibration standards and ultimately to the universal adoption of the quantum candela.

Zusammenfassung

Auf Grund günstiger optischer Eigenschaften sind Silizium Farbzentren (SiV) vielversprechende Kandidaten für die Realisierung von Einzelphotonenquellen. Solche nicht-klassischen Lichtquellen sind für Quantencomputer, Quantenverschlüsselung und Quantenmetrologie essentiell. Für letztere bilden Einzelphotonenquellen eine Schlüsseltechnologie auf dem Weg zu eine quanten-basierte Neudefinition der SI-Basiseinheit Candela.

Diese Arbeit verfolgt zwei Ansätze um die Entwicklung von Einzelphotonenquellen mit praktischer Bedeutung voranzutreiben: Im ersten Ansatz werden die Lumineszenzeigenschaften einer großen Menge von Nanodiamanten welche SiV Zentren enthalten etabliert. Im Zuge dessen wird eine bisher unbekannte, stark inhomogene Verteilung etabliert, die in zwei Cluster bezüglich der Zentralwellenlänge und Linienbreite der Nullphononenlinie bei Raumtemperatur unterteilt ist. Eines dieser Cluster wird mit Spannungen im Diamantgitter erklärt, das andere könnte aus modifizierten SiV Zentren bestehen.

Im zweiten Ansatz arbeiten wir an der Entwicklung von integrierten Einzelphotonenquellen mit hoher Intensität und geringer Linienbreite basierend auf den untersuchten SiV Eigenschaften. Mittels "pick-and-place" Methoden werden SiV Zentren an verschiedene Nanostrukturen gekoppelt. Durch das platzieren auf einem Oberflächenemitter (VCSEL) versuchen wir eine kontrollierbare hybrid-integrierte Einzelphotonenquelle zu realisieren. Durch die Kombination von Nanodiamanten mit plasmonischen Nanoantennen versuchen wir die Fluoreszenzintensität von enthaltenen SiVs zu verbessern. Es wurden signifikante Fortschritte in Bezug auf beide Ziele erreicht.

Unsere Arbeit trägt zur Entwicklung integrierter Einzelphotonenquellen mit hoher Intensität und geringer Linienbreite bei. Dadurch leisten wir einen Beitrag zu Entwicklung neuer Kalibrierungsstandards und damit zur Einführung des Quantencandela.

Acknowledgements

First of all, I want to thank my supervisor, Christoph Becher, for the opportunity of writing my PhD thesis performing research on the topic of quantum optics. I owe him my utmost gratitude for his support especially in times when my mental health complicated the work on this thesis.

I would like to offer my special thanks to Christophe Couteau, the second examiner of this thesis.

This work would not have been possible without the collaboration with the group of Anke Krueger, especially with Andreas Muzha, who performed the wet-milling. This crucial step yielded the extensive data collection reported in this thesis.

I cannot express in words how thankful I am for the help of Christoph Pauly, who is a master in performing tricky pick-and-place processes. Without him, all nanodiamonds would probably still rest on their original substrate. More often than not discussions with him yielded new ideas to tackle technical problems due to his background in material sciences.

Special thanks to Nancy Rahbany. It was always interesting and very fruitful to work with her on coupling nanodiamonds to her double bowtie antenna structures.

I wish to acknowledge the help of the group of Matthias Schreck and especially Stefan Gsell for providing this work both with CVD-grown nanodiamonds and with iridium coated substrates.

I want to thank Adam Gali for providing the theoretical calculations which put our experimental results of the wavelength shift in an established context.

I am happy to have had the opportunity to work in the SIQUTE project and to experience an international exchange of ideas. I want to thank all affiliated people.

I am very grateful for the guiding help of Janine Riedrich-Möller, who was of guiding help during the start of my PhD and never tired of running downstairs to the lab to help me with peculiar problems of the setup. Furthermore, I would also like to thank Christian Hepp and Carsten Arendt, for their help with technical challenges. I want to express my special thanks to my office colleague Philipp Fuchs and lab colleague Alexander Bommer for sharing both fun moments and lousy moments. I also want to thank the whole Quantum Optics group for their support.

I owe special thanks to Elke Huschens, who solved complex bureaucratic and organizational problems in the blink of an eye. I also want to thank the workshop team who created specialized bits and pieces for the lab setup.

I want to thank my friends near and far for cheerful and fulfilling times beyond physics.

I am grateful to my family for their support during my studies. I want to thank my sister for her moral support, my mum who kindled my diverse curiosity and my dad who introduced me to the great fascination of science and technology.

Finally I want to thank my partner Michael for his never-ending support in very demanding times. I don't know what I would have done without this pillar of strength.

Contents

List of Figures

List of Tables

1 Introduction

> "Every competent physicist can "do" quantum mechanics, but the stories we tell ourselves about what we are doing are as various as the tales of Sheherazade, and almost as implausible."
>
> David J. Griffiths

The International System of Units (SI, abbreviated from the French Système international d'unités) emerged in the late 18^{th} century as a coherent metric system of measurement with rationally related units and simple rules for combining them [1]. Since its inception it was improved and augmented continuously in an ongoing effort to accommodate continued scientific and technological progress. The current SI system is comprised of seven base units: The kilogram (kg), the second (s), the Ampere (A), the Kelvin (K), the mole (mol) and the candela (cd). Currently a redefinition of four of the base units (kilogram, mole, Kelvin, Ampere) in terms of fundamental constants is under way [2, 3]. The proposed change will improve the definitions of these base units to make them easier to realize experimentally, particularly for the measurement of electrical quantities [4]. It will also eliminate the last remaining base unit definition which relies on a historic material artifact, the international prototype of the kilogram. As a result all base units will, for the first time, be tied to one or more fundamental constants of nature.

As these developments are put into motion, similar discussions regarding the SI base unit for luminous intensity, the candela, have emerged. It has been suggested that it can be improved by leveraging recent advances in classical radiometry and photometry as well as the development of novel quantum devices and techniques [5].

At the time of writing the definition of the candela read:

> The candela is the luminous intensity, in a given direction, of a source that emits monochromatic radiation of frequency $540 \times 10^{12}\,\mathrm{Hz}$ and that has a radiant intensity in that direction of $638^{-1}\mathrm{W\,sr^{-1}}$.

Traditional applications relying on this definition in conjunction with accurate photometric and radiometric measurements are light design, manufacturing and use of optical sources, detectors, optical components, colored materials and optical radiation measuring equipment [4]. Such devices operate in the classical regime of optical radiation where high flux levels dominate. Here primary optical radiation scales for sources and detectors are generally based on cryogenic radiometry establishing a link to the SI units of electricity [6]. Other calculable sources such as synchrotron and blackbody radiators can serve as primary source scales in the ultraviolet and deep-UV regions by establishing traceability to SI units of thermometry, electricity and length [4, 5].

Scaling down to the quantum world of radiometry is associated with a loss of measurement accuracy. In this regime dedicated photon counting techniques are required to deal with the challenge of low flux levels. Since they rely on counting photons directly, in principle they provide efficient and traceable measurements of photon flux and improved associated uncertainties. For high-accuracy absolute radiometry in this regime, predictable single or quasi-single photon sources and photon detectors as well as associated new quantum-based calibration methods and standards are called for. To promote the development of such technologies a reformulation of the candela has been proposed in terms of *countable* photon units [3–5, 7]. Here we emphasize the distinction between *countable* and *calculable* sources of photons, the latter being available as blackbodies or synchrotron radiators.

A straightforward quantum-based reformulation has been suggested based on [4, 5]:

$$P = nh\nu, \tag{1.1}$$

where the radiant intensity per steradian $P = 638^{-1}\mathrm{W\,sr^{-1}}$ in a given direction and the photon frequency $\nu = 540 \times 10^{12}\,\mathrm{Hz}$ are assumed to be exact with their numerical values inherited from the present definition of the candela. The anticipated proposed changes to the SI system will define Planck's constant $h = 6.626\,070\,15 \times 10^{-34}\,\mathrm{J\,s}$ as an exact numerical constant [8]. As a consequence the number of photons per second per steradian in a candela n becomes a constant defined as:

$$n = \frac{P}{h\nu} \approx 4.091\,942\,9 \times 10^{15}\,\mathrm{counts\,s^{-1}\,sr^{-1}}. \tag{1.2}$$

Given this definition of the radiant intensity of a candela in terms of countable photons, a possible formulation of the quantum candela could read [5]:

> The candela is the luminous intensity, in a given direction, of a source that emits photons of frequency 540×10^{12} Hz at a rate of $4.091\,942\,9 \times 10^{15}$ photons per second per steradian in that direction.

This definition would incur a deviation of 0.0014 % from the current value of the candela. This is an acceptable change, taking into account the fact that current experimental realizations of the candela are limited to uncertainties of 0.02 % [5]. Proposals such as this are regularly reviewed by the Consultative Committee for Photometry and Radiometry ensuring that the current best measurement practices and existing as well as emerging needs of the user community of the candela are met [4].

While a proposed formulation of a quantum-candela can be considered a small change to the SI system, a shift towards quantum based radiometric SI units it likely to become a critical enabler driving the development of accurate and traceable measurement methods on the single-photon level. In order for the definition of the quantum-candela to have practical meaning, photon counting detectors are required capable of accurately resolving single photons. To ensure proper calibration of such devices, reliable deterministic single photon sources are key. As novel instruments and associated calibration standards emerge, our ability to work with individual photons in a wide range of applications is expected to improve [9–12]. The quest for single photon sources is supported by large research projects such as “Single-Photon Sources for Quantum Technology" funded by the European Metrology Research Program [7, 13].

Advances in radiometry are particularly important for fields like quantum communication and quantum computing. They are heavily reliant on deterministic reliable single photon sources and well-calibrated detectors. At the same time users of these technologies have developed into major driving forces of research related to single photon sources [12, 14]. Amongst others, some well known applications include quantum key distribution [15–17] or transmission in a quantum network [18–20].

At present several candidates for on-demand single photon sources are available, which we shortly mention here. One possibility consists of atennuating a laser beam such that the mean number of photons in the beam becomes close to one [10, 21, 22]. However, the mean photon number cannot be controlled perfectly and a non-zero probability remains that multiple photons are present in the beam simultaneously.

Quasi-single photon states can be realized using photon-pairs consisting of a signal and an idler photon. Pairs are created when a photon interacts with a non-linear optical medium in a process called spontaneous parametric down-conversion (SPDC) [13, 23–27]. The deciding feature of the process is the strong time-correlation between signal and idler photons. If both photons are injected into individual optical paths, a detection event in one of the paths heralds the existence of a photon in the other path. SPDC pairs can thus be used to construct single photon sources. Unfortunately, due to the poor efficiency of the SPDC process, the probability of generating pairs is unfavorable [4, 28]. Thus efforts have been undertaken to improve the efficiency [28–30].

Single photons can be obtained as a result of radiative transitions between energy levels of single atoms or molecules trapped in an optical cavity [31]. While these sources have desirable properties such as high collection efficiency, the practical usefulness is limited due to being technologically demanding. Amongst others a high vacuum is needed to operate these sources [4].

In contrast to that, single photon sources based on solid-state systems combine the outstanding optical properties of atoms with the convenience of operation in ambient pressure and a high scalability of the solid-state host system [32–34]. Challenges include variability between photons from different emitters and homogeneous linewidth broadening that gives rise to photon distinguishability from the same emitter. Furthermore, the extraction of photons from emitters in solid-state host materials can be non-trivial. These challenges are subject of ongoing research. Among the best known solid-state quantum emitters are quantum dots and color centers, the latter of which will be discussed later. Quantum dots emit photons by recombination of electron-hole pairs created by optical excitation or via an electric current [35, 36]. The choice of semi-conducting material determines the electronic structure of the system and thus the characteristics of the emitter. Over the past decade, efforts to engineer solid-state single photon emitters have expanded beyond the originally studied colour centres and quantum dots to include two-dimensional materials, carbon nanotubes and other solid-state host materials [34].

For a wide range of single photon sources, significant progress has been made towards improving purity, indistinguishably and collection efficiency [33, 37–40].

As it stands, a single photon source suitable for the calibration of single-photon detectors remains difficult to realize [41]. Ideally, a standard single photon source should be emitting with a quantum efficiency of 100 % indicating that the entire excitation energy is transformed into radiation without losses. At the same time multiple photon events should be completely supressed to the point that single photons are emitted with a probability of one. Subsequently emitted photons should be collected with perfect efficiency.

Very recently, another interesting direction has been explored, identifying color centers in nanodiamonds involving silicon [42, 43] and nitrogen [44] as promising candidates for the realization of standard single photon sources [41, 45]. In particular it was shown that it is possible to absolutely calibrate single photon sources using a classical detector and a calibrated spectrometer, establishing an unbroken traceability chain to the SI system. The photon flux of the source can be controlled via the settings of the pump laser repetition rate. In this way a direct link between the high photon flux levels of the classical regime and low photon flux levels in the quantum world has been formed. For the nitrogen vacancy center a photon flux rate of $\approx 1.4 \times 10^5$ photons per second was recorded.

In this thesis we continue researching the potential of color centers in nanodiamonds as single photon sources. More precisely, we focus on the silicon-vacancy center. In doing so we aim to add momentum to the development of single photon source as high-accuracy calibration devices and subsequently, to the development of photon counting detectors and the adoption of the quantum-candela.

The SiV center in diamond is an ideal candidate for single photon calibration purposes. It is a very efficient and stable narrow linewidth emitter, producing single photons with high intensity. Conveniently, SiV centers operate at room temperature under ambient pressure and hence do not require overly sophisticated experimental setups. As an alternative to hosting SiV centers in bulk diamond, they can be implanted in nano-sized diamond grains offering increased collection efficiency. Grains containing individual SiV centers can be identified and preselected.

In this thesis we synthesize nanodiamonds hosting SiV centers using a variety of different techniques. Chemical vapor deposition, high-pressure, high-temperature synthesis as well as wet-milling methods are used to produce a sizable set of samples. To investigate the samples, i.e. to study the optical properties of embedded SiV centers we rely on optical excitation. In particular, confocal microscopy is used to collect emitted fluorescent single photons. An attached spectrometer or a Hanbury-Brown and Twiss setup offer further insights into the properties of the SiV center as a single photon source.

Our work can roughly be subdivided into two larger explorations. The first revolves around charting the luminescence properties of a large set of nanodiamonds and their hosted emitters, allowing us to establish distributions of selected SiV center properties. This yields a novel strongly inhomogeneous distribution yielding two clusters with regard to the center wavelengths and the linewidth of the zero-phonon-line at room temperature. One of these clusters is consistently explained by strain in the diamond lattice, the other might be due to modified SiV centers. To our knowledge, our efforts result in the largest coherent examination of SiV centers in nanodiamonds to date. In contrast to that the second exploration focuses on individual nanodiamonds and our attempts to relocate them to different nanostructures in order to achieve a coupling between SiV centers and the host structure. First we attempt to realize a controllable hybrid-integrated single photon source by placing a nanodiamond containing SiV centers on top of a vertical-cavity surface emitting laser (VCSEL). Furthermore, we combine nanodiamonds with plasmonic nanoantennas in order to enhance the photoluminescence intensity of the contained SiV centers. To this end, a large range of samples was investigated in the search for well-suited nanodiamonds hosting single SiV centers. Figure 1.1 illustrates the magnitude of the effort.

The thesis is structured as follows: Chapter 2 introduces the reader to color centers and diamond as a host material. A discussion of SiV centers restricted to their most important luminous properties is presented. Chapter 3 familiarizes the reader with the essential experimental setup and methods deployed in this thesis to study SiV center luminescence. Various relevant methods of synthesizing sample nanodiamonds containing SiV centers are presented and discussed in Chapter 4. Chapter 5 is dedicated to the important topic of gauging the quality of fabricated samples. The results of charting the luminous properties of our nanodiamonds samples is presented in Chapter 6. Our attempts of coupling nanodiamonds hosting SiV centers to two different nanostructures is investigated in Chapter 7. Finally we discuss the overall findings of this thesis in Summary and Conclusions.

Some of the results presented in this thesis (parts of Chapter 4, Chapter 5, Chapter 6) have been published in [46] by S. Lindner, A. Bommer, A. Muzha, A. Kruger, L. Gines, S. Mandal, O. A.Williams, E. Londero, A. Gali, and C. Becher. In this publication, nanodiamond production was performed by A. Muzha, A. Kruger, L. Gines S. Mandal, and O. Williams, the theoretical framework of strain in the

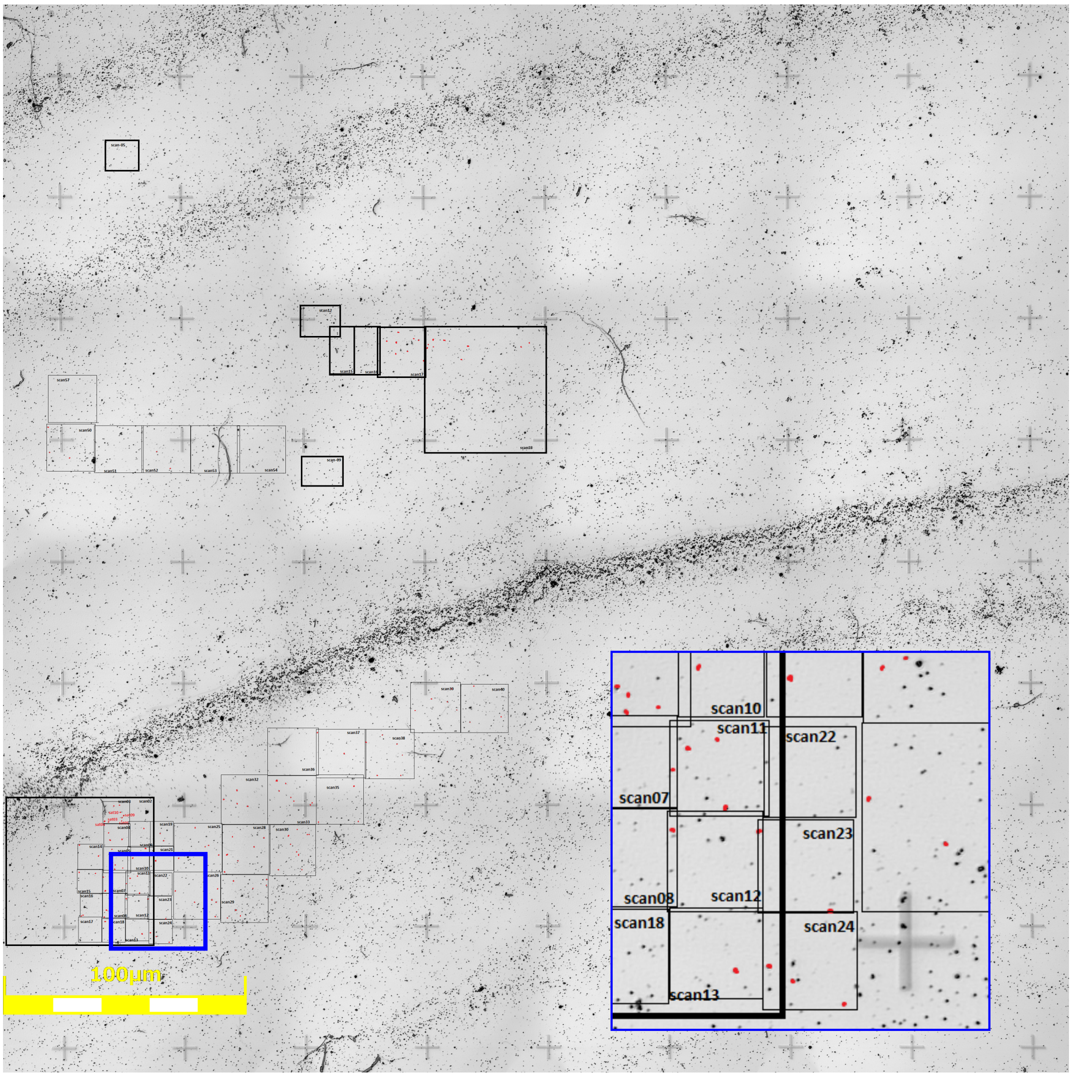

Figure 1.1: An exemplary image of a sample surface carrying nanodiamonds. What appears to be black dust are enormous amounts of individual nanodiamonds. Various black squares indicate areas that were scanned in search of nanodiamonds suitable for coupling. The blue square zooms in on a cluster of overlapping scans revealing the individual nanodiamonds present. The luminescence properties of all nanodiamonds marked red were individually investigated.

diamond lattice was established by E. Londero and A. Gali. The spectroscopic measurements were performed by A. Bommer and the author of the thesis.

2 Silicon Vacancy Centers in Diamond

In the following we introduce color centers, i.e. optically active point-defects present in a diamond lattice. We focus on color centers combining silicon impurities and lattice vacancies forming the silicon-vacancy center (SiV center). We start by presenting the most important properties of diamond and emphasize its suitability as a host for optical applications with color centers. A classification of diamond with respect to defects and impurities as well as crystallinities serves as a preparation for the introduction of methods to synthesize diamonds containing SiV centers presented in Chapter 4. Finally, we discuss SiV centers in detail and focus on their most important optical properties which make them ideal candidates for realizing reliable single photon sources at room temperature. In particular, we zoom in on the key features of its luminescence spectrum, the zero-phonon-line and the phonon side band. Our discussion partially follows the presentation in [47–51].

2.1 Diamond as a Host Lattice

Diamond is a metastable modification of carbon which is stable under ambient pressure at room temperature [52]. Carbon atoms form strong sp^3-bonds with each other in a tetrahedral arrangement of neighboring atoms. For an extensive introduction of carbon bonds refer to Chapter 5. The resulting sp^3-hybridized lattice is of exceptional mechanical stability, making diamond the hardest known material [53]. The crystal structure can also be interpreted as a face-centered cubic (fcc) lattice with two carbon atoms in the primitive Bravais cell, situated at $(0,0,0)\ a$ and $(\frac{1}{4},\frac{1}{4},\frac{1}{4})\ a$ with $a = 3.567\,\text{Å}$ denoting the lattice constant [54]. Figure 2.1 illustrates the structure.

The valence and conduction bands of diamond are separated energetically by a large direct band gap of 7.3 eV while its indirect band gap amounts to 5.5 eV [56, 57]. As a result diamonds are transparent for light of all wavelengths larger than 230 nm [58]. This transparent quality makes diamond an ideal host material for various optically active lattice defects or impurities. These induce a wide range of discrete energy levels situated in the sizable band gap. The absorption of optically active impurities or impurity complexes gives rise to the observed variety of colors

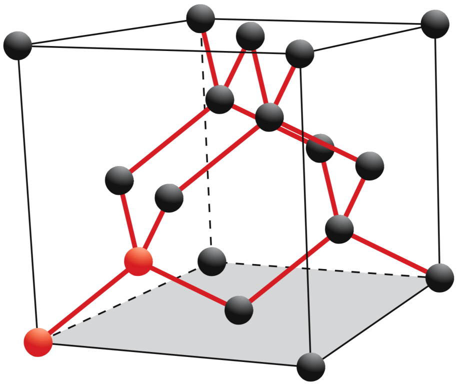

Figure 2.1: Face-centered cubic diamond lattice. Note the tetrahedral arrangements of carbon atoms [55]. Red dots illustrate the two carbon atoms in the primitive Bravais cell.

in diamonds, thus these impurities are commonly termed color centers [48]. Due to the exceptional mechanical stability of diamond, color centers too are very stable mechanically, another important property favorable for optical applications.

A property of diamond, detrimental to some optical applications, is its large refractive index with values of 2.49 at 360 nm and 2.4 at 800 nm respectively [59]. Thus, a portion of the light escaping from the diamond is reflected back into it, effectively reducing the efficiency of light extraction, see Figure 2.2a. If nanodiamonds smaller than the wavelength of the light to be collected are used, internal reflection is suppressed and the extraction efficiency can be increased as illustrated in Figure 2.2b [60]. As a result, the quantum yield defined as the ratio between the number of photons emitted by the SiV center to the number of photons absorbed by the diamond is enhanced.

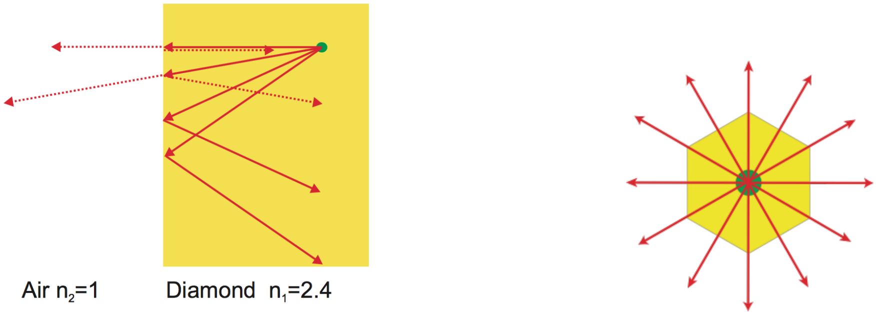

(a) (b)

Figure 2.2: (a) Light from a fluorescent emitter inside the diamond (green dot) undergoes reflection at the diamond-air interface. Figure reproduced with permission from [48]. (b) Nanodiamond smaller than fluorescence light wavelength, reflection is suppressed.

2.2 Classification of Diamond

Two major approaches for classifying diamond are commonly encountered. First, classification according to the presence or absence of certain impurities or impurity complexes. Second, classification based on different diamond crystallinities observed in the diamond. In the following both classification systems are briefly introduced.

2.2.1 Classification by Impurities

Impurities or complexes of impurities in the diamond lattice can be optically active and thus change the optical properties of diamond. Most strikingly perhaps is the appearance of color in otherwise colorless diamond due to a sufficient concentration of such defects. Using IR absorption spectroscopy the degree of nitrogen impurities can be determined. It is used to subdivide diamonds into distinct groups named Type I and Type II [61, 62]. The groups are further subdivided as follows:

- Type Ia: With a nitrogen concentration of up to 3000 ppm, most natural occurring diamonds belong to this group [59]. Nitrogen appears arranged predominantly in aggregate clusters forming complexes of impurities. These complexes are optically active, absorbing light in the blue range of the visible spectrum. Consequently Type Ia diamonds often exhibit a yellow to brownish coloration.
- Type Ib: With concentrations of up to 500 ppm, nitrogen atoms appear predominantly in isolation, replacing individual carbon atoms in the diamond lattice. In addition to absorbing visible blue light, green is being absorbed as well. Type Ib diamond thus exhibits intensified yellow or brownish coloration. While only 0.1 % of naturally occurring diamond fall into this class, almost all synthetic diamonds created using the high-pressure, high-temperature (HPHT) method are of Type Ib [59].

While Type I diamond exhibits an appreciable concentration of nitrogen, Type II diamonds lack nitrogen entirely. Type II diamond is divided into two subgroups according to the presence or absence of boron as follows:

- Type IIa: Can be considered pure as they lack optically active defects [63]. They thus are colorless. Up to 2 % of naturally occurring diamond and most diamonds synthetically created using the chemical vapor deposition (CVD) method are of Type IIa [59].
- Type IIb: Contains appreciable concentrations of boron atoms replacing individual carbon atoms in the diamond lattice. Boron defects are optically active absorbing visible light ranging from red to yellow. Depending on the Boron concentration blue to gray colorations are observed. Furthermore, diamond

> changes from an insulator to an efficient p-type semiconductor in the presence of boron impurities [64].

We remark that for many modern applications of diamonds the presented “classic" categorization of diamond is insufficient. In these cases a precise quantification of the concentration and nature of various relevant impurities is called for [65, 66].

In this section we also briefly touched upon the CVD and HPHT methods, two approaches to synthetically produce diamonds. Both are relevant for this thesis and are explained in detail in Chapter 4.

2.2.2 Classification by Crystallinity

Up until now, the discussion assumed that diamond forms a lattice consisting of one giant single crystal. However, other crystallinities are possible and can be used to classify diamond. They range from mono or single crystals to polycrystalline, nanocrystalline or even ultra-nanocrystalline diamond films [67]. This classification is particularly useful for synthesized diamond as will be discussed in Chapter 4. Table 2.1 summarizes the different sizes of diamonds or diamond films which can be achieved using variations of the CVD method. In the context of this thesis it is not necessary to distinguish nanodiamonds based on the size of their crystallinities, it suffices to distinguish between mono- and polycrystalline nanodiamonds.

Diamond films consist of isolated diamond grains of random orientation with sp^2 hybridized grain boundaries and graphite-like inclusions [47]. Carbon present in non-diamond phases, e.g. graphite or amorphous carbon gives rise to detrimental light absorption while crystal boundaries lead to increased scattering losses. As the size of diamond crystallites get smaller, the ratio of non-diamond carbon to diamond carbon increases. Thus losses are most pronounced for the smallest grain diamond films.

Crystallinity	Grain size
monocrystalline	arbitrary
polycrystalline	50 nm to 10 µm
nanocrystalline	10 nm to 50 nm
ultra-nanocrystalline	$<$ 10 nm

Table 2.1: Classification of diamonds synthesized using CVD [50].

2.3 The Silicon-Vacancy Center

A color center is an optically active point-defect in a crystal lattice, capable of absorbing and emitting light. Defects can consist of one or several vacant lattice sites, foreign atoms replacing lattice atoms or a combination thereof. If the presence of a defect induces discrete energy levels located in the band gap of the host material, the color center can be interpreted as its own quantum system. In other words, the color center can be viewed as a single isolated and localized artificial atom embedded in a host matrix. As such it is able to absorb light and emit single photons by means of fluorescence.

Compared to alternative single photon sources like single atoms [31], ions [68] or individual quantum dots [35, 69], color centers offer a couple of advantages. As a result of the high mechanical stability of the host lattice color centers exhibit increased photo-stability, in particular compared to organic molecules as light sources. Furthermore the host lattice offers protection of color centers from detrimental interactions with aggressive free molecules [70]. Lastly, color centers can be handled and investigated at room temperature and ambient pressure, thus significantly reducing the experimental sophistication necessary to study them.

Of particular interest are color centers as single photon sources when hosted in diamond. With its transparency, exceptional stability and minimal phononic interactions at room temperature the diamond lattice is an ideal host matrix for color centers [71, 72]. While more than 500 different color centers in diamond are documented, only a small fraction has been investigated with respect to their properties as single photon sources [59]. For an in-depth review of color centers and their versatile applications see [73, 74]. The two arguably most prominent examples of well-studied color centers are vacancy centers featuring nitrogen and silicon [75–77].

The silicon-vacancy center (SiV center) in diamond and its properties are at the center of this thesis. The SiV center has been established as a reliable single photon source at room temperature. It shows very narrow emission lines with record count rates up to mega-counts-per-second [42]. The emission of indistinguishable photons and the optical access of electronic spin states have been demonstrated [78–81], hinting at the possibility of deploying SiV centers as spin-qubits.

A silicon-vacancy center is formed in a diamond lattice by substituting two carbon atoms by a silicon atom and a nearby empty lattice site respectively. The silicon atom occupies its energetically optimal position by sitting in-between two lattice sites. This is called “split-vacancy” configuration and induces a D_{3d} symmetry with the two vacancies and the impurity aligned along the $\langle 111 \rangle$ diamond axis [82], see Figure 2.3.

The SiV center is known to occur in two different charge states. The first is the neutral state or SiV^0 with a zero-phonon transition at 1.31 eV (946 nm). It is associated with a $S = 1$ ground state [83]. The second state is the negatively

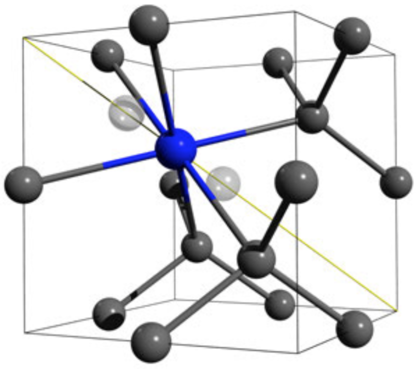

Figure 2.3: Crystal structure of the SiV center embedded into the diamond lattice: The silicon atom (blue sphere) sits in between two vacant lattice sites (white spheres) forming a "split-vacancy" configuration aligned along the $\langle 111 \rangle$ crystallographic axis (yellow line). Figure reproduced with permission from [47].

charged state SiV^- where the silicon-vacancy center recruited an additional free electron. It exhibits a zero-phonon transition at 1.68 eV (738 nm). Its ground state has been determined as a $S = \frac{1}{2}$ state [82, 84]. Due to its outstanding brightness and the location of the zero-phonon-line in the visible range of the spectrum, this thesis focuses on the negatively charged SiV center. For convenience we drop the charge distinction from now on and refer to SiV^- centers simply as SiV centers.

SiV centers are synthesized using CVD in nanodiamonds and single-crystal diamond films [85], see Chapter 4 for details. It is also possible to directly implant silicon atoms into diamond. After the implantation, high temperature annealing must be used to animate present lattice vacancies to recombine with silicon impurities in order to form split-vacancy SiV centers [84, 86].

In the following sections we detail the most important luminescence properties of SiV centers in diamond. For a comprehensive review we refer to [47, 48] and references therein.

2.3.1 Luminescence properties

The silicon-vacancy center as a quasi-atomic system is capable of absorbing and emitting light. When a ground state electron absorbs a photon of appropriate energy, it is promoted to a discrete higher-energy excited state located within the band gap of the diamond host matrix. Reversing this excitation relaxes the electron back down to the ground state while emitting a so-called fluorescent photon, accounting for the energy difference between excited and ground state. This transition is spin-allowed, limiting the life times of excited states to nanoseconds and thus promoting rapid relaxation and associated fluorescence [87].

Fluorescence is directly linked to the electronic structure of the SiV center. A qualitative depiction of its most important electronic states is given in Figure 2.4, a comprehensive discussion is found in [49, 51, 87]. Since optical transitions are associated with well-defined energies it follows that photoluminescence spectroscopy is suitable to study them using a laser to optically excite the SiV center. In the context of this thesis, optical above-resonant excitation is the method of choice, in particular, when used in conjunction with a confocal photoluminescence setup which will be discussed in Chapter 3. If the excitation energy exceeds the energy of the lowest excited state, electrons are promoted to higher electronic and vibrational states. Conveniently, these states relax rapidly towards the lowest excited state in non-radiative processes [87]. Once the lowest excited state is reached, a fluorescent transition to one of the ground state levels can follow. It has been shown that above-resonant excitation is feasible for excitation energies ranging from 1.75 eV to 2.55 eV (about 480 nm to 700 nm) [88–90]. If the excitation energy is chosen too high, however, the SiV center is ionized. This is unfavorable, since electrons escaping to the diamond conduction band do no longer induce fluorescence. Ionization may be reversed if an SiV center manages to capture a free electron from the conduction band. This charge state conversion is believed to be linked to fluorescence intermittence, describing so-called blinking SiV centers [91, 92].

The fluorescence spectra of SiV centers typically show two prominent features: A narrow zero-phonon-line and a weak phonon side band. The former is connected to fluorescent photons associated with a purely electronic transition while the latter involves vibrational transitions involving electron-phonon interactions. The phonon side band is typically shifted to higher wavelengths, i.e. lower energies, with respect to the zero-phonon-line. The resulting energy deficit can be explained by phonons being created during the relaxation of higher vibrational states. A shift in the opposite direction can also be observed in rare cases if preexisting phonons are absorbed during the relaxation process [93].

The relative strength of the zero-phonon-line and the phonon side band is influenced by electron-phonon coupling. Phonons can either originate locally, i.e. directly connected to the SiV center, or delocalized connected to lattice vibrations. In the following we discuss localized phonon modes. For a discussion of delocalized modes we refer the reader to [94].

When a color center is excited, its charge distribution changes. As a result, the equilibrium positions of all particles involved in the color center shift leading to slight changes in color center geometry. Naturally, the combined changes of charge distribution and geometry of the color center also affect the positions of surrounding atoms of the host lattice. Similarly, if the excited state relaxes back to the ground state, the process occurs in reverse. Thus, due to differing atomic arrangements for ground and excited states, the periodic emission and absorption of photons is accompanied by lattice vibrations, i.e. phonons. In other words, the electron-phonon interaction couples the motion of the lattice and electronic transitions of a

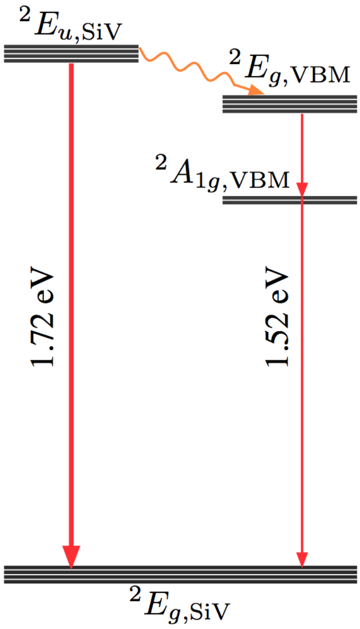

Figure 2.4: Electronic structure of SiV centers in diamond according to Gali and Maze [87]. The energy of the optical transition from the $^2E_{u,SiV}$ excited state to the $^2E_{g,SiV}$ ground state (thick red arrow) is calculated to be 1.72 eV. It is in approximate agreement with the experimentally observed value of 1.68 eV (738 nm). Additional long-lived shelving states $^2E_{g,VBM}$ and $^2A_{1g,VBM}$ can be reached from $^2E_{u,SiV}$ via a non-radiative transition (orange arrow) and parity-forbidden transitions (thin red arrows). Figure courtesy of [51].

color center [95, 96].

We now give a more detailed discussion of the electron-phonon interaction in SiV centers. Here we assume that only one dominant vibrational mode couples to the color center which is a strong assumption. In general it is believed that in a solid state host matrix a discrimination between the modes of the undisturbed lattice and quasi-local impurity-induced modes is appropriate [94, 96, 97]. Furthermore, various mechanical properties such as stress in the lattice are reported to affect phonon energies [98]. In addition, electron-phonon interactions and thus phonon side band features are believed to depend strongly on various local properties of color centers [99, 100]. Thus it is possible to encounter complex varying phonon side band features from one SiV center to the next. For a more detailed discussion of these effects we refer the reader to [47, 48] and references therein.

Our discussion follows the argumentation of Davies [95] assuming that vibrational modes can be viewed as oscillations of nuclei between their equilibrium coordinates associated with the electronic states. As a result the electronic ground state energy can be written as a harmonic oscillator potential as:

$$V_g = \frac{1}{2}m\omega^2 Q^2, \tag{2.1}$$

where ω denotes the frequency of the mode, m is the nuclei mass and Q the displacement from equilibrium. The excited state potential likewise can be written as

$$V_e = V_0 + aQ + \frac{1}{2}m\omega^2 Q^2 + bQ^2. \tag{2.2}$$

Here V_0 denotes the purely electronic energy. The term aQ denotes the linear nuclear displacement of the excited state configuration with respect to the ground state equilibrium where $Q = 0$ holds. The quadratic term bQ^2 refers to the vibrational frequency shift due to a redistribution of charge between the electronic states. Figure 2.5 illustrates ground and excited state potentials V_g and V_e and how they are displaced from each other.

Grey shaded functions illustrate eigenfunctions of the harmonic oscillator associated with vibrational states. Their quantum numbers are denoted n and n' for ground and excited state respectively. If $n = n'$ for a transition between ground and excited state, vibrational modes do not change signaling a zero-phonon-line transition. Note that according to the Frank-Condon principle [101] absorption and emission of photons and resulting changes in the electronic distributions are much faster than the vibrations of the surrounding nuclei. Thus optical transitions in Figure 2.5 occur vertically.

In Figure 2.5 an electron is excited from vibrational level $n = 0$ of the ground state to a higher vibrational level $n' = 2$ of the excited state. From there it quickly relaxes down to the vibrational state $n' = 0$ in a non-radiative process. In contrast, the following transition from $n' = 0$ to $n = 3$ occurs via the emission of a photon. In the Condon approximation the most probable optical transition maximizes the overlap between the vibrational eigenfunctions of source and destination states. Such a transition is shifted with respect to the ZPL and is associated with the phonon side band. The observed red-shift of the phonon side band is directly tied to the phonon energy with higher order sidebands showing multiples of this energy.

Given the fact that optical transitions are vertical in the Frank-Condon scheme, the displacement between ground and excited state potentials determines the probability for phonon side bands to occur. The displacement in turn is proportional to the linear electron-phonon coupling. A measure suitable to quantify this coupling is the Huang-Rhys factor S given by

$$S = -\ln \frac{I_{ZPL}}{I_{ZPL} + I_{PSB}}, \tag{2.3}$$

where I_{ZPL} and I_{PSB} are the intensities of the ZPL and the phonon side band respectively. Note that S can be interpreted as an indicator of the most probable

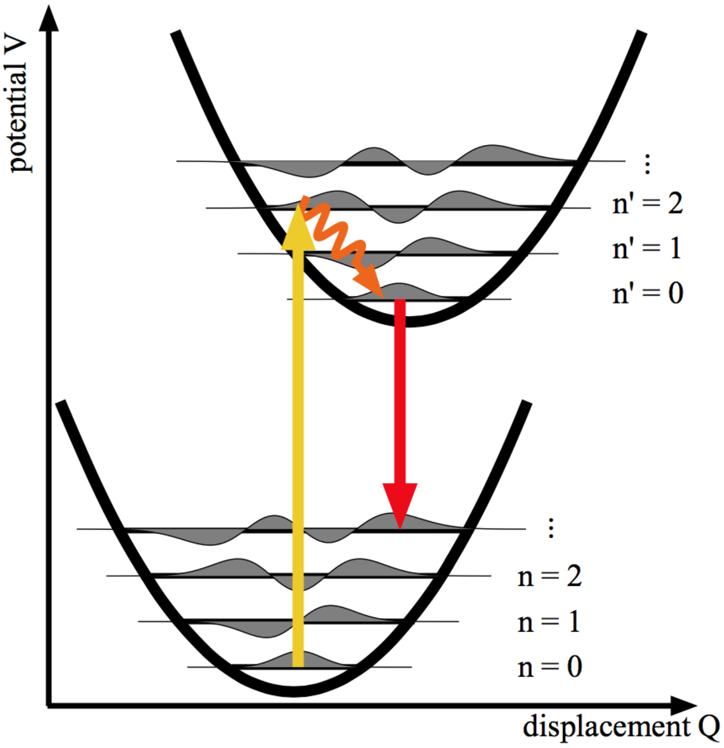

Figure 2.5: Electron phonon coupling approximated using harmonic oscillator potentials for the vibrational modes n in the ground and n' in the excited state. After an excitation to a higher vibrational state (yellow arrow), the color center quickly relaxes to the vibrational state $n' = 0$, from where it decays to the ground state via the emission of a photon (red arrow). The most probable transition is the one with the highest overlap between vibrational eigenfunctions ($n' = 0 \rightarrow n = 3$). Figure and caption reproduced from [51].

optical transition involving photons. A small value of S indicates a weak linear electron-phonon coupling resulting in negligible phonon side band emissions. If no phonons are involved, the entire emission is concentrated in the zero-phonon-line. Conversely, a large value of S indicates extensive electron-phonon interactions, leading to a pronounced phonon side band and a weaker zero-phonon-line.

For SiV centers hosted in polycrystalline diamonds the Huang-Rhys factors have been determined to be very small ranging from 0.08 to 0.24 [35, 102, 103]. As a result the zero-phonon-line as the most probable transition dominates the luminescence spectrum making SiV centers excellent narrow-band emitters. Figure 2.6 illustrates the stark difference between the zero-phonon-line and the phonon side band. In contrast, $S = 3.74$ has been established for nitrogen vacancy centers [95]. An electron-phonon coupling of this magnitude concentrates almost all emission into the phonon side band and leaves the zero-phonon-line strongly suppressed.

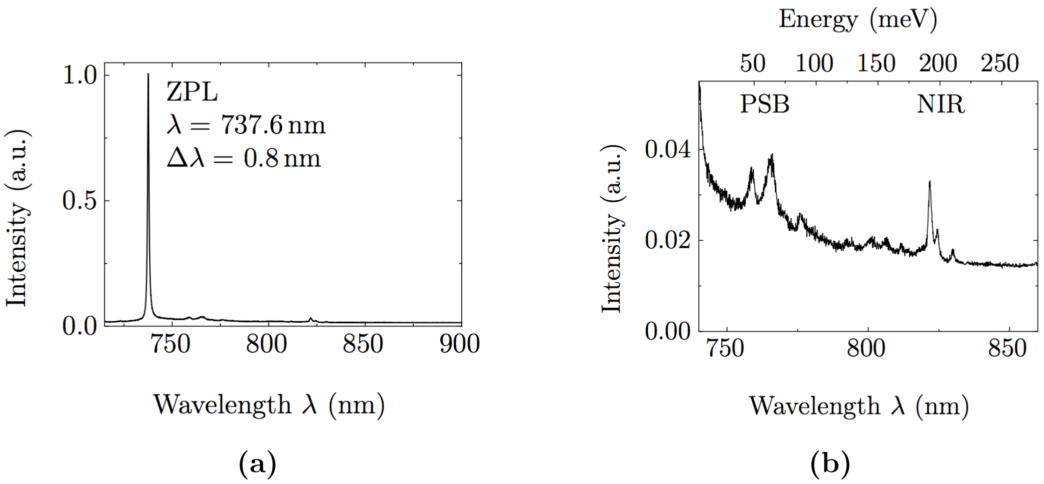

Figure 2.6: (a) The narrow zero-phonon-line dominates the luminescence spectrum. (b) Low intensity phonon side band shows distinct vibrational transitions. Figure reproduced from [47].

As an alternative measure for the electron-phonon coupling the Debye-Waller factor can be used. It is closely related to the Huang-Rhys factor S and defined as

$$D_w = e^{-S} = \frac{I_{ZPL}}{I_{ZPL} + I_{PSB}}, \tag{2.4}$$

which can be interpreted as the fraction of total photons that are emitted into the zero-phonon-line.

We close this chapter with a short discussion of the luminescence spectra of SiV centers at cryogenic temperatures. If ensembles of SiV centers are cooled below $\approx 10\,\mathrm{K}$ a fine structure is revealed [104]. It includes up to 12 different lines with intensities proportional to the natural abundance of the three stable isotopes of silicon $^{28}Si, ^{29}Si, ^{30}Si$ [105]. Each isotope is associated with 4 lines attributed to doublet levels of ground and excited states which are split by 0.2 meV and 1.07 meV respectively [84, 105, 106]. The splitting itself is believed to be a result of spin-orbit coupling with a weak contribution of the dynamic Jahn-Teller effect [84]. Initial results were based on ensembles of SiV centers, however, recently the splitting was detected for isolated SiV centers as well [107]. Figure 2.7 shows exemplary spectra representative for ensembles and single SiV center at cryogenic temperatures.

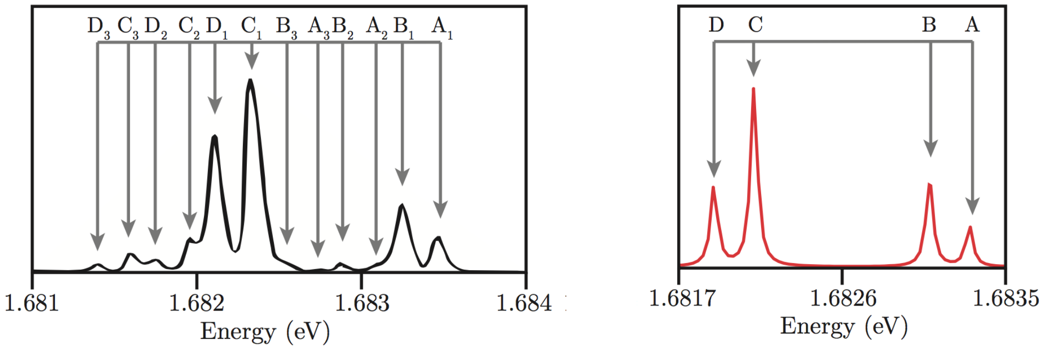

(a) **(b)**

Figure 2.7: (a) Fluorescence spectrum of an ensemble of SiV centers at 10 K. 12 peaks can be seen, 4 for each stable isotope of silicon [105]. (b) Fluorescence spectrum of an isolated SiV center at 15 K. 4 peaks can be seen, 2 for the ground state and 2 for the excited state. Figure reproduced from [47].

3 Photoluminescence Setup

The study and handling of SiV centers in nanodiamonds requires dedicated experimental methods and techniques. In the following we detail the experimental setup used to obtain the results presented in later chapters. The core of the setup consists of a confocal microscope connected to either a grating spectrometer or a Hanbury-Brown and Twiss interferometer. The former yields fluorescent spectra of SiV centers while the latter enables measurements of the intensity autocorrelation function of individual emitted fluorescent photons.

3.1 Confocal Setup

When studying SiV centers experimentally, two capabilities are key: Exciting SiV centers into emitting fluorescent light using a laser and the ability to register resulting SiV center fluorescence. A confocal setup elegantly supports both requirements. Confocal microscopy uses an objective to focus a laser onto a small volume of a sample which can be used to excite SiV centers in a controlled fashion. As the luminescence light returning from the emitter is in the same focus as the excitation laser light, it is effectively collected by the objective, thus the designation “confocal". For an overview of confocal microscopy we refer the reader to [108].

Figure 3.1 illustrates the confocal setup deployed in this work. With the exception of the laser and the sample stage, the whole setup is fixed to a vertical breadboard. The vertical design permits a horizontal sample stage, promoting quick scanning and exchanging of samples. The sample itself resides on top of a translation stage and is held in place sufficiently by surface friction. It is oriented by an aluminum angle adjustable via a manual rotation stage. The translation stage is moved by two stepper motors (Newport MVP25XL) enabling the sample to be translated horizontally, i.e. in the $x - y$ plane. Above the horizontal stage, the objective is fixed to another stage which in turn is mounted to a vertical breadboard. In this way, the vertical distance between the sample and the objective can be controlled. As a result the focus of the laser can be adjusted along the z-axis, i.e. the optical axis, allowing to implement a full three-axis scan of samples.

The bright red color in the sketch in Figure 3.1 represents the path of the excitation laser beam. The sample is excited with a continuous wave diode laser (Schäfter-Kirchhoff, 58FCM) emitting at a wavelength of 660 nm. The outlet of the laser

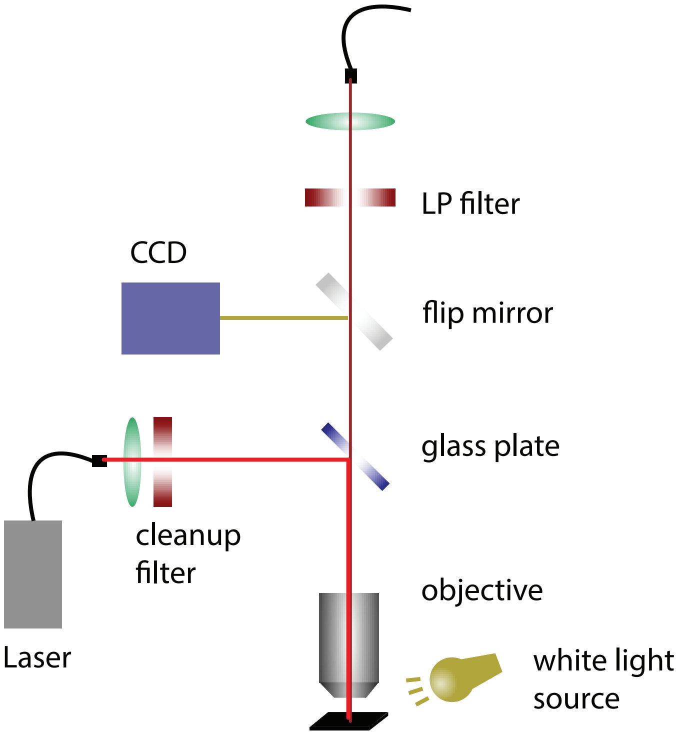

Figure 3.1: Confocal microscopy setup. An excitation laser beam (red) leaves an optical fiber and is directed towards a glass plate. The glass plate reflects ≈ 10 % of the incoming beam towards an objective after which is focused onto the sample. The same objective collects the resulting fluorescent light and redirects it towards the glass plate where ≈ 90 % of the light is allowed to pass. The passing fluorescence light light is fed into an optical fiber which connects to the detection part of the setup. A flip mirror can be engaged to bring a CCD camera into the setup in case a white light source is used to illuminate the sample.

is a pigtail fiber. The laser light is out-coupled and collimated by an aspheric lens. To suppress sideband emission from the laser, a 660 nm bandpass filter with a filter window of 10 nm is used. After this cleanup filter, the excitation beam hits a 2 mm glass plate (fabricator Bernhard Halle Nachfl. Germany) redirecting the beam. It is then focused onto the sample by a 100× microscope objective (Olympus, LMPlanFLN) with a numerical aperture of 0.8.

The collected light follows the detection beam path depicted in dark red in Figure 3.1. Both the excitation light reflected from the sample surface and the fluorescence light from the color centers pass through the glass plate. Removing the flip mirror behind the beamsplitter from the path directs light towards a single mode fiber (Thorlabs SM600) connecting the confocal setup with either the spectrometer or the HBT setup. Prior to focusing light into the single mode fiber using an aspheric lens, a long-pass filter is deployed to eliminate residual excitation light and ambient light. The filter is chosen with a cutoff wavelength of 710 nm or 720 nm.

Besides the obvious purpose of guiding the photoluminescence light to the spectrometer and the Hanbury-Brown and Twiss setup for spectroscopic investigations, it serves another crucial purpose. Namely, the core diameter of about 4.3 µm acts as a pinhole to reject photoluminescence light from depths outside of the focal plane [109]. For this axis parallel to the beampath the resolution amounts to about 2 µm, in the plane of the sample it is substantially higher with about 0.4 µm.

We remark that the glass plate in used Figure 3.1 has a high transmission of $\approx 90\,\%$. This leads to a high collection efficiency of fluorescence light light at the cost of excitation efficiency since most of the exciting light is not being redirected towards the sample. In contrast to that, certain use cases such as saturation measurements require high excitation intensities. To realize these the glass plate may be replaced by a dichroic mirror (692 Omega Optical DRLP). A dichroic mirror spectrally separates excitation light from photoluminescence light as it selectively transmits and reflects light as a function of its wavelength.

In general, if high excitation setting is required we opt for a dichroic mirror, otherwise working with the glass plate at lower excitation is the default. This is advised since high intensities carry the danger of damaging SiV centers to the point of bleaching and can also cause fluorescent intermittence of SiV centers, i.e. blinking, as an unwanted side-effect, see Chapter 2.

3.2 Optical Imaging of The Sample Surface

The setup introduced in the previous section can be modified to investigate the sample surface before starting fluorescence measurements. For this purpose, the sample is directly illuminated at a flat angle from outside the objective with white light from a halogen lamp, see the white light source in Figure 3.1. The flip mirror behind the glass plate is brought into the beam path to guide the light towards a CCD camera. The scattered light from the sample surface is collected by the objective and the surface is imaged on the CCD chip. Thus nanodiamonds and other features on the substrate are made visible. Factors limiting the quality of the image are not only the resolution of the confocal setup, but also shadows due to the incident angle of the white light source.

In Chapter 7 we introduce applications of SiV centers in nanodiamonds, for which knowing the precise positions of specific nanodiamonds is crucial. Therefore, cross markers are milled into the surface of the substrate on which the nanodiamonds are situated. These markers of a size of 10 µm can easily be recognized by optical imaging and can thus be used as landmarks for the purpose of indexing individual SiV centers. The starting point for a scan of an area of interest on the sample is determined by navigating with the optical image. After flipping the flip mirror out of the beam path, light is directed towards the detection part of the setup enabling systematic scans of the sample.

3.3 Spectrometer

Figure 3.2 displays the detection part of the setup. The fluorescence light arrives via a single-mode fiber connecting the confocal setup with the detection setup and is out-coupled with an aspheric lens. A flip mirror is employed to direct the light either to a grating spectrometer or the HBT setup. The optical spectrum of a light source gives insight to the optically active constituents and therefore bears information about the emitter.

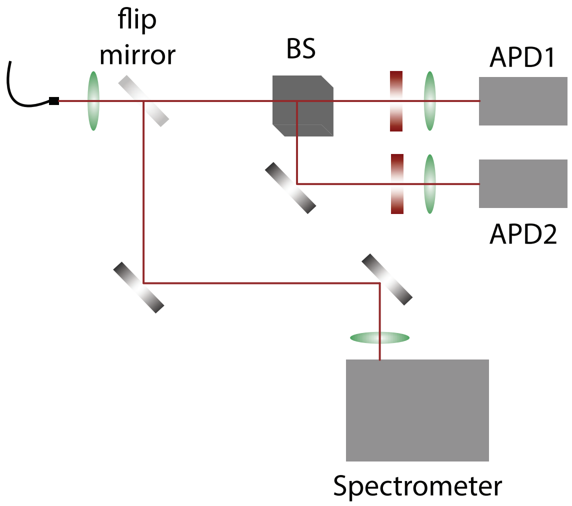

Figure 3.2: Spectrometer and HBT interferometer. Fluorescent light arrives via an optical fiber and is directed towards a flip mirror. The mirror directs the beam either towards a 50:50 beam splitter (BS) into the APDs of the HBT setup, or into a grating spectrometer.

As mentioned before, the fluorescence light from the SiV centers is investigated with the grating spectrometer (Princeton Instruments Acton2500i). The incident beam passes through an entrance slit, is then scattered on the grating where the light is spectrally divided and finally hits a detector, imaging the entrance slit on the detector surface. The employed detector is a CCD camera (Princeton Instruments, Spec-10) cooled with liquid nitrogen to a temperature of −120 °C. This limits background signals due to thermally generated free charge carriers. The spectrometer is optimized for detection of light up to a wavelength of 900 nm. and features three gratings: 600 grooves/mm, 1200 grooves/mm, and 1800 grooves/mm. These gratings are mounted on a turret, allowing easy swapping of gratings between measurements.

With the spectrometer's step-and-glue function which is implemented in the spectrometer software (WinSpec) it is possible to record several spectra over a wide wavelength range which are then stitched together. It is therefore the spectra are combine to a larger wavelength range with a higher resolution. For most measurements the grating with 600 grooves/mm was used. The resolution of the spectrometer using the 600 grooves mm^{-1} is 0.13 nm at 738 nm and the accuracy amounts to ± 0.4 nm as stated by the manufacturer.

3.4 Hanbury-Brown and Twiss Setup

A Hanbury-Brown and Twiss setup is used to establish the intensity autocorrelation function ($g^{(2)}$ function) of an emitter [110, 111]. In this work, the $g^{(2)}$ function is used to assert the non-classical behavior of a photoluminescence source, i.e. characterize its properties as a single photon emitter. In the photon number representation, it is defined as follows:

$$g^{(2)}(\tau) = \frac{\langle N(t)N(t+\tau)\rangle}{\langle N(t)\rangle^2}. \tag{3.1}$$

Here, $N(t)$ denotes the number of photons at a certain time t, $N(t+\tau)$ denotes the number of photon at a time interval τ later than t. The angular brackets $\langle\rangle$ denote temporal averaging. For a two-level system $g^{(2)}(\tau)$ can be interpreted as the probability of detecting two photons separated by a time interval τ. The physical intuition behind this definition is as follows: The detection of a fluorescent photon emitted from a quantum system is the result of an excited electron relaxing back to its ground state. To emit a consecutive single photon, an additional electron must first be promoted to an excited state, a process which takes a certain amount of time, see Chapter 2. If $g^{(2)}(\tau) > 1$ in the limit of $\tau \to 0$ a system is capable of emitting several photons simultaneously. This is known as photon bunching and is typical for classical light sources. In contrast, $g^{(2)}(\tau) < 0$ for $\tau \to 0$ is an indication that no two photons can be detected simultaneously. This property is termed photon anti-bunching and is a defining characteristic of non-classical light sources such as single photon source. The last important type are coherent (random) photons, as for instance produced via stimulated emission, for these $g^{(2)}(\tau) = 1$ for $\tau \to 0$ holds. Figure 3.3 shows how the $g^{(2)}$ function distinguishes these three types. For an in-depth review of the intensity auto-correlation function we refer the reader to [48, 112].

The aim of the HBT setup is to record the time delay between two consecutive photons as a prerequisite to compute $g^{(2)}(0)$. A sketch of the HBT setup is shown in Figure 3.2. Photons are detected using single photon avalanche photo diodes (APDs, PicoQuant τ-SPAD100). APDs are the semiconductor analog to photomultiplier tubes, i.e. an incoming photon creates secondary charge carriers through ionization. The secondary charge carrier is accelerated by a bias voltage to create

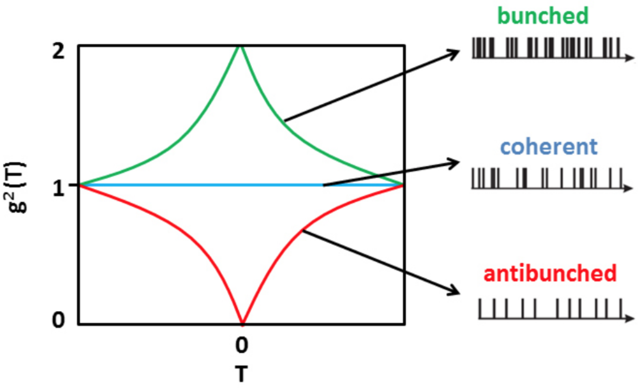

Figure 3.3: Intensity autocorrelation function for coherent, bunched, and antibunched light sources. Figure and caption reproduced from [113].

further secondary charge carriers, resulting in an avalanche effect. Therefore, the signal of a single photon is intensified and detected as an electrical current pulse. These avalanche photo diodes have a nominal detection efficiency of up to 70 % at an optimal wavelength of about 670 nm and a dark count rate of under 100 cps. If a charge carrier created by the avalanche is temporarily trapped and later liberated, it induces a so-called after-pulse. To avoid detecting these artifacts as real events, the APDs have a dead time of about 70 ns. In the ideal case, one APD would be enough to measure the time delay between two consecutive photons. However, the second of two consecutive photons could hit the detector during its dead time. To circumvent this problem, two APDs are employed and the detection beam is split with a non-polarizing 50:50 beamsplitter cube. Each beam then goes through a band-pass filter and is focused on the avalanche photo diode with an aspheric lens. As the beam path is slightly different for each APD, a small optical path difference is introduced, however, this difference only results in an offset of the $g^{(2)}$ function and does not alter the physical nature of the result. The bandpass filters serve two purposes: First, they limit optical crosstalk between the avalanche photo diodes. The detection process in an avalanche photo diode produces light due to recombination of charge carriers. Crosstalk between two avalanche photo diodes occurs, if one of the photons produced by recombination in one avalanche photo diode escapes and is detected in the other one [114]. Second, the band-pass filters serve to reduce background during the $g^{(2)}$ measurement process.

When the APD fires, it outputs a digital TTL (transistor-transistor logic compatible) signal. The arrival times of the signals, so-called time-tags, are recorded with a time-tag unit (produced by dotfast-consulting) with a temporal resolution of 78.125 ps. The timing uncertainty of the photon detection process introduces variations of the digital signal's time-tag from the actual detection time. This is called timing jitter and adversely affects the recorded time-tags and consequently the value of $g^{(2)}(0)$. In the past it has been shown to significantly obfuscate the detection of anti-bunching behavior in single photon source and thus relevant corrections need to be taken into account [47, 48].

As stated earlier, the time delay between two consecutive photons is necessary for the reconstruction of the $g^{(2)}$ function. The time delays are fed into a histogram which is then fitted to receive the continuous $g^{(2)}$ function. As a suitable fit function a numerical convolution between the $g^{(2)}(\tau)$ derived for a three-level system and detector timing jitter is used [43, 47, 48].

In the Hanbury-Brown and Twiss setup the arrival time of photons are recorded with two APDs, each of which keeps a list of arrival times as raw data. To get a single array of arrival times of the photons, the arrays of time-tags of the two APDs have to be correlated. Subsequently they are binned to obtain the $g^{(2)}$ function. For that, the time difference between each entry in one array and all consecutive time-tags in the other array are determined and binned according to the timing resolution of the time-tag unit. After normalizing and fitting these data, the $g^{(2)}$ function is obtained, determining whether an emitter qualifies as a single photon source.

4 Fabrication of Nanodiamonds

Due to its extraordinary properties, diamond has transcended its sole purpose as a rare gem and developed into an important tool enabling various applications in industry and research. This change has been driven largely by the development of methods allowing to cheaply produce synthetic diamond. While synthetic diamonds are typically small and without the splendor generally associated with diamond, they can be produced on-demand and are thus arguably more useful than rare gemstones. In this chapter we introduce the two most common methods for the fabrication of diamonds in a laboratory setting: The high-pressure, high-temperature (HPHT) and the chemical vapor deposition (CVD) method. The aptly named high-pressure, high-temperature process mimics the conditions under which diamond is formed in nature and is widely used to synthetically produce diamonds for industrial applications such as utilization of diamond as an abrasive. While HPHT diamonds are utilized in this work, most reported measurements are based on diamond produced with the CVD method in which diamonds are grown using a methane-hydrogen gas mixture. Both processes have in common that defects and impurities are a naturally occurring. For a more extensive list of diamond production processes refer to [115]. In the context of this thesis nano-sized diamonds are required. They can be obtained by milling larger sized HPHT or CVD diamonds down to the desired grain size in a vibrational mill. The obtained nanodiamonds are small enough that individual specimen have a chance of hosting a single SiV center. These can be identified and used for further exploration. Parts of the work presented in this chapter have been published in [46].

4.1 High-Pressure High-Temperature Diamond

The HPHT method was the first process to successfully synthesize diamond in 1879. Today, it is still widely used due to its relatively cheap production costs for small diamonds.

In the HPHT process, diamond is synthesized from graphite under temperatures of up to $1.5 \times 10^3\,^\circ\mathrm{C}$ and pressures between $5 \times 10^4\,\mathrm{bar}$ and $10^6\,\mathrm{bar}$ [115]. Under these extreme conditions, carbon transitions from its graphite to its diamond phase because the latter becomes energetically favorable [116–119]. The machine used for this kind of synthesis is a press. For some forms of this method, a metallic catalyst solvent is added lowering the required pressures and temperatures by causing graphite to dissolve earlier. At the same the catalyst promotes the crystallization process. Several press designs exist, all of which rely on creating and maintaining high pressures and high temperatures. While it is possible to grow big ($>$ 10 carat) high-quality diamonds with the HPHT process, its cost quickly increases and thus becomes unfavorable.

4.2 Chemical Vapor Deposition Diamond

In contrast to the HPHT method, in the CVD method diamond is crystallized from carbon available in the gas phase. The process still requires respectable temperatures in the range of 700 °C to 1300 °C but makes do with the low pressures of less than 1 bar available in a vacuum growth chamber [120].

The chamber contains a vapor consisting of a mixture of atomic hydrogen and methane. The gas is forced into the plasma phase using strong microwaves or hot filaments [121–123]. While the hot filament is easy to implement, it has the disadvantage that atoms which are etched from the filament during the growth process are likely to contaminate the diamond. To minimize the introduction of defects other than SiV centers in the diamond, growing diamonds in a microwave plasma is preferred. In it methane molecules dissociate and release carbon. In the presence of a substrate such as iridium coated with nucleation seeds, carbon can crystallize forming diamond. Figure 4.1 illustrates the setup. In a plasma containing atomic hydrogen, the formation of diamond is favored over the formation of graphite. This is due to the fact that the atomic hydrogen preferentially etches sp^2 bonded carbon, i.e. graphite.

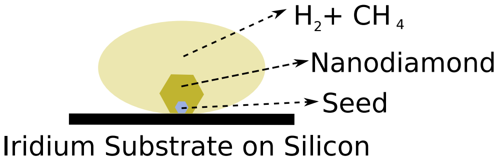

Figure 4.1: Sketch of the CVD method. A hydrogen-carbon plasma acts as a donor for carbon atoms which crystallize to form diamond on top of a suitable iridium substrate. A diamond seed initiates the process.

Typically, single crystal diamond substrates are required to grow single crystal diamond. HPHT substrates are suitable to start a crystallization process. This approach is referred to as homoepitaxial growth. An alternative approach is to utilize non-diamond substrates such as iridium or platinum to trigger heteroepitaxial growth [124, 125]. This method is utilized for all the CVD nanodiamonds grown and investigated in this thesis. It relies on small diamond crystals deposited on the substrate acting as seeds for the diamond crystallization process.[1] Seed dia-

---

[1] CVD nanodiamond growth performed by S. Gsell, group of M. Schreck, Augsburg University.

mond crystals are commercially available, and are usually particles produced by a so-called detonation process. In a detonation process, the high pressure produced by shock-waves of a detonation is used to create very small diamond particles of a size down to a few nanometers.

Growth on a substrate is favored, if the lattice constant of the substrate and the diamond to be grown are similar. The lattice constant of iridium is 0.384 nm [126, 127] and thus close to the lattice constant of diamond with 0.356 nm [115]. Therefore, the diamond was grown on a stratified substrate topped with an iridium layer of 60 nm to 150 nm thickness.[2] The iridium layers themselves were grown onto an yttria-stabilized zirconia (YSZ) buffer layer, which in turn was grown on a silicon wafer [128]. If the lattice constant of the substrate and the diamond are not matched, stress in the diamond lattice is induced. Therefore, the iridium substrate not only facilitates diamond growth, but also reduces unfavorable stress in the nanodiamonds. The detrimental effects of stress on the diamond lattice and its implications with respect to hosted SiV centers are discussed in Chapter 6.

To produce nanodiamonds of controlled size, the growth process is stopped when the diamonds grown onto the seed crystals are large enough. If the growth process is further continued, the individual crystals grow together to form diamond films. Such diamond films are used as starting material for the wet-milling process described in Section 4.3.

One of the advantages of the CVD process is that silicon is incorporated automatically into diamonds, SiV centers can thus be formed *in-situ* as the diamond is grown. The presence of silicon atoms required to be absorbed into the diamond lattice is explained by the plasma etching the edges of the silicon wafer underneath the growth substrate. To further increase the silicon content in the chamber, sacrificial silicon can be introduced.

In this thesis, two types of nanodiamonds samples were investigated. The first batch, henceforth referred to as CVD samples, was grown by the group of M. Schreck, Augsburg University using detonation diamond seeds of a size smaller than 3 nm (produced by the company Microdiamant, product Liquid Diamond monocrystalline, MSY 0-0.03 micron GAF). For the growth process, 1 % of methane was added to the hydrogen environment in the growth chamber. The growth process was performed with a pressure of 30 hPa for 30 min to 60 min, yielding nanodiamonds of a diameter of about 100 nm to 200 nm. An image of a sample of the produced diamonds is given in Figure 4.2.

The second type of samples consist of CVD nanodiamonds grown onto molecular analogs of diamond crystals. A subgroup of these molecular diamonds are called diamondoids and are carbon crystals based on the carbon cage molecule adamantane $C_{10}H_{16}$. The molecular diamonds used for this work are adamantane in cyclohex-

---

[2] Production of the stratified substrate performed by S. Gsell, group of M. Schreck, Augsburg University.

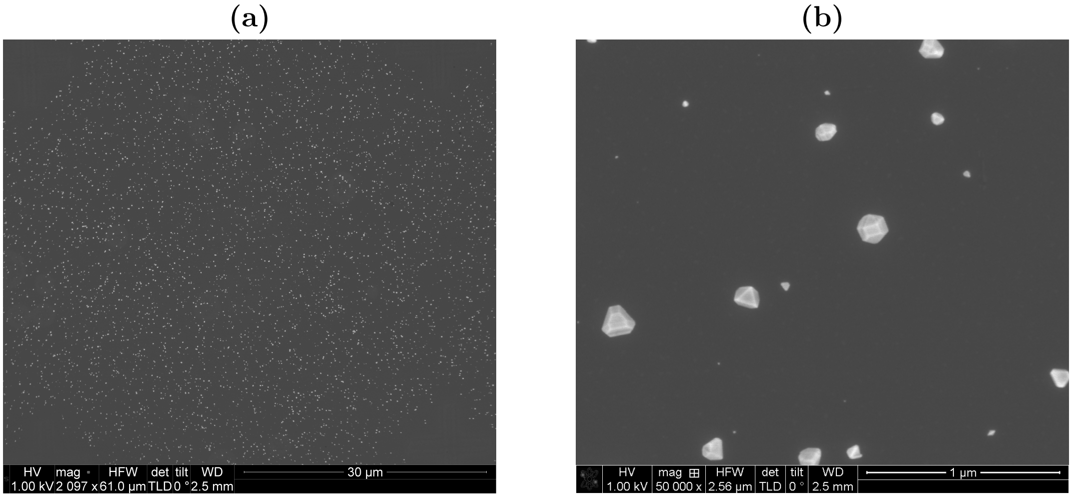

Figure 4.2: SEM images of CVD diamonds (sample insitucvd) produced by M. Schreck's group at Augsburg University. The average size of these nanodiamonds is 100 nm. (a) Overview image, white dots are nanodiamonds. (b) Detail image, it can be seen that nanodiamond shape and size is varied.

ane, mercapto adamantane in cyclohexane, and cyclohexane. Each of these seed crystals was used in different growth processes. During the growth process, either 1 % or 3 % methane was added to the hydrogen plasma and either silicon (Si) or silicon dioxide (SiO_2) was injected to promote the formation of *in-situ* incorporated SiV centers, see Table 4.1.

Unfortunately spectroscopic measurements revealed that the luminescence emission exhibits a strong background. Therefore diamondoids were not further investigated in this thesis.

Sample	Seed crystals	Methane conc.	silicon source
160211_E	Mercapto adamentane in cyclohexane	1 %	SiO_2
160211_F	Cyclohexane	1 %	SiO_2
160212_C	Cyclohexane	3 %	Si
160212_D	Adamentane in cyclohexane	3 %	SiO_2
160212_E	Mercapto adamentane in cyclohexane	3 %	SiOs
160212_F	Cyclohexane	3 %	SiO_2

Table 4.1: Summary of the samples grown on diamondoid seed crystals.

4.3 Wet-Milled Nanodiamonds

In addition to growing nanodiamonds of a specific size directly via a CVD process, macroscopic diamond starting material can be crushed to obtain small diamond particles. In contrast to nanodiamonds directly grown by a CVD process, the process is divided into two sub-processes: At first a macroscopic diamond is produced using one of the methods introduced in this chapter. Then macroscopic diamond is continuously milled into smaller diamond particles.

The wet-milled nanodiamonds investigated in this thesis were kindly provided by A. Muzha, group of A. Krueger, Julius-Maximilians Universität Würzburg. During the wet-milling process small metal beeds in an aqueous solution are driven by the vibrations of a vibrational mill. The moving beads continuously collide with the present diamonds and thus keep breaking them into smaller and smaller particles. A sketch of the process is shown in Figure 4.3. Steel contamination introduced by the beads are eliminated in a post-processing treatment with acid.

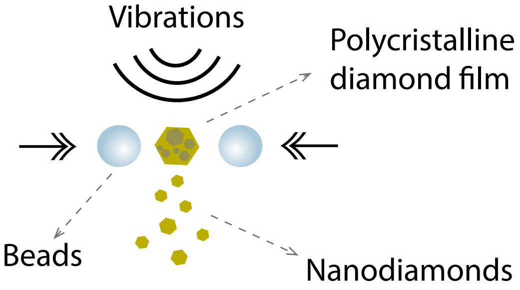

Figure 4.3: Sketch of a wet-milling process in a vibrational mill. A macroscopic polycrystalline diamond film is progressively broken down into smaller polycrystalline nanodiamonds by metal beads.

The big advantage of the milling process is that it enables the production of a large quantity of diamond nanoparticles. When producing nanodiamonds directly via a CVD process, the number of produced nanodiamonds in one process scales with the surface of the substrate on which the nanodiamonds are grown. In contrast, the quantity of milled nanodiamonds scales with the volume of the starting material. Another advantage of the wet-milling process is that the nanodiamonds are already in an aqueous solution after milling. Therefore, it can be used to spin-coat the nanodiamonds directly onto any substrate.

If the starting material for the wet-milling process is a polycrystalline diamond film, it is likely to break along crystal boundaries or other imperfections. However, the final nanodiamonds may still contain crystal boundaries resulting in reduced crystal quality. To improve diamond quality nanodiamonds are treated with post-processing steps including annealing in vacuum and oxidation in air. A detailed description of these processes and their effects is given in Chapter 5.

In general any diamond, independent of production method, can be used as starting material for the milling process. In the following sections, available samples are distinguished by the respective staring material and milling method.

4.3.1 Wet-Milled HPHT Nanodiamonds

We investigated nanodiamonds wet-milled from a HPHT starting material to median sizes of about 45 nm, 80 nm and 260 nm. They were then drop-cast onto an iridium substrate and implanted with $^{28}\mathrm{Si}^{1+}$ with a flux of $10^{11}\,\mathrm{cm}^{-1}$ at 900 keV. The implantation itself was performed by D. Rogalla, Ruhr-Universität Bochum (RUBION - Zentrale Einrichtung für Ionenstrahlen und Radionuklide). All HPHT nanodiamonds were oxidized in air at 450 °C for 3 h. Resulting samples available for explorations are designated hphtimp45, hphtimp80, hphtimp260 and listed in Table 4.2.

4.3.2 Wet-Milled CVD Nanodiamonds

In the following paragraphs, details of the production processes of nanodiamond produced by wet-milling a CVD diamond film in a vibrational mill are given [46]. For an overview of the samples refer to Table 4.2. The starting material for the wet-milled nanodiamonds was a nano-crystalline diamond film [129] directly grown on a silicon wafer by CVD. A microwave hydrogen plasma containing 1 % methane was used to grow on purified 5 nm nanodiamond seeds (produced by PlasmaChem). To induce *in-situ* SiV center creation, sacrificial silicon pieces were placed in the growth chamber. During diamond growth the silicon pieces are etched by the plasma leading to individual atoms being incorporated into the diamond lattice. The diamond film was then wet-milled in a vibrational mill with steel beads. The high amount of steel containment due to the steel beads is removed by extensive acid treatment. We also investigated nanodiamonds milled with silicon nitride beads, and found that the choice of material of the beads does not result in any noticeable difference in dependent measurements. The median diameters of the nanodiamonds are 50 nm, 70 nm and 100 nm as determined by laser diffraction spectroscopy. Figure 4.4c shows a photo of the obtained aqueous diamond solution, Figure 4.4a and Figure 4.4b show the milled nanodiamonds on top of an iridium substrate.

The aqueous solution containing the nanodiamonds is drop cast onto an iridium film on a silicon substrate. The iridium film of a thickness of 130 nm was grown onto a buffer layer of yttria-stabilized zirconia (YSZ) which in turn is grown onto a silicon wafer produced by O. Williams, School of Engineering, Cardiff University. The iridium surface has the advantage that it acts as an antenna and therefore enhances the collection efficiency of fluorescence light [42]. For a discussion on the

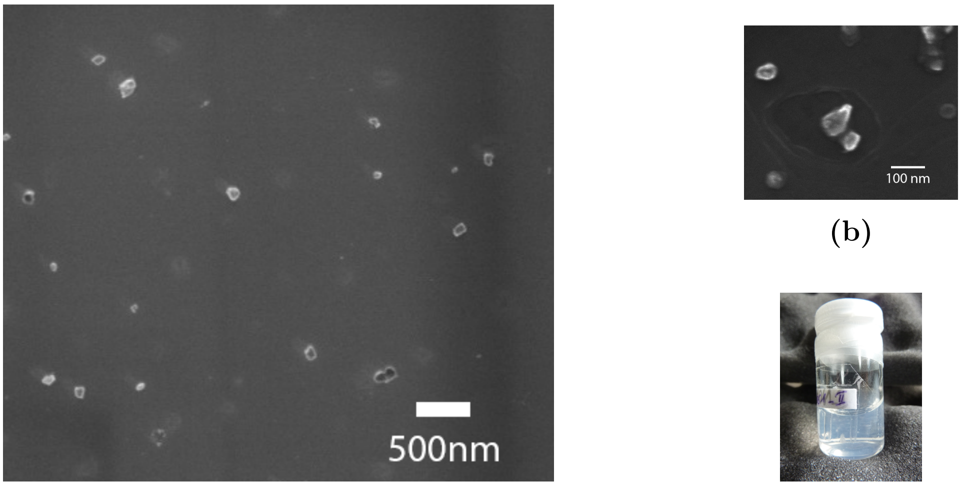

(a) (b) (c)

Figure 4.4: (a) SEM image of milled nanodiamonds (sample insitu100) showing the distribution of the nanodiamond crystals on the iridium substrate.(b) Close-up SEM image showing some individual diamond grains. (c) Picture of the diamond solution.

properties of the substrate see Section 4.4. Post-processing treatment consists of annealing in vacuum at 900 °C or oxidation in air at a temperature of 450 °C, or a combination of the two. The duration for either treatment method was 3 h to 6 h.

4.3.3 Doubly Wet-Milled Nanodiamonds Implanted With Silicon

In addition to SiV centers that were implanted during diamond growth, we investigated nanodiamonds with SiV centers implanted after diamond growth. We developed a procedure composed of consecutive milling steps to obtain nanodiamonds with an optimal concentration and homogeneous distribution of SiV centers in the host nanodiamonds. A suboptimal concentration of SiV centers in nanodiamonds arises from the fact, that silicon implantation causes the SiV centers to form in a specific depth dependent on the implantation energy. As a consequence, when implanting bulk material most of the diamond is left vacant of SiV centers. Hence, a big portion of nanodiamonds milled from such a bulk material would not host any SiV centers.

To obtain diamond particles with a homogeneous distribution of SiV centers, the process of fabricating implanted nanodiamonds is the following: First, a polycrystalline diamond film (produced by Element Six, electronic grade) is milled to diamond particles a few microns in size. Next, these microdiamonds are spin-coated onto iridium substrates and implanted with $^{28}\mathrm{Si}^{1+}$. To eliminate lattice damage and unnecessary vacancies resulting from the implantation process, diamonds were annealed in vacuum and subsequently oxidized. At last, the micrometer sized diamond particles are milled to the desired smaller sizes.

For the milling process in a vibrational mill, a minimum amount a few milligrams of diamond material is necessary. When starting with a diamond film, this threshold is easily reached, however, a big quantity of microdiamonds is needed to meet the requirements. To develop an optimal production procedure of implanted nanodiamonds, we first ran preliminary tests with a small amount of diamond material. After determination of the optimal specifications of the procedure, we began production on a larger scale.

For our first experiments, we coated a small amount of microdiamonds milled from the diamond film onto a silicon substrate without an iridium layer. The microdiamonds were then implanted with $^{28}\mathrm{Si}^{1+}$ at an implantation energy of 1.7 MeV, and fluences of $10^9\,\mathrm{cm}^{-}1$ to $10^{12}\,\mathrm{cm}^{-}1$.[3] After implantation, the microdiamonds on the silicon substrate were annealed for 2 h at 900 °C and subsequently oxidized in air for 2 h at 450 °C. For a detailed explanation of the effect of annealing and oxidation refer to Section 5.1.1. Using this procedure, we encountered the problem that the silicon from the substrate sublimated and re-nucleated during annealing. This process caused the diamonds to sink into the silicon surface, see Figure 4.5a.

Iridium is less prone to damage by high temperatures and withstands annealing procedures up to our standard annealing temperature of 900 °C without problems. Hence, we repeated the production process in the same manner as described above, but this time, we used an iridium coated silicon wafer as substrate. Thus we effectively circumvented the reported problems of microdiamonds sinking into the substrate surface.

Spectroscopic measurements revealed, that microdiamonds implanted with a fluence of $10^{11}\,\mathrm{cm}^{-2}$ were best suited to form a high concentration of SiV centers within the microdiamonds.

Following our results from the preliminary tests, we initiated mass production. A technical challenge was the limited space in the vacuum oven used for post-processing treatments of the microdiamonds. This circumstance capped the size of individual substrates for the microdiamonds to a side length of 2 cm. Hence, the microdiamonds were directly spin-coated onto 20 iridium substrates of a side length of 2 cm which yielded densely coated samples, see Figure 4.5b. After spin-coating the samples were implanted with $^{28}\mathrm{Si}^{1+}$ using an implantation energy of 900 keV with a fluence of $10^{11}\,\mathrm{cm}^{-2}$.[4] The microdiamonds were then annealed in vacuum for 3 h at 900 °C and oxidized in air for 3 h at 450 °C. As mentioned, a bottleneck

---

[3] Implantation performed by D. Rogalla, Ruhr-Universität Bochum (RUBION - Zentrale Einrichtung für Ionenstrahlen und Radionuklide).

[4] Implantation performed by J. Klug at rubitec - Gesellschaft für Innovation und Technologie der Ruhr-Universität Bochum mbH.

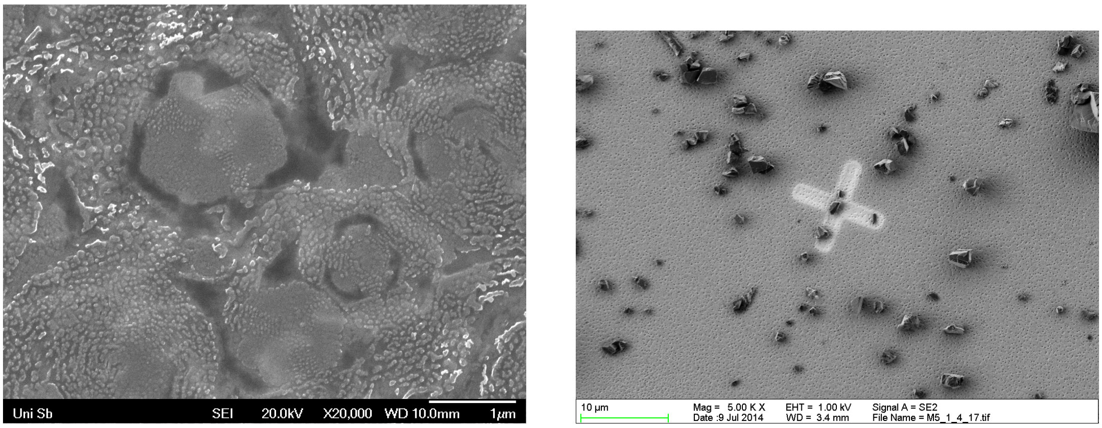

(a) **(b)**

Figure 4.5: (a) SEM picture of nanodiamonds sunken into a silicon substrate after annealing at 900 °C for 3 h. Magnification 20 000. (b) SEM image of the microdiamonds after milling, coated onto an iridium substrate, but before implantation. In the middle of the picture, there is a reference cross milled into the iridium substrate with a focused ion beam. Its size amounts to 10 µm. It can be seen, that the microdiamonds exhibit sizes of a few micrometer.

of the production was the limited space of the vacuum oven. Only 3 samples fit into it at once, hence it was necessary to recursively repeat the annealing process until all samples were annealed.

At last, the microdiamonds were milled again to sizes of about 40 nm, 45 nm, 240 nm and 260 nm. The diamonds of sizes 40 nm and 240 nm were directly annealed in vacuum at 1200 °C for 1 h and oxidized in acid [5] without prior spin-coating.

4.4 Iridium Substrate

As mentioned in Section 4.2, growth on a substrate is favored, if the lattice constants of substrate and diamond to be grown are similar. Therefore, for CVD nanodiamond growth a multi-layered substrate was prepared in a heteroepitaxial growth process. This substrate consists of a silicon wafer on the bottom, an yttria-stabilized zirconia buffer layer in the middle and an iridium layer on top. Initially, whole 4 in wafers were prepared with a multi-layered structure. After the heteroepitaxial growth processes, the wafer is cut to squares with a side length of 1 cm to fit into all machinery used during experiments, such as the spin-coater, the confocal setup, the focussed ion beam and the vacuum oven.

---

[5] Milling and post-processing performed by A. Muzha, group of A. Krueger, Julius-Maximilians Universität Würzburg.

Apart from the favorable lattice constant, iridium exhibits further advantages which lead us to coating the wet-milled diamonds onto these same multi-layered substrates:

- The high hydrophilicity of iridium enhances the homogeneity of the nanodiamonds on the substrate after spin-coating or drop-casting. Hydrophilicity is further improved by treating the substrate in a Piranha etch (50:50 mixture of sulfuric acid H_2So_4 and hydrogen peroxide H_2O_2) by removing oxide layers on the surface. The treatment with Piranha etch also has the advantage that all organic contamination is removed. Measurements after applying the Piranha cleaning yielded an estimation of the contact angle of slightly more than one degree. To determine the contact angle with water, the volume of a water drop is compared to the surface it covers after dropping it onto an iridium substrate, see Figure 4.6a. From that an estimation of the contact angle is deduced.
- During the post-processing steps, it is of major importance, that the substrate can withstand high temperatures. We remark that during the preliminary tests with implanted nanodiamonds on a silicon substrate we encountered difficulties with diamonds on a silicon substrate as they sunk into the surface after annealing. In contrast, iridium withstands the high temperatures required for annealing without damage.
- Iridium acts both as a mirror and as an antenna for the fluorescence light light emitted by the SiV center [42]. Therefore, the collection efficiency of the fluorescence light light is enhanced.

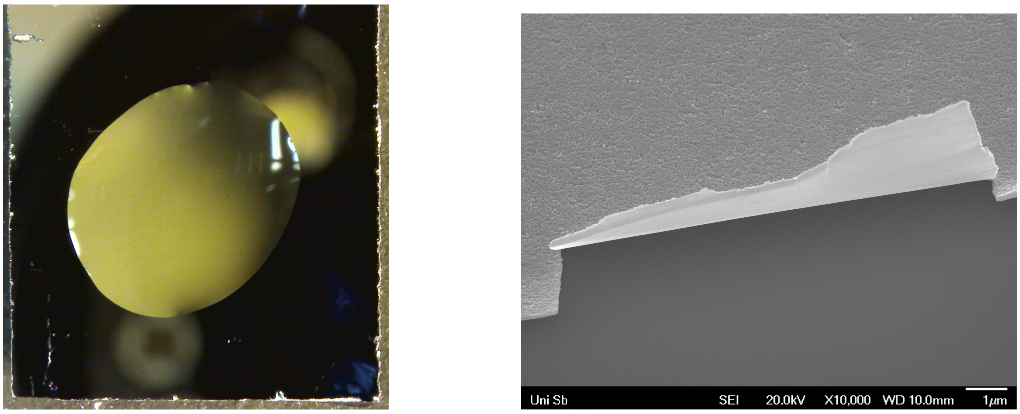

(a)

(b)

Figure 4.6: (a) Microscope image of a drop of water on an iridium substrate cleaned with Piranha etch. This picture was used to estimate the contact angle. (b) SEM picture of a 60 nm iridium layer that peeled off the substrate after cleaning in an ultrasonic bath.

At this point we comment upon a minor complication we experienced when using iridium surfaces. If the iridium layer is too thin, it tends to peel off the substrate, see Figure 4.6b. We encountered this problem during a cleaning procedure in the ultrasonic bath. However, this disadvantage is trivially circumvented by using a thicker iridium layer. For our measurements, we used an iridium layer of a thickness of about 130 nm, for which we did not encounter any adhesion problems.

4.4.1 Substrate Preparation

Prior to drop-casting or spin-coating a diamond solution onto the iridium substrate, the substrate is cleaned. The standard cleaning procedure is started with treating the substrate in diverse chemicals in an ultrasonic bath. Each step is carried out for a duration of 3 min to 7 min, approximately adjusted to the amount of contamination present:

- Distilled water with a drop of dishwasher detergent: Removes coarse contamination off the substrate.
- Isopropanol (purity 99.9 % p.a.): Dissolves oils without leaving oil traces as compared to ethanol.
- Acetone (purity 99.9 % p.a.): A heavy-duty degreasing agent, also dissolves many plastics.
- Distilled water: Acetone heavily reacts with the later applied Piranha solution, potentially causing explosions. Therefore, any acetone residue has to be removed. As acetone is water-soluble, distilled water is used to remove the residue.

Thereafter, the substrates are put into a Piranha solution (50 % sulfuric acid H_2So_4, 50 % hydrogen peroxide H_2O_2) to enhance the surface hydrophilicity and therefore obtain a homogeneous distribution of diamonds on the surface. They are then put again into distilled water and blow-dried with compressed air to avoid residue from the water.

The substrates were then either drop-casted or spin-coated with aqueous diamond solutions. For the former, the substrates are heated on a heating plate to a temperature of 60 °C. While the substrates are permanently heated by the heating plate, drops of a volume of about 5 µL are dropped onto the substrate surface. If substantially more than 5 µL is needed, then several drops of about 5 µL are dropped onto the substrate consecutively. A single large drop is ill-advised since the solution would flow off the substrate before drying.

For spin-coating, an on-site built spin coater was used. Before turning it on, the spin-coater is preset to a velocity of 2500 rpm. Then drops of 5 µL are dropped on the substrate and the spin-coater is immediately turned on. After about 3 min, the drop has dried. If more than 5 µL of diamond solution is wanted, the spin-coating is repeated until the desired amount is reached.

4.5 Listing of Investigated Samples

Sample name	Size	Si incorporation	Post-processing
hphtimp45	45 nm	*implanted*	oxidized in air at 450 °C
hphtimp80	80 nm	*in-situ*	annealed in vacuum for 1 h at 1000 °C and at 900 °C for 3 h
insitu50	50 nm	*in-situ*	series of individual samples with diverse post-processing steps
insitu70	70 nm	*in-situ*	series of individual samples with diverse post-processing steps
insitu70n	70 nm	*in-situ*	no post-processing, subset of insitu70
insitu70o	70 nm	*in-situ*	oxidized in air at 450 °C, subset of insitu70
insitu100	100 nm	*in-situ*	series of individual samples with diverse post-processing steps
insitu100ao	100 nm	*in-situ*	annealed in vacuum at 900 °C, consecutively oxidized in air at 450 °C, subset of insitu100
implanted250ao	250 nm	*implanted*	annealed in vacuum at 900 °C, consecutively oxidized in air at 450 °C
twomill40ao	40 nm	*implanted*	annealed in vacuum at 1200 °C, consecutively oxidized in air at 450 °C
twomill50o	50 nm	*implanted*	oxidized in air at 450 °C
twomill240ao	240 nm	*implanted*	annealed in vacuum at 1200 °C, consecutively oxidized in air at 450 °C
twomill260o	260 nm	*implanted*	oxidized in air at 450 °C

Table 4.2: Listing of investigated wet-milled samples. While this is a subset of all the samples investigated throughout the work of this thesis, these samples are the most thoroughly investigated ones. They are the basis for the results reported in Chapter 6. The first column indicates the names of the samples, the second the mean diameter of the nanodiamonds, and the third designates how the silicon was incorporated into the diamond.

5 Quality of Nanodiamonds

Carbon exists in a variety of crystalline and disordered structures, exhibiting three hybridizations, sp^3, sp^2, sp^1, see Figure 5.1. In its sp^3 configuration, characteristic of diamond, each of the four carbon valence electrons are assigned to a tetrahedrally directed sp^3 orbital resulting in strong σ bonds with adjacent atoms. In the threefold coordinated sp^2 configuration of graphite, σ bonds form a bonding plane as three of the four valence electrons participate in trigonally directed sp^2 orbitals. The remaining fourth electron of the sp^2 is found in a $p_z(p\pi)$ orbital normal to the boding plane. Here π orbital form weaker π bonds between one or more neighboring atoms. The final configuration is denoted sp^1 where two out of four valence electrons enter σ orbitals. Here σ bonds are formed directed along the x-axis. The remaining two electrons participate in $p\pi$ orbitals in the y and z directions. Strong directional σ bonds give rise to the extreme physical properties of carbon in its diamond form. Graphite is characterized by strong intra-layer σ bonding and weak van der Waals bonding across different layers [130].

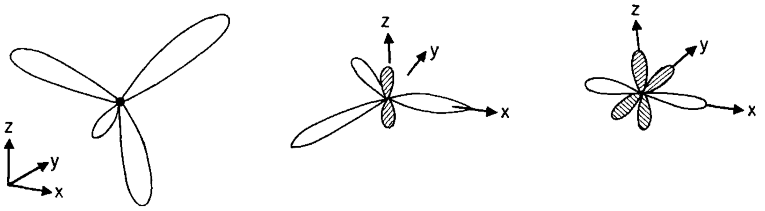

Figure 5.1: The sp^3, sp^2, sp^1 hybridized bonding of carbon [131].

In this thesis we perform measurements of SiV centers hosted in nanodiamonds produced by various means Chapter 4. In this context we use the term quality as a measure of how close diamond crystals are to their pristine form. The presence of lattice imperfections such as additional vacancies, lattice strain, impurities or the inclusion of graphite or amorphous carbon is known to adversely affect crystal quality [59, 132, 133].

If contaminations are present on the surface of nanodiamonds they can absorb a fraction of the fluorescence light emitted from within the diamond. Thus they reduce the quantum yield of SiV centers. Surface contamination like graphite and amorphous sp^2 hybridized carbon atoms manifest themselves as additional peaks in the Raman spectrum. Strain in the diamond lattice broadens the first order

Raman peak and causes it to shift to higher or smaller wavenumbers. Similarly, high concentrations of lattice defects cause additional peaks, a broadening of the first order Raman peak and a shift towards smaller wavenumbers.

To improve crystal quality and to reduce the mentioned distracting effects the following methods are deployed here: Annealing in a vacuum, oxidation in air as well as surface treatments involving plasmas.

To study the effectiveness of these treatments and to gauge the quality of our nanodiamond samples we rely on Raman spectroscopy and TEM imaging. The former is used to detect strain, quantify defect concentration and the presence of carbon in non-diamond phases, while the latter enables imaging of individual nanodiamonds revealing details in crystallinity such as crystal boundaries. Parts of the work presented in this chapter have been published in [46].

5.1 Quality-improving Post-Processing Treatments

5.1.1 Annealing and Oxidation

In this thesis we perform measurements with nanodiamonds produced both by direct CVD growth and by wet-milling a CVD diamond film. In a chemical vapor deposition reactor, either an amorphous carbon deposit, or a crystalline diamond film may be produced depending on the ratio of the fluxes of carbon and atomic hydrogen onto a substrate [134, 135]. Hence, both the milled and directly grown nanodiamonds may be contaminated with amorphous carbon. The degree of contamination can be kept to a minimum by tuning the parameters of the growth process.

SiV centers were formed both via *in-situ* implantation during CVD growth and via silicon implantation. *In-situ* implantation disrupts the integrity of the diamond lattice and potentially leads to lattice damage. During silicon implantation the diamond lattice gets damaged by the penetrating ions. sp^2 bonds, carbon interstitials and vacancies disrupt the metastable equilibrium of the diamond phase. Hence, there is a tendency for damaged diamond to “tip over" to the thermodynamically stable form of carbon, i.e. graphite.

At temperatures above about 500 °C, vacancies in the diamond lattice become mobile and diffuse towards the surface [136], disrupting the pristine diamond surface, causing surface contamination. Literature suggests, that annealing at 900 °C for 1 h is sufficient to remove most of the damage following implantations. To reduce the damage in the diamond lattice even further, we anneal the implanted diamonds at 900 °C to 1200 °C for 3 h to 6 h in vacuum (10^{-6} Pa).

The surface of the nanodiamonds is contaminated with graphite and amorphous sp^2 hybridized carbon. In particular, for milled diamonds contaminations are commonly introduced by the milling process due to mechanical abrasions. To remove these, we apply oxidation in an oven under ambient air at a temperature of 450 °C for 3 h to 6 h.

5.1.2 Surface Treatment With Gas And Plasma

We want to explore the possibility of reducing the detrimental effects of surface termination via various surface treatments with different gases. In particular, we treated our nanodiamonds with hydrogen (H_2), oxygen (O_2), ozone (O_3) both at room temperature and at 500 °C. Alternatively, we apply a H_2 plasma.[1]

Unfortunately, the only samples that yielded spectra with measurable ZPLs were the ones treated with H_2. However, we did not observe any luminescence enhancement. For all other treatments, we found that nanodiamonds either did not show any luminescence or immediately bleached upon excitation. Bleaching occurs even when using a continuous wave 660 nm laser at low excitation powers of 200 µW. While we cannot say for sure why this the case, we suspect that the treatments favor SiV center ionization. Since this approach did not seem fruitful, we did not pursue it further.

5.2 Raman Measurements

Raman spectroscopy of various samples gives insight into crystal quality and surface contamination of nanodiamonds. Raman scattering is the inelastic scattering of a photon $\hbar\omega_i$ on a molecule or crystal lattice in the initial state $|i\rangle$ with energy E_i. The molecule of crystal transitions into a higher energy state E_f and the scattered photon with frequency ω_s looses the energy $\Delta E = E_f - E_i = \hbar(\omega_i - \omega_s)$. Therefore, energy is exchanged between the photon and the excited matter, changing the rotational or oscillation energy of the involved molecule or the oscillation energy, i.e. phonons of the crystal lattice. The Raman shift is typically referenced in wavenumbers and given by

$$\Delta\omega = \left(\frac{1}{\lambda_{ex}} - \frac{1}{\lambda_R}\right), \tag{5.1}$$

where λ_{ex} denotes the excitation wavelength and λ_R the center wavelength of the Raman peak. As every solid exhibits characteristic phonon modes tied to the properties of its lattice structure, Raman spectroscopy can be used to characterize

---

[1] Performed by O. Williams, School of Engineering, Cardiff University.

diamond. Raman measurements of nanodiamonds give insight into the issues of surface contamination, lattice strain and defect concentration: Surface contamination like graphite and amorphous sp^2 hybridized carbon atoms cause additional peaks in the Raman spectrum. A high defect concentration may lead to additional peaks, a broadening of the first order Raman peak and a shift to smaller wavenumbers. Strain in the diamond broadens the first order Raman peak and causes a shift to higher wavenumbers [59, 132, 133].

For Raman measurements the setup described in Section 3.1 is used. As excitation light source, a 532 nm continuous wave diode laser operating in single mode is used (Integrated Optics®Matchbox Laser 0532L-41B) [46]. It provides single frequency mode laser light, a prerequisite for Raman investigations. The beamsplitter is a dichroic mirror (Omega Optical 645DRLP), the laser light is additionally blocked out with a 532 nm notch filter in the detection path in front of the single mode fiber replacing the usual long pass filter. With these adaptations, the combination of the confocal unit and the spectrometer serves as a Raman spectrometer. As the diamond Raman line is very narrow, the 600 grooves/mm grating does not offer sufficient resolution and is only used for a coarse approach. Detailed measurements are realized using 1200 grooves/mm and 1800 grooves/mm gratings.

Since the size of single nanodiamonds is on the order of tens of nanometers, low signal intensities can become an issue when taking Raman measurements. To overcome this problem we pursue two different approaches:

a) Nanodiamond Clusters: Collective measurements are carried out at several areas on the sample insitu70. Since this sample is densely covered with nanodiamonds, collective measurements of clusters of nanodiamonds achieve higher signal intensities, see Figure 5.2a.

b) Large Nanodiamonds: Raman measurements are carried out on the implanted sample implanted250ao. For this sample, diamond particles are large enough to yield sufficient intensities on single nanodiamonds.

5.2.1 Surface Contamination

We test the impact of oxidation treatment as described in Section 5.1.1 on surface contamination. Figure 5.2a shows a measured Raman spectrum of a sample without oxidation treatment (insitu70n). To verify reproducibility, the measurement is performed on three different spots of the sample. The narrow peak in Figure 5.2a corresponds to the first order diamond Raman peak and will be further analyzed in Section 5.2.3. The spectrum also shows a broad peak with a Raman shift of about $(1582 \pm 5)\,\mathrm{cm}^{-1}$. This shift corresponds to the G-band due to amorphous sp^2 hybridized carbon atoms and graphite. The exact G-band position and linewidth is sensitive to parameters such as the clustering of the sp^2 phase, bond-length and bond-angle disorder, presence of sp^2 rings or chains, and the sp^2/sp^3 ratio [137].

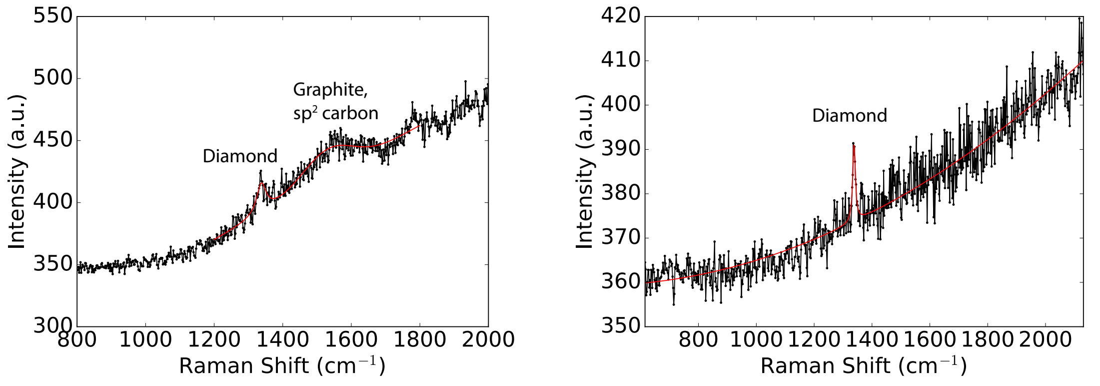

(a) (b)

Figure 5.2: Raman measurements, black: data, red: fit. (a) Raman measurement before oxidation, sample insitu70. The diamond Raman peak is situated at 1338 cm^{-1}. The broad feature around 1580 cm^{-1} corresponds to the graphite G-band. (b) Raman measurement after oxidation, sample insitu70o. The G-band has vanished, indicating removal of graphite and amorphous sp^2 hybridized carbon.

The nanodiamond Raman spectra are considerably modified after oxidation in air at 450 °C. To verify this, we perform Raman measurements on three different spots of a sample produced in the same process as the above mentioned, which is additionally oxidized (insitu70o). While the G-band peak is present in every measurement performed on a non-oxidized sample, it is not present in any of the oxidized samples (Figure 5.2b), indicating successful removal of sp^2 hybridized carbon and surface graphite.

5.2.2 Defect Concentration

Several effects impact the first order diamond Raman line: 1. defects in the diamond lattice, 2. hydrostatic pressure, 3. uniaxial or more complicated stress configurations. In the measurement on nanodiamond clusters the width of the diamond Raman peak of sample insitu70 varies between 15 cm^{-1} and 30 cm^{-1} without oxidation treatment, but is only 9 cm^{-1} to 11 cm^{-1} after the oxidation process. A possible reason for this change of the width is improved crystal quality [132]. In the measurement on large nanodiamonds we measured a Raman line at (1308 ± 5) cm^{-1} (denoted line R1) which exhibits a broad linewidth of (25 ± 5) cm^{-1}. One plausible explanation for both the position and the linewidth of the Raman line are defects in the diamond lattice [132].

5.2.3 Lattice Strain

We investigated how strain in the diamond lattice manifests itself in both measurements on nanodiamond clusters and on large nanodiamonds. In the Raman measurement on nanodiamond clusters, the position of the diamond Raman peak is the same for oxidized (insitu70o) and non-oxidized (insitu70n) samples, indicating that oxidation does not affect strain in the diamond. However, the Raman shift of both non-oxidized and oxidized samples amounts to $(1338 \pm 5)\,\mathrm{cm}^{-1}$, as compared to the literature value of $1332.5\,\mathrm{cm}^{-1}$ of pristine diamond [59] (given uncertainties are governed by spectrometer resolution). This shift indicates the presence of strain in the diamond particles.

Performing several Raman measurements on large nanodiamonds we find diamond Raman lines at $(1308 \pm 5)\,\mathrm{cm}^{-1}$ (line R1), at $(1345 \pm 5)\,\mathrm{cm}^{-1}$ (line R2) and at $(1348 \pm 5)\,\mathrm{cm}^{-1}$ (line R3), indicating a broad distribution of strain among the individual diamond particles (uncertainties governed by spectrometer resolution). Only line R1 can be explained with a high defect concentration in the diamond lattice due to its shift to smaller wavelength.

However, a more consistent model which explains all occurring shifts is the presence of strain/stress in the diamond nanoparticles. The Raman shift $\Delta\nu$ in the presence of compressive and tensile stress is given by [138, 139]:

$$\Delta\nu = \frac{p}{0.34}, \tag{5.2}$$

where the Raman shift $\Delta\nu$ is given in cm^{-1} and the stress p in GPa.

The calculation yields a pressure range from (-8.33 ± 1.70) GPa tensile stress to (5.27 ± 1.70) GPa compressive stress. Whereas under hydrostatic pressure the triply degenerate first order Raman peak remains degenerate, under uniaxial and more complex stress configurations (biaxial stress, shear stress etc.) mode splitting occurs [132]. As mentioned above, we observe broad linewidths up to $(25 \pm 5)\,\mathrm{cm}^{-1}$. The broad linewidths of the Raman lines may be attributed to uniaxial strain, as mode splitting manifests itself in a broadening of the peak due to limited spectrometer resolution.

5.3 Transmission Electron Microscopy

Transmission electron microscopy (TEM, also sometimes conventional transmission electron microscopy or CTEM) is a microscopy technique in which a beam of electrons is transmitted through a sample to form an image. The sample is most often an ultra-thin section less than 100 nm thick or a suspension on a grid [46]. An image is formed through the interaction of the electrons with the sample as the beam is transmitted through the sample. Since electrons have higher de Broglie wavelengths than photons, a high resolution is obtainable, allowing the surface of nanodiamonds to be resolved. Thus, the crystallinity of single nanodiamonds can be studied directly.

5.3.1 Crystallinity and Grain Boundaries

For TEM investigations nanodiamond samples must obey certain size requirements. In particular, they must be large enough for the carbon grid inside the microscope acting as a stage for specimen to hold them. Furthermore, their diameter must not exceed a certain value, since the TEM electron beam must be able to permeate the material for imaging. Samples of type insitu100 mostly comprised of nanodiamonds fulfilling these requirements, was investigated by J. Schmauch, group of R. Birringer, Saarland University.

In Figure 5.3a a TEM image of a single nanodiamond is shown. A complex crystal formation deviating from single crystal diamond structure is visible. A higher resolution detail is given in Figure 5.3b. The image clearly shows different crystal orientations, asserting that the nanodiamond particle is not a single crystal diamond. Within the nanodiamond, several sharp lines are visible. These lines are edges of crystal boundaries and grain boundaries, introducing strain in the diamond lattice. We remark at this point that some studies suggest the possibility that SiV centers are created with a higher probability at grain boundaries and morphological defects of the crystal [140, 141].

We repeated this visual assessment of crystal quality for a range of different nanodiamonds with identical results. This supports the conclusion that our nanodiamonds are polycrystalline.

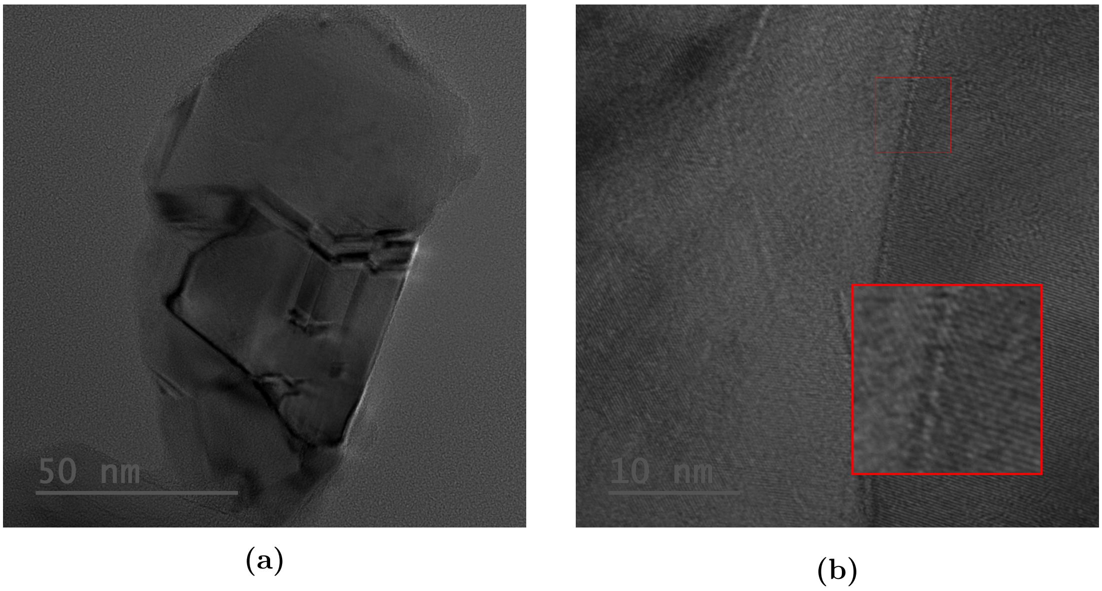

(a)

(b)

Figure 5.3: Transmission electron microscopy (TEM) pictures of sample insitu100. (a) Image of a single nanodiamond particle revealing a complex crystal structure. (b) Close-up image of a diamond particle. The vertical line is a crystal boundary, to the left and right the parallel layers of one crystalline region can be seen. For better visibility, the inset shows a magnification of the area indicated by a red box. The different orientations of the crystal lattice layers are visible.

6 Spectral Distribution of SiV centers in Nanodiamonds

In this chapter we report our results regarding luminescence properties of SiV centers. Parts of the work presented in this chapter have been published in [46]. The samples used in our investigation consists of a large set of wet-milled CVD nanodiamonds containing *in-situ* SiV centers of a size in the range of 70 nm to 100 nm. Throughout the chapter we refer to samples using their distinct sample-id as listed in Table 4.2.

The obtained fluorescence spectra of SiV centers show that both the center wavelength of the ZPL as well as the linewidth of the zero-phonon-line vary significantly among individual nanodiamonds. Our measurements over a large set of SiV centers indicate a strong correlation between the center wavelength of the zero-phonon-line and the corresponding linewidths, resulting in a previously unreported bimodal distribution. We assert single photon emission from these SiV centers across the whole range of zero-phonon-line positions and linewidths. Furthermore, we detect fluorescence intermittency, i.e. blinking. The obtained data for the bright and dark times indicate an exponential decay of the dark state and a log-normal decay of the bright state, the latter of which has to our knowledge not been reported as of yet.

6.1 Photoluminescence Spectra

To identify nanodiamonds containing SiV centers, we performed confocal scans of the samples, see Figure 6.1. To reduce bias in the measurements, not only the brightest spots of the confocal scans are investigated, but also those which barely exceed background fluorescence. SiV centers are further investigated by measuring photoluminescence (PL) spectra, single photon statistics and photostability. As discussed in Chapter 2, the typical luminescence spectrum of an SiV center is composed of a prominent zero-phonon-line peak and weak sidebands. Investigations of both are reported independently in the following paragraphs.

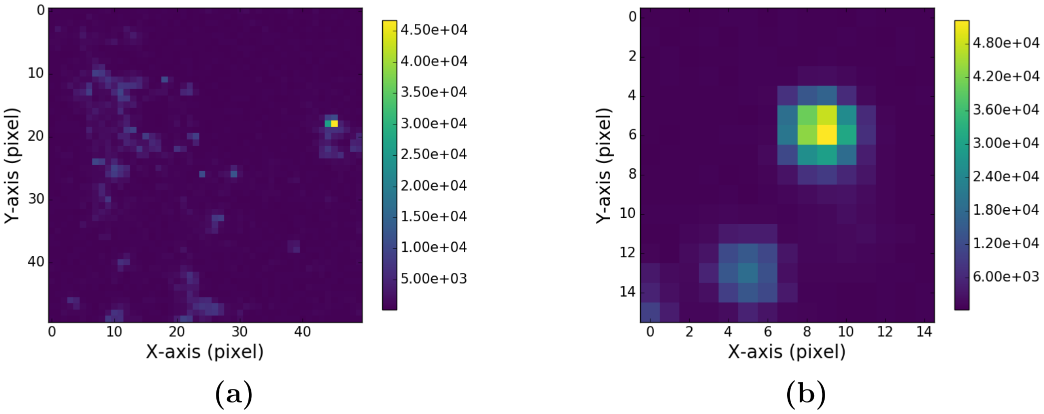

(a) (b)

Figure 6.1: Photoluminescence scans measured in the confocal setup. (a) depicts an overview of a size of 50 µm × 50 µm. The bright yellow dot is emitter V1 introduced in this chapter. Also several of the not so intense emitter visible as light blue spots were investigated. (b) Shows a detail scan of a size of 8 µm × 7.5 µm of emitter V1.

6.1.1 Zero-Phonon-Line

The center wavelength and the linewidth of the zero-phonon-line (ZPL) of SiV center luminescence spectra for samples insitu50, insitu70, and insitu100 are determined by fitting a Lorentzian fit to the ZPL. Both spectra from nanodiamonds containing single and multiple SiV centers are taken into account. Figure 6.2 depicts a few examples of the measured spectra in order show how diverse they are.

In Figure 6.3 the linewidth for each measured ZPL is plotted against its center wavelength. What immediately strikes the eye is a pattern that to our knowledge has not been reported to date: The observed ZPLs partition into two groups, a horizontal cluster (group H) and a vertical cluster (group V). The two clusters are separated by a gap, i.e. a region with a pronounced lack of data points. Single emitters are identified both in group H and group V, marked as red triangles in Figure 6.3. Further details on single emitters are given in section Section 6.2. The two groups are defined by their characteristic center wavelengths and linewidths: In group H very prominent ZPL peaks are found showing linewidths in the range of 1 nm to 5 nm and center wavelengths in the range of 715 nm to 835 nm.

Figure 6.4a shows a representative spectrum of a single emitter in group H (denoted emitter H1), exhibiting a ZPL linewidth of 1.4 nm and a center wavelength of 726.5 nm. In contrast, in group V, the spectra exhibit broader ZPL linewidths of approximately 5 nm up to 18 nm. Their ZPL center wavelengths, however, are distributed within the very narrow range of 738 nm to 741 nm. Figure 6.4b shows a spectrum of a single emitter of group V (denoted emitter V1) with a ZPL linewidth of 6.4 nm and a center wavelength of 740.8 nm. For comparison, the room tempera-

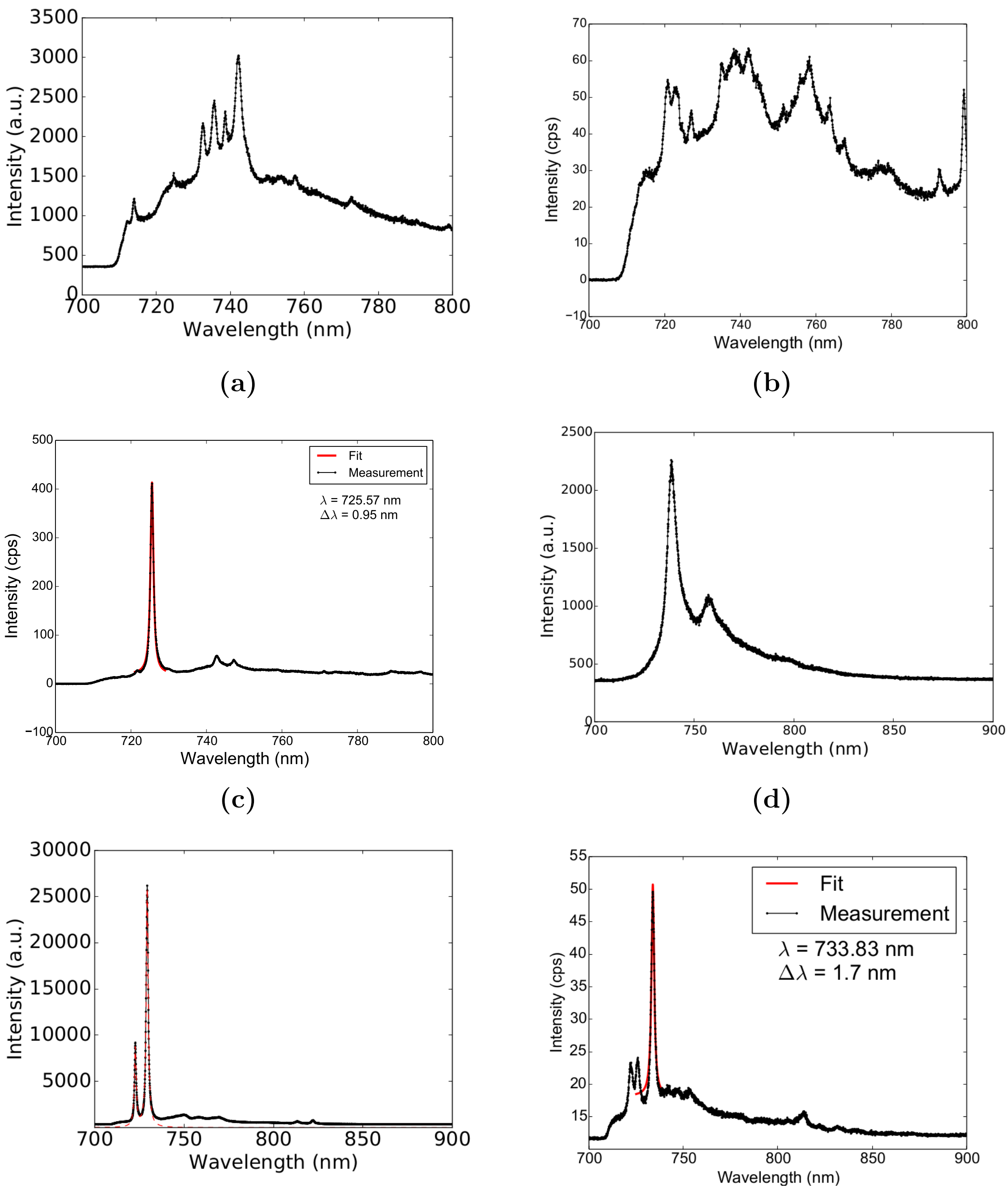

(a) **(b)** **(c)** **(d)** **(e)** **(f)**

Figure 6.2: Various spectra of samples consisting of wet-milled nanodiamonds with *in-situ* incorporated SiV centers. The nanodiamonds yielding spectra (a) and (b) host many SiV centers with ZPL at different center wavelengths. (c) and (d) exhibit one dominant ZPL and recognizeable sideband features. In (e) two ZPLs of different intensity are visible, in (f) one ZPL donminates the spectrum while some ZPLs of lower intensity are present.

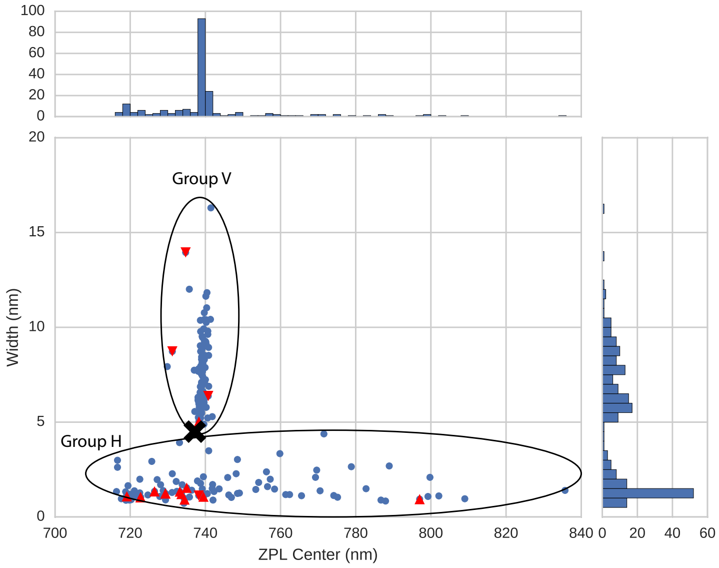

Figure 6.3: Distribution of the ZPL center wavelength versus the linewidth of the ZPL of the investigated SiV centers in milled nanodiamonds containing *in-situ* incorporated SiV centers for samples insitu50, insitu70, insitu100. The data separates into a horizontal (group H) and a vertical (group V) cluster. The bold black cross marks the position of an ideal SiV center in unstrained bulk diamond [142]. The red triangles indicate emitters with an anti-bunching dip in the $g^{(2)}(0)$ measurement. Upwards pointing triangles represent blinking emitters (fluorescence intermittency), while triangles pointing down represent non-blinking emitters (see Section 6.3).

ture ZPL of SiV centers in unstrained bulk diamond exhibits a linewidth of 4 nm to 5 nm and a center wavelength of 737.2 nm marked with a black cross in Figure 6.3 [107, 142].

To determine how much the ZPLs contribute to the total observed emission of emitter H1 and emitter V1, we determine the Debye-Waller factors for both. The Debye-Waller factor is defined by $DW = I_{ZPL}/I_{TOT}$ and is therefore suited as a measure for sideband intensity. The Debye-Waller factor for emitter H1 amounts to 0.81 ± 0.01. This Debye-Waller factor corresponds to a Huang-Rhys factor $S = -\ln(DW)$ [63] of 0.21 ± 0.01, which is in good agreement with the values reported in [85]. The error is mainly due to background corrections. When zooming in onto the spectrum of emitter V1 we do not find distinct sidebands peaks, i.e. almost all emission for this emitter is focused into the ZPL. Considering resolution limits of the spectrometer, dark-counts and fluorescence background, we evaluate the Debye-Waller factor to be larger than 0.97. It is the largest Debye-Waller factor amongst all our milled SiV centers. The two mentioned Debye-Waller factors should not be interpreted as single representative emitters for the respective groups, they rather

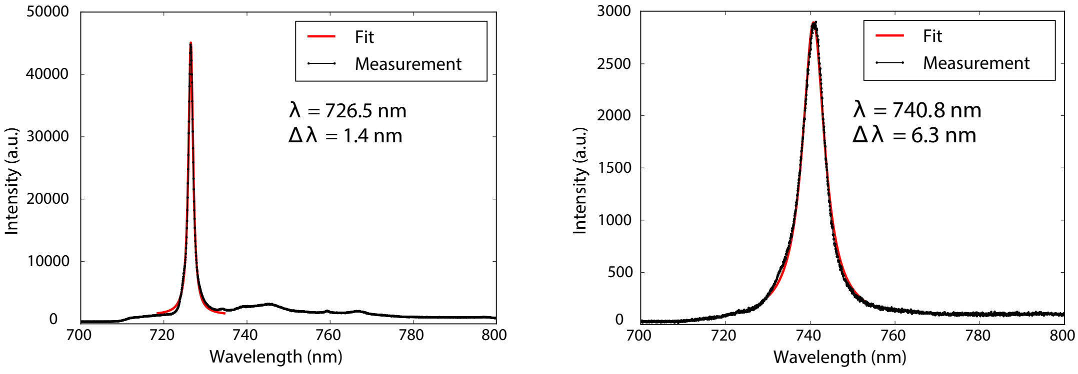

(a) (b)

Figure 6.4: Representative photoluminescence spectra of sample insitu100ao measured at room temperature. (a) Spectrum of group H of Figure 6.3, denoted emitter H1. (b) Spectrum of group V of Figure 6.3, denoted emitter V1. The red lines are Lorentzian fits to the peaks.

serve as an orientation of the spread of the Debye-Waller factors of both groups. It has to be pointed out, that we did not find any systematic difference of the Debye-Waller factor between group H and group V.

To provide context for the novel findings presented in Figure 6.3, we compare our results to various earlier findings. Furthermore, we discuss an additional comparison to an investigated control sample fabricated using silicon implantation. The results are presented in Figure 6.5.

Samples for which previous data has been taken are:

1. nanodiamonds produced by bead-assisted sonic disintegration (BASD) of polycrystalline CVD diamond films (blue rings in Figure 6.5 [144]; data taken from [143]).
2. nanodiamonds produced by heteroepitaxial CVD growth on iridium substrates with *in-situ* incorporated SiV centers; measured in a spectral filter window of 730 nm to 750 nm (blue squares in Figure 6.5; data reused from [48] with permission).
3. nanodiamonds produced in the same manner as in 2 (blue downwards pointing triangles in Figure 6.5; produced by M. Schreck [85]; spectroscopic measurement performed with setup described in Section 3.1).

All previous data from different nanodiamond material fit nicely with the ZPL distribution presented in Figure 6.5, confirming the findings of Figure 6.3.

We verify that the observed luminescent defects are indeed silicon related by performing control experiments with silicon implanted samples (implanted250ao). By

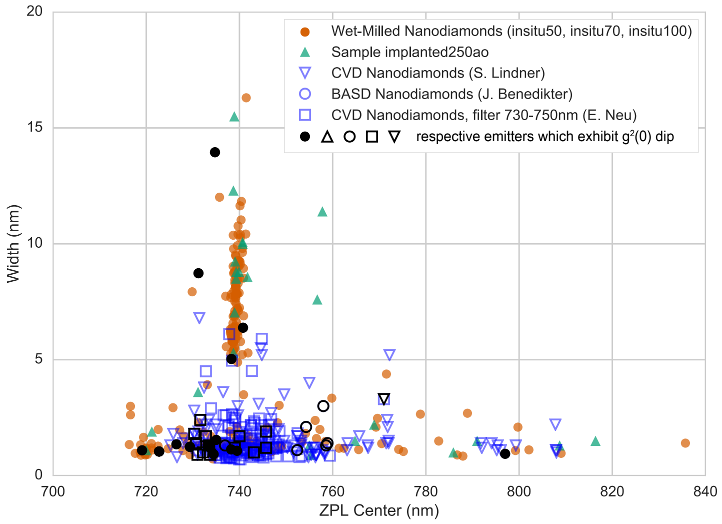

Figure 6.5: Comparison of the distribution of the linewidth vs. the center wavelength of the ZPL of the investigated SiV centers in milled nanodiamonds (samples insitu50, insitu70, insitu100) with data measured on sample implanted250ao (implanted with Silicon); with data measured in our group on CVD nanodiamonds produced by M. Schreck [85]; with data measured on nanodiamonds reported by J. Benedikter in [143]; and with data measured in CVD diamonds by E. Neu in a filter window between 730 nm and 750 nm [48]. Black symbols represent emitters exhibiting a dip in the $g^{(2)}(0)$ function, indicating a single or very few SiV centers

doing so we rule out the possibility that the two clusters in the distribution are a result of artifacts. Such artifacts include other elements incorporated into the nanodiamonds during the growth process: Residue from previous processes performed in the diamond growth chamber or material from chamber parts may be incorporated during nanodiamond growth. Figure 6.5 shows that the implanted SiV centers cover roughly the same spectral range as the *in-situ* incorporated centers from around 720 nm to 820 nm as the *in-situ* incorporated centers. This correlation provides strong evidence for the silicon related origin of the defects.

To provide a theoretical interpretation, the ZPL center wavelength shift is investigated in further detail and compared to results from density functional calculations. Zooming in to group V (Figure 6.6a) it becomes clear that only six of the measured data points in group V are situated at a shorter center wavelength than the point attributed to an ideal SiV center in unstrained bulk material. The the shortest wavelength shift is at 729.9 nm. At the same time, much more data exhibit a center wavelength larger than the ideal SiV center. This asymmetry suggests that a red-shift of the ZPL of an SiV center is significantly more likely than a blue-shift.

Several mechanisms contribute to the center wavelength shift, predominantly hydro-

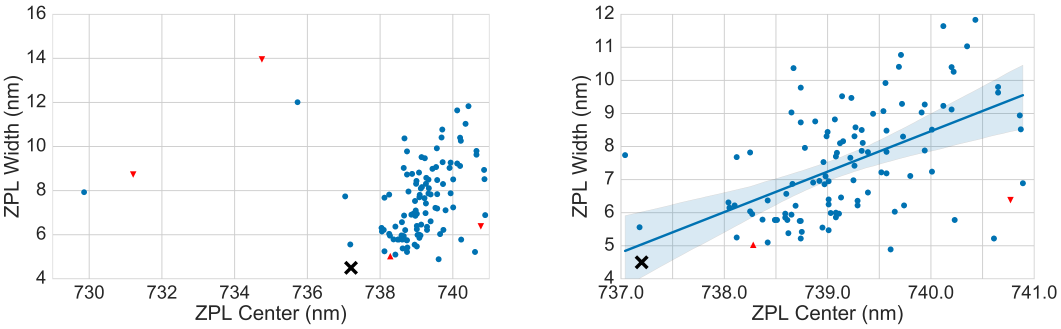

(a) **(b)**

Figure 6.6: (a) A zoom into group V. While many data points exhibit larger center wavelengths (i.e. a redshift) than the ideal SiV center in bulk, only few exhibit shorter center wavelengths (i.e. a blue-shift). (b) Zooming further into group V, a clear trend of broader ZPL linewidths for larger ZPL center shifts is visible. The line is a linear regression to all data points between 737 nm and 741 nm which exhibit a linewidth bigger than 4 nm.

static and material strain. As discussed in Section 5.2.3, we measured the Raman shift of samples insitu70 and implanted250ao. These measurements indicate strain in the diamond lattice in the range of -8.33 GPa to 5.27 GPa. In the following, we first discuss the stress/strain shift mechanisms for the SiV center before we compare theoretically derived strain shift coefficients to the mentioned range of ZPL shifts.

To gain insight into the strain mechanism for SiV centers in diamond, we perform ab initio Kohn-Sham density functional theory (DFT) calculations on the strain ZPL shift coupling parameters. The unstrained model of the negatively charged silicon-vacancy center (SiV^-) in bulk diamond is constructed starting from a 512 atom pristine diamond simple cubic supercell within the Γ point approximation. Here the Γ point refers to the center of the Brillouin zone. The Γ point sampling of the Brillouin zone has proven to be adequate for defects in 512-atom supercells [145, 146] providing a sufficiently converged charge density. The SiV^- defect has $S = 1/2$ and it is found to have D_{3d} symmetry with an axis oriented along $\langle 111 \rangle$ [82]. Standard projector augmented-wave (PAW) formalism together with plane waves are applied, as implemented in the Vienna Ab initio Simulation Package (VASP) code [147–150]. The geometry optimization is carried out within the constructed supercell by using the Perdew-Burke-Ernzerhof (PBE) DFT functional [151]. A 420 eV cutoff is applied for the wave function expansion and a 1260 eV cutoff for the charge density. The geometry of the defect is optimized until the forces were lower than 10^{-6} eV Å^{-1}. The D_{3d} symmetry is preserved for both the ground state and the excited state after relaxation.

The ground state of the defect is found to have electronic configuration $e_u^4 e_g^3$ (^2E_g)

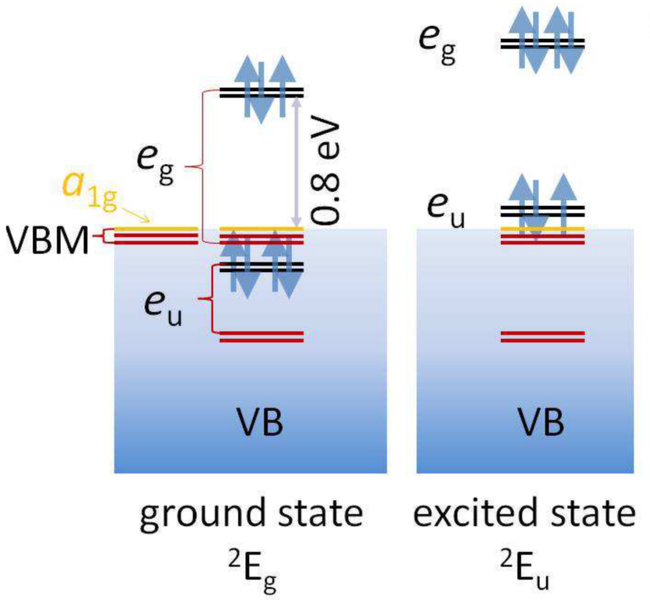

Figure 6.7: Schematic diagram of the ground and the bright (optically allowed) excited state of the negatively charged SiV defect in diamond. The valence band (VB) resonant states play a crucial role in the excitation. For the sake of simplicity, the spin-polarization of the single particle levels are not shown. Figure and caption reproduced from [87]

while the excited state is modeled by promoting one electron from the e_u to the e_g level and presents electronic configuration $e_u^3 e_g^4$ (^2E_u), see 6.7. Both these states are dynamic Jahn-Teller systems [81, 84]. The optical signal of the defect (ZPL) can be calculated as the lowest excitation energy by the constraint DFT approach (CDFT) [152]. According to CDFT one electron is promoted from the ground state to a higher level leaving a hole behind. The interaction between the electron and the hole is included in the procedure. The ZPL energies were obtained by taking the total energies of the optimized geometries in the ground and excited state.

The strain on the defect structure is simulated by applying a compression to the supercell along a well defined direction. The strained supercells are obtained by compressions along ⟨100⟩, ⟨110⟩ and ⟨111⟩. We also study the configuration produced by a hydrostatic pressure, which consists in subjecting the cell to the same compression along the three directions. After introducing the strain along the directions, the ZPL energies were calculated for each strained supercell. Finally, we obtained data points on the calculated ZPL energies vs. the applied strain. These ZPL energies correspond to the optical transition between the lower branch levels of the ^2E_u and ^2E_g doublets. We note that additional calculations were performed for the ⟨100⟩ and ⟨110⟩ strained supercells by using the screened, range-separated, non-local hybrid density functional of Heyd-Scuseria-Ernzerhof (HSE06) [153, 154] and we found good agreement with the PBE values.

Nudged elastic band (NEB) calculations [155] by HSE06 were performed in order to calculate the energy barriers in the ground state in strained supercells. The barrier energies between the C_{2h} configurations stayed under 10.0 meV which implies small change in the adiabatic potential energy surface around the D_{3d} symmetry upon the applied strain. As a consequence, the Ham reduction factor in a strained SiV center will minutely change with respect to that of an unstrained SiV center [156]. This suggests that the observed ZPL shifts upon stress are directly strain related, and the contribution of the change of the effective spin-orbit coupling to the ZPL shifts is minor.

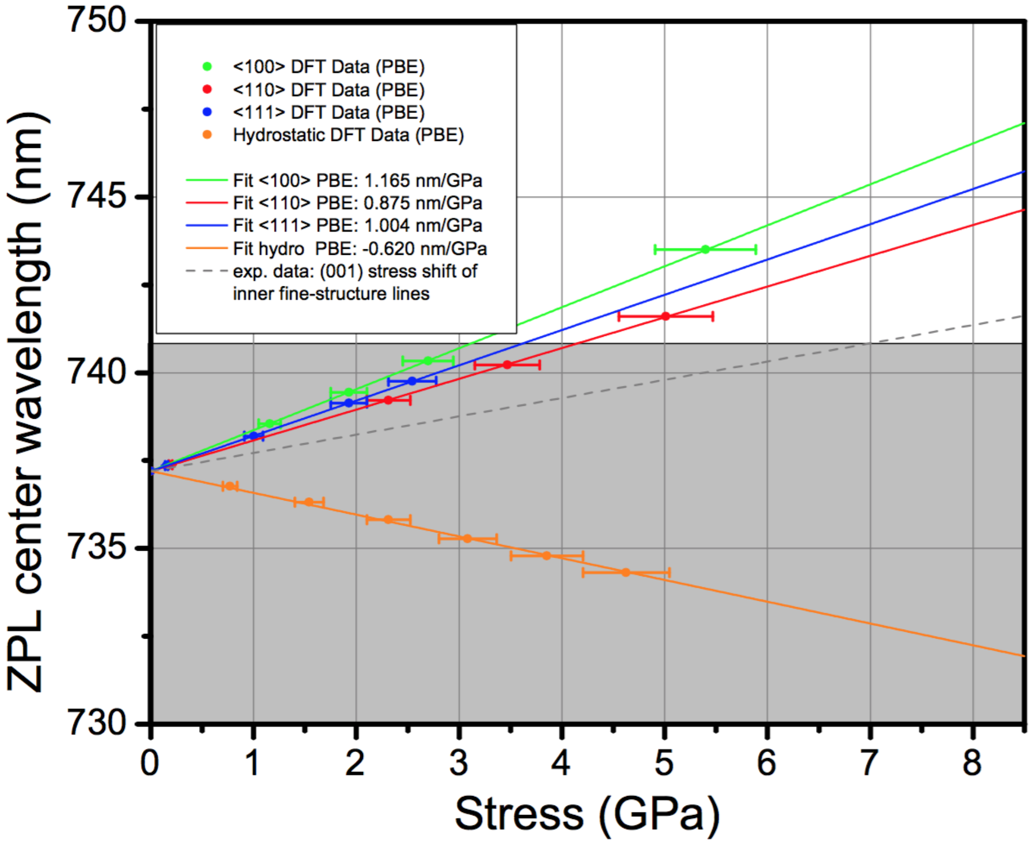

Figure 6.8: Calculations of the wavelength of the SiV center ZPL in dependence of pressure. Markers: DFT calculated pressure with PBE and HSE functionals; Lines: linear fits to the calculated points. Hydrostatic-type pressure causes a moderate blue shift whereas uniaxial strain causes larger redshift with different magnitudes depending on the direction of the strain. Grey line: experimental stress shift data for ⟨001⟩ uniaxial stress and inner fine-structure line of the SiV center. Grey area: range of ZPL center wavelengths of group V.

The data points in Figure 6.8 show ZPL center wavelength shifts calculated with the method outlined above. For comparison with experimentally determined stress data the strain values of the theoretical calculation were converted into stress assuming a simplified model where diamond is approximated as an isotropic linear elastic material. In this case stress σ is related to strain ϵ via Young's modulus as

$$\sigma = E\epsilon. \tag{6.1}$$

This assumption is pragmatic as we do not know the orientation of stress in the nanodiamonds from the Raman measurements but only its modulus. The values of E vary considerably among different diamond materials [157] but even nanocrystalline diamond may obtain a large Young's modulus $E \geq 1000\,\mathrm{GPa}$ [158]. As an average value for the nanodiamond size used in our investigations we assume $E = (1000 \pm 100)\,\mathrm{GPa}$ [157]. The calculated data points were extrapolated by linear fit functions to yield stress shift coefficients for the range of stress (up to $\approx 8.5\,\mathrm{GPa}$) found in the nanodiamonds. The grey area covers the wavelength range of experimental ZPL wavelengths measured within group V. The dashed grey line represents stress-shifts of SiV center emission lines at low temperatures derived from the only experimentally measured stress shift coefficient for the SiV center under uniaxial stress in $\langle 001 \rangle$ [84, 99]. The measurements of [99] were performed at 4 K and reveal the shifts of the SiV center fine structure lines: the outer lines of this fine structure shift with about $4\,\mathrm{nm}\,\mathrm{GPa}^{-1}$ ($2.23\,\mathrm{THz}\,\mathrm{GPa}^{-1}$, not shown here), whereas the inner lines shift with only $0.52\,\mathrm{nm}\,\mathrm{GPa}^{-1}$ ($292\,\mathrm{GHz}\,\mathrm{GPa}^{-1}$, denoted as dashed line). The room temperature spectrum, however, is mostly governed by the inner line “C” of the spectrum [142], i.e. the line with second highest wavelength, corresponding to the optical transition between the lower branch levels of the ^2E_u and ^2E_g doublets as used in the DFT calculations. We find that the calculated uniaxial stress shift coefficients match well the experimentally obtained value (dashed line) and both coincide well with the range of measured red-shifted ZPLs of group V (grey area). We thus interpret the ZPL shifts of group V as originating from level shifts due to uniaxial strain. Furthermore, the calculated ZPL shifts due to hydrostatic pressure coincide well with the range of the blue shifted ZPLs that we observe in group V. The fact that we see only few blue-shifted ZPLs might be due to reason that pure hydrostatic pressure is rarely observed and overlayed by uniaxial stress in the nanodiamonds. On the other hand, the measured shifts in group H are too broad to be solely explained by strain in the diamond. A potential explanation for the very inhomogeneous distribution of defect center ZPL center wavelengths could be the association of SiV centers with a further nearby defect, such as a vacancy, or a modified SiV complex such as SiV:H [159].

Zooming in to group V, another effect becomes visible (Figure 6.6b): With increasing ZPL center wavelength, the linewidth becomes broader. As discussed above, a red-shift of the ZPL is linked to increasing uniaxial strain. Thus we conclude that the ZPL linewidth too is affected by strain in the diamond lattice. Here, a modified electron-phonon coupling [160] causes increased uniaxial stress, resulting in larger linewidths. A similar effect has been previously observed for SiV centers at cryogenic temperatures [142].

To conclude, we are able to explain the distribution of ZPL center wavelengths in group V very consistently with theoretical predictions based on perturbative shifts due to strain in the diamond lattice. On the other hand, we have to assume that group H is comprised of modified SiV centers, the structure of which is currently unclear.

6.1.2 Sideband

It is known that the photoluminescence spectra of SiV centers in nanodiamond are dominated by the zero-phonon-line. As a result phonon side band contributions remain small, a fact expressed in large Debye-Waller factors of over 70 % established previously [85, 161]. Our own measurements are consistent with these of emitter H1 and emitter V1 results. We also find distinct sideband peaks in many SiV center photoluminescence emission spectra. The investigated emitters exhibit two different structures of sideband spectra: The spectra in group V exhibit one strong sideband peak, spectra in group H exhibit several weaker sideband peaks. Figure 6.9a and Figure 6.9b illustrate the respective observations.

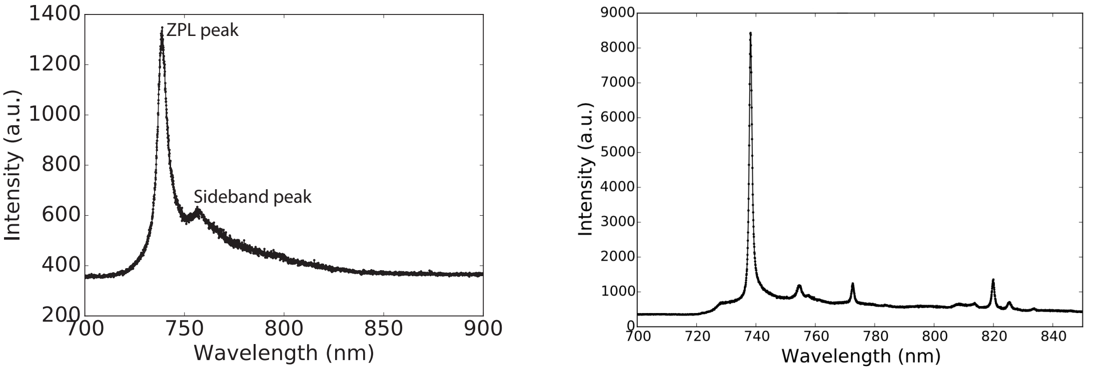

(a) (b)

Figure 6.9: Representative spectra of emitters showing single (a) and multiple (b) side band peaks. The former belong to group V, while the latter are members of group H.

Most of the spectra in group V exhibit a characteristic shape, composed of the ZPL and one strong sideband peak. 70 % of the photoluminescence spectra with one distinct sideband peak exhibit a shift of the sideband peak from the ZPL between 37 meV to 43 meV. The range of line shifts for the prominent sideband peak coincides with a well-known feature at 42 meV, associated with SiV centers [99, 162], but also to a larger number of optically active defects [99]. The occurrence of this 42 meV sideband feature for a large number of defects and the absence of isotopic variations [107], favors an assignment as non-localized lattice vibration. We furthermore observe that the dominant sideband peak shifts towards smaller distance from the ZPL for increasing ZPL center wavelength, i.e. increasing strain.

Figure 6.10 presents a linear fit to data for emitters in group V.. The low phonon energy of the sideband feature and its shift with strain might arise from a local “softening” of the crystal lattice in the vicinity of a defect [99].

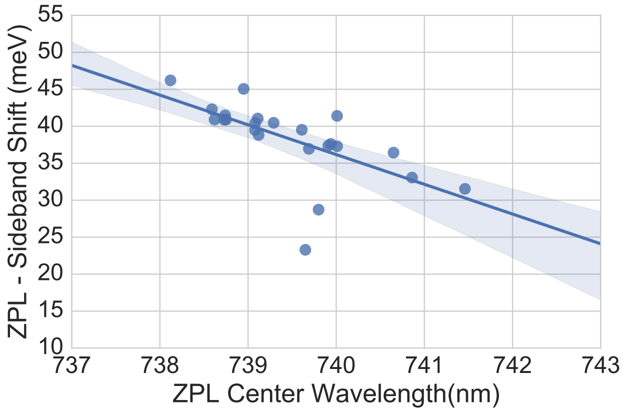

Figure 6.10: Shift of dominant sideband peak from the ZPL in spectra of SiV centers (group V, samples insitu50, insitu70, insitu100) vs. ZPL center wavelength. The linear fit shows that the shift decreases with increasing ZPL center wavelength, i.e. with increasing strain and exhibits a slope of $(-4 \pm 1)\,\mathrm{meV\,nm^{-1}}$. The shaded area is the 95 % confidence region.

A recent study [163] suggests that the 42 meV mode, similar to other broad phonon side band features, originates from a resonance attributed to phonons causing the dynamical Jahn-Teller effect with SiV centers [164]. As the Jahn-Teller coupling varies with strain it is also expected that the resonance shifts accordingly.

In the spectra of group V, we do not observe a typical SiV center sideband feature at 64 meV, attributed to a local vibration of the silicon atom, frequently much stronger than the 42 meV sideband peak. A possible explanation is, that the lattice mode at 37 meV to 43 meV is so strong that the local vibrational mode at 64 meV cannot be separated from the tail of the lattice mode. In group H we observe many spectra which exhibit several peaks within the spectral range of our detection range between 710 nm to 900 nm. The challenge arises to unequivocally distinguish between peaks stemming from a phonon sideband and peaks stemming from shifted, less intense SiV center ZPLs.

Interestingly, we assert a tendency for peaks to accumulate at a shift of around 43 meV, 64 meV, 150 meV and 175 meV, as shown in Figure 6.11. This pattern in the phonon side band of group H is consistent with side band shifts reported in [96, 99, 161].

The possibility exists, that some these peaks believed to be phonon side bands are actually shifted ZPLs stemming from other SiV centers. To address this question, we perform photoluminescence measurements at cryogenic temperatures.

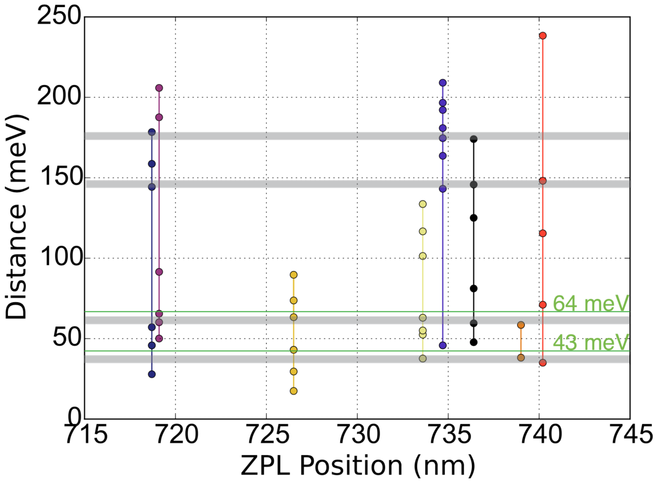

Figure 6.11: This plots shows sideband peaks attributed to different ZPL center wavelengths, with respect to the sideband peak's shift. The ZPL center wavelength is visualized on the x-axis, the respective sideband peak shifts on the y-axis. Therefore, data points aligned on a vertical line belong to the same spectrum. For better visibility, all data points of one spectrum are colored in the same color. Areas shaded in grey represent an accumulation of sideband shifts. The green lines indicate distances with 43 meV and 64 meV respectively.

6.1.3 Cryostatic Measurements

At cryogenic temperatures phonon side band contributions vanish, allowing a focused investigation of zero-phonon-lines. In particular, for SiV centers a four-way splitting of the zero-phonon-line is expected, see Chapter 1. To conduct low-temperature measurements, we used a confocal setup similar to the one described in Chapter 3. It differs merely by the fact that the sample is efficiently cooled to 4 K using a cryostat.

In Figure 6.12 measurements of two individual nanodiamonds are shown, both situated on sample insitu70o. Figure 6.12b and Figure 6.12d show spectra recorded at cryogenic temperatures while Figure 6.12a and Figure 6.12c show spectra recorded at room temperature for comparison. Instead of the four-fold degeneracy expected for SiV centers in low-strain diamond, the cryogenic measurements indicate a multitude of various lines. The observation is best explained by the presence of several SiV centers which are subject to varying levels of strain in their local lattice neighborhood. Given the fact that zero-phonon-lines are found spread over a significant range of wavelengths, a non-negligible impact of lattice strain on SiV center luminescence is revealed.

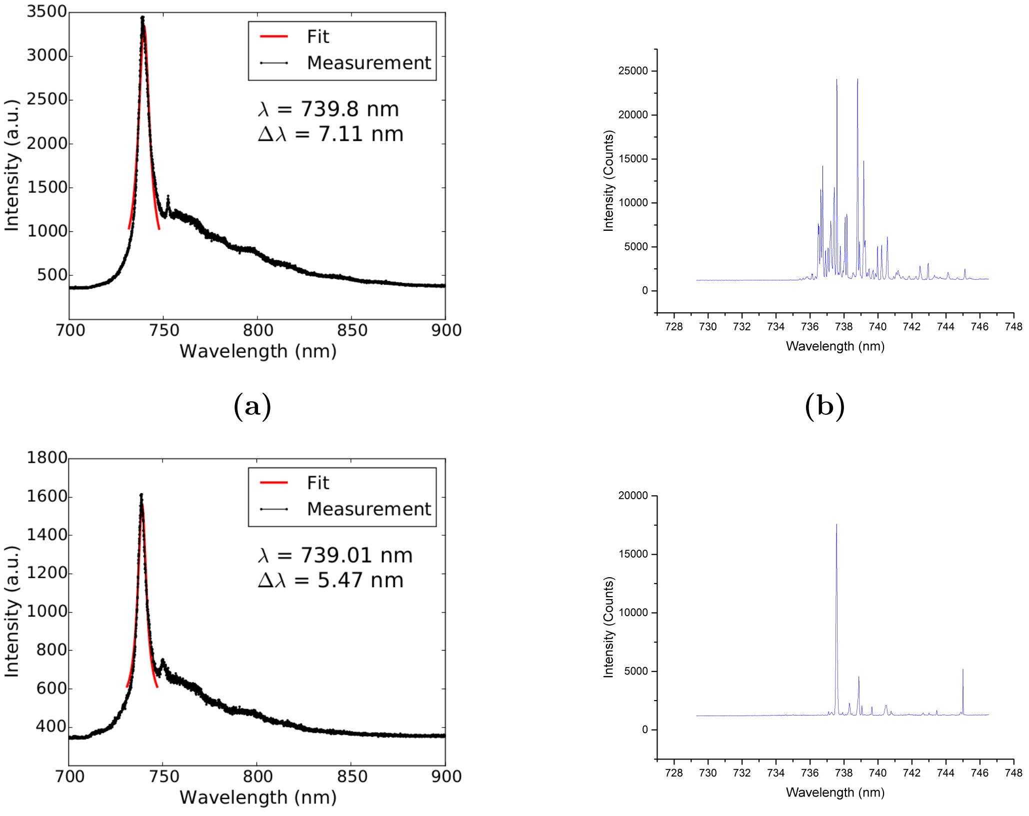

(a) (b)

(c) (d)

Figure 6.12: Comparison of spectra taken at room-temperature (l.h.s) and at cryogenic temperatures (r.h.s). At low temperatures a multitude of lines is revealed indicating several SiV centers embedded in a strained lattice neighborhood.

6.2 Photon Correlation Measurements

The investigated SiV centers exhibit count rates of a few thousand to a few 100 000 counts per second (cps). We carried out measurements of the photon statistics and found that about 3 % of luminescent nanodiamonds contain single color centers. These measurements show, that the probability of finding a single emitter does not correlate in any way with the center wavelength or the linewidth of the ZPL. We found several single SiV centers with an anti-bunching dip down to about 0.2 and attribute the residual $g^{(2)}(0)$ value to background fluorescence from the diamond host. For the utilized nanodiamonds a background measurement without simultaneously measuring SiV center photoluminescence is infeasible, because the laser spot size is bigger than the nanodiamond, i.e. the SiV center will always be excited when the nanodiamond is illuminated. Therefore, the background is estimated from the sideband of SiV center spectra. The measured lifetimes of the single SiV centers are in the range of about 1 ns to 9 ns, which is of the same order as previous research suggests [78, 99].

Figure 6.13 shows the $g^{(2)}$ functions of one emitter of group H and one emitter of group V. The former emitter's spectrum is shown in Figure 6.14a, and denoted emitter H2. The latter is the same as emitter V1 introduced in Section 6.1.

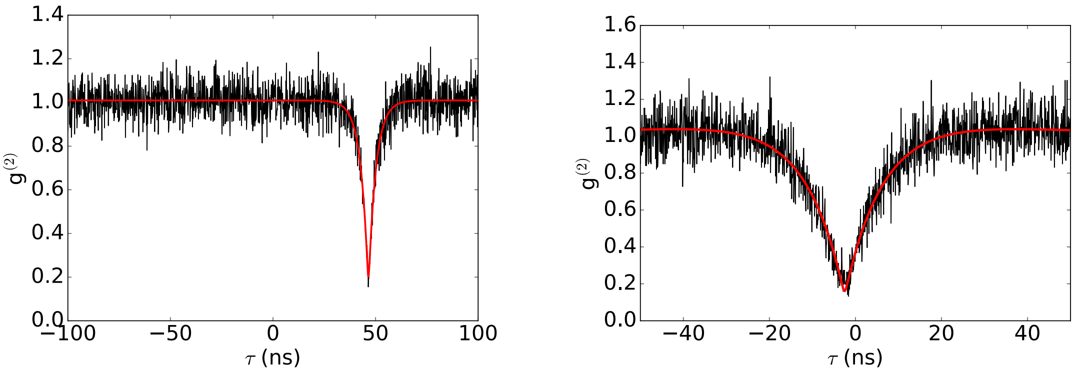

(a)

(b)

Figure 6.13: (a) Intensity autocorrelation function of an emitter in group H. (b) Intensity autocorrelation function of emitter V1 at an excitation power of 200 µW. Saturation power is 1 mW.

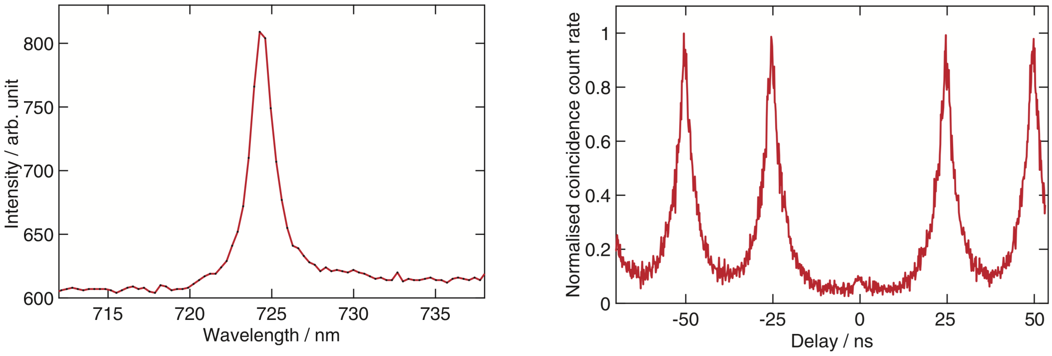

(a)

(b)

Figure 6.14: (a) Spectrum of emitter emitter H2. The center wavelength amounts to 724 nm and the linewidth to 2.0 nm. (b) Pulsed $g^{(2)}$ function of the same emitter. $g^{(2)}(0)$ amounts to 0.2. Figures reproduced from [41].

Figure 6.13a shows the photon correlation function of emitter H2 under continuous wave excitation. The shift of the dip to $\tau = 50\,\mathrm{ns}$ originates from a path length difference of the two detection paths in the Hanbury-Brown and Twiss setup. The $g^{(2)}(0)$ value of the fit is 0.20.

We also performed measurements with a pulsed laser, which is a prerequisite for a direct link between the high photon flux levels of the classical regime and low photon flux levels in the quantum world [13, 41], as mentioned in Chapter 1. The pulsed second-order correlation at zero delay $g^{(2)}(0)$ are calculated by integrating photon counts in the zero-time-delay peak and dividing by the average of the adjacent peaks.

The excited state lifetime of the emitter was determined to be (3.8 ± 0.1) ns, see Figure 6.15. For this, the emitter is excited by a pulsed laser (PiL069XSM from Advanced Laser Diode Systems A.L.S. GmbH) produces short optical pulses of less than 50 ps at a maximum repetition rate of 80 MHz and a wavelength of 685 nm [41]. The measured time intervals between the optical pulse and the detected fluorescence light yields the exponentially decaying lifetime of the excited state. The lifetime of the emitter is the time interval after which the number of N_0 excited emitters decreases to N_0/e.

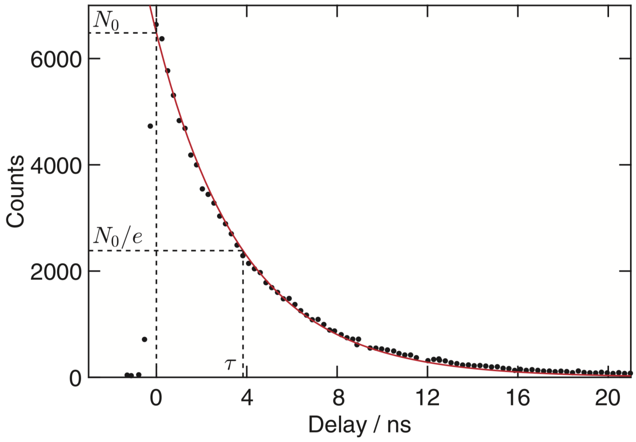

Figure 6.15: Lifetime measurement of emitter emitter H2. The lifetime of the emitter is the time interval after which the number of N_0 excited emitters decreases to N_0/e. Figure reproduced from [41].

An important characteristic of single photon sources is their photon count rate at saturation. The count rate $I(P)$ as a function of the excitation power P is given by

$$I(P) = I_\infty \frac{P}{P + P_{sat}} + c_b P. \tag{6.2}$$

Here I_∞ refers to the maximal photon count rate, while the saturation power is denoted by P_{sat}. These two quantities are parameters determined by fitting count rates $I(P)$ measured at different excitation powers P. The added term $c_b P$ takes into account the linear increase of background fluorescence from the diamond host material at higher excitation powers. When background effects are negligible, this term can be omitted.

Figure 6.16 depicts the saturation curve of emitter V1. The saturation count-rate amounts to (340 ± 20) cps at a saturation power of (1.0 ± 0.1) mW. Figure 6.13b

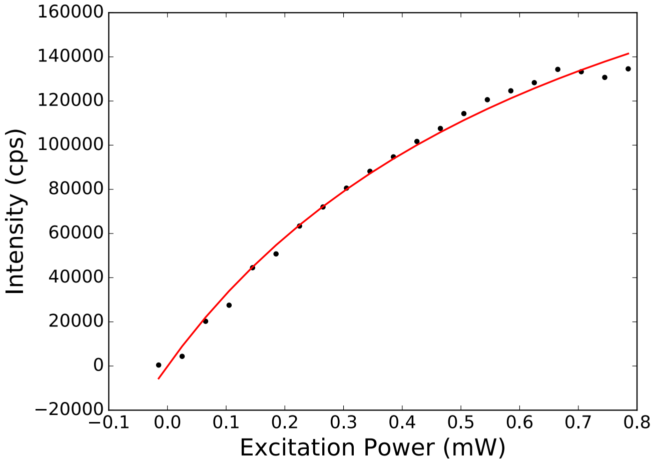

Figure 6.16: Saturation measurement of emitter emitter V1.

shows the $g^{(2)}$ function of emitter V1 at an excitation power of 200 µW, which is 20 % of the emitter's saturation power $P_{sat} = (1.0 \pm 0.1)\,\mathrm{mW}$. The $g^{(2)}(0)$ value yields 0.16. It is a $g^{(2)}$ measurement representative of single SiV centers. It is well below 0.5, indicating single photon emission. The non-vanishing $g^{(2)}(0)$ value is caused by background fluorescence of the diamond. The lifetime of the excited state of this emitter is $(9.2 \pm 0.2)\,\mathrm{ns}$. It is the highest excited state lifetime we measured within this work.

Several nanodiamond photoluminescence spectra contain multiple narrow distinct peaks at different wavelengths. This circumstance is attributed to nanodiamonds containing more than one SiV center, each of which is subject to a different ZPL wavelength shift. We choose narrow bandpass filters to perform independent measurements of each individual peaks of such a spectrum. As a result it is possible to measure $g^{(2)}(0)$ values below 0.5 for each of these narrow peaks. Hence the individual peaks are identified as single emitters with a different ZPL center wavelength.

We do not see a systematic difference regarding the photon autocorrelation functions of group H and group V, both reach similar $g^{(2)}(0)$ values. Also, the timescales of the excited state lifetimes coincide.

6.3 Photostability

As mentioned in the previous section, the single photon count rates observed from the investigated SiV centers varies strongly between a few thousand to a few 100 000 cps. To further investigate the count rate, the luminescence time trajectory of the emitters which exhibit a dip at $g^{(2)}(0)$ is evaluated. It is found that some of the observed emitters exhibit fluorescence intermittence, also called blinking. Figure 6.17 illustrate the effect. Blinking is attributed to temporal ionization of the color center during optical excitation, forming an optically inactive charge state [42, 87, 165]. Therefore the emitters change between states of higher and lower emission, i.e. brighter and darker states, called blinking levels.

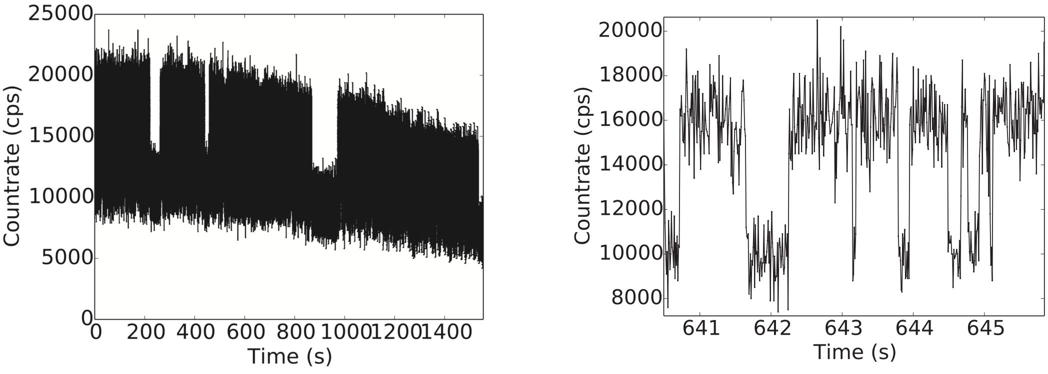

(a)

(b)

Figure 6.17: (a) Time trace of the single emitter H1, which exhibits strong blinking. The variation of the count rate in the upper state is attributed to a drift of the setup. (b) Detail of the time trace of the same emitter.

The photon count time trace of emitter H1 is shown in Figure 6.17. In the overview picture (Figure 6.17a), a few blinking dips can be seen exhibiting time intervals of up to a few minutes. The fact that the count rate never drops down to the dark count rate lets us assume, that there are at least two SiV centers present, one exhibiting fluorescence intermittence and one exhibiting a stable emission. When zooming in, shorter time intervals are observable (Figure 6.17b). The time intervals range from a few tens of milliseconds up to a few seconds with a few outliers exhibiting very long time intervals up to a few tens of seconds.

The bright and dark times exhibit different probability distribution functions and with that, different characteristic time constants. In Figure 6.18 the time intervals of the emitter are shown as small vertical dashed red lines and solid blue lines for the bright and dark state respectively. Outliers with very long time intervals are ommited here. The dashed lines are kernel density estimators of the distribution of the respective time intervals. This implies that every data point is represented with a Gaussian function and the resulting functions are added up to model the whole data. The red solid line is an exponential fit of the distribution of time intervals in the bright state. The high p-value of 0.92 confirms the goodness of the fit. The median time interval in the bright state obtained by the exponential fit amounts to 0.09 s. While other literature on solid state quantum emitters reports an exponential probability distribution for both time intervals in bright and dark states [166, 167], we found a log-normal probability distribution for the time interval in the dark state. The solid blue line in Figure 6.18 is a log-normal fit of the distribution

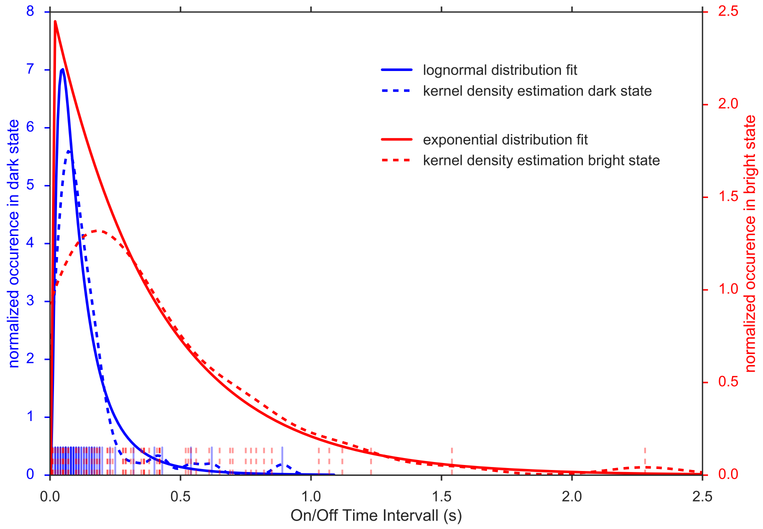

Figure 6.18: Time intervals of the single emitter exhibiting the highest blinking rate in the bright (red) and dark (blue) states. Each flank of the blinking state was individually read out from the photoluminescence time trace. On the horizontal axis small vertical lines represent the individual data points of the bright/dark time intervals. The blue and red dashed curves represent kernel density estimations of the distribution of time intervals of the dark and bright states, respectively. The y-axis is scaled to the normalized kernel density estimate. The red solid line is an exponential fit of the bright state time intervals whereas the blue solid line is a log-normal fit of the dark state time intervals. These fitting functions were chosen because they provide the best agreement with the data using a Kolomogorov-Smirnov test with respect to other functions (p-values: bright state (red) 0.92, dark state (blue) 0.77).

of the time intervals in the dark state. A Kolomogorov-Smirnov test yields a p-value of 0.77 for the log-normal fit and is by far the best model to describe the data distribution. For comparison: The p-value of an exponential fit amounts to 0.36. The median time interval in the dark state obtained by the log-normal fit is determined as 0.10 s, therefore being close to the median time interval in the bright state. Very long time intervals are not shown in the plot for better visualization of the small timescales, however these long time intervals are included in the fit. The longest measured time interval amounted to 41.14 s and occurred in the dark state.

Measurements of blinking time intervals in [165] and [42] report time intervals between about 0.03 s to 1 s, and 0.1 s to 2 min, respectively. These findings are in good agreement with our measurements.

In general, excitation and emission processes are mediated by charge separation (i.e. excitons). If an electron or hole is localized far enough that there is sufficiently negligible overlap with the wave function of the remaining carrier, blinking occurs [168]. We explain the observed blinking as a manifestation of the local crystal disorder due to dislocations and impurities which act as a trap for the excited electron and therefore switch the emitter to the dark state. The capture of the electron of the exciton by traps due to local crystal disorders may inhibit recombination and therefore induce the dark state [166]. The assumption that dislocations and impurities are responsible for blinking emitters is in agreement with our findings reported in Chapter 5.

Research of blinking rhodamine molecules confirms power law distributed bright state times and log-normal distributed dark state times [169]. The log-normal distribution is explained by a Gaussian distribution of activation barriers of the electron transfer to trap states in the surrounding material [170]. It hints towards a recapture of the electron via multi-phonon relaxation channels.

7 Coupling of Nanodiamonds to Photonic Structures

In the previous chapter, we reported on photoluminescence properties of different sets of SiV centers. Across the available samples, emitters were found to exhibit considerable variations in wavelength, linewidth as well as intensity of zero-phonon-lines. This broad variety in combination with the ability to examine SiV centers individually opens up the possibility to preselect emitters according to desired spectroscopic parameters, such as narrow linewidths, high count-rates and single photon emission.

Once suitable emitters are identified, their host nanodiamonds can be moved with precision using pick-and-place methods. In particular, SiV centers may be transfered and coupled to photonic structures where their extraordinary properties can be exploited to create a single photon source. Such sources are useful tools, widely required for applications in metrology and various quantum technologies such as quantum computing or quantum cryptography.

In the scope of this thesis, nanodiamonds including suitable SiV centers were identified and coupled to two different kinds of structures: Vertical-Cavity Surface Emitting Lasers (VCSELs) and plasmonic nano-antennas.

To create a hybrid-integrated single photon source, a nanodiamond containing an SiV center is placed on top of a VCSEL. The SiV center is positioned such that it is directly pumped by the VCSEL output laser beam. Thus, the emission of the SiV center is steered indirectly via the operation of the VCSEL. Through the use of suitable optical filters allowing only SiV center fluorescence light to emerge, a controlled single photon source can be realized. This system is interesting in the context of metrological applications, as it constitutes a promising building block for a portable device ready to calibrate single photon detectors.

Coupling SiV centers to plasmonic nano-antennas aims at enhancing the detectable photoluminescence intensity of an emitter. As described in previous chapters, not only ZPL position and linewidth, but also the photoluminescence intensity varies strongly among individual SiV centers. As mentioned we aim to add momentum to the adaption of the quantum candela. To this end single photon sources are needed as calibration devices for the development of photon-counting detectors. Single photon sources exhibiting a high intensity are favorable for calibration purposes [41]. Furthermore, plasmonic antennas can be used to tune the emitter's photoluminescence spectrum.

7.1 Additional Experimental Methods

Coupling SiV centers to photonic structures requires specialized experimental methods. A range of challenges must be overcome: First, additionally to the spectroscopic preselection, the pick-and-place process poses further technical restrictions on the suitability of a host nanodiamond. The size of the host nanodiamond has to be bigger than 70 nm and they have to lie isolated on the substrate surface, i.e. with a distance of about one micrometer. This substantially reduces the number of SiV center candidates ready to be coupled to photonic structures. Another challenge is posed by accurately picking up a single nanodiamond hosting an SiV center and placing it precisely at a specified position within a given photonic structure. Furthermore, since the SiV center is to function as the photoluminescence emitter, it must not be damaged during the relocation process. To minimize the damage caused by electron radiation, both the dose and the energy are minimized. Hence, the pick-and-place process is performed as fast as possible and with a low acceleration voltage that is just strong enough to see a hazy image of the nanodiamond.

In the context of this thesis we explored the following methods to couple nanodiamonds to photonic structures:

1. Directly spin-coat the target structures with a nanodiamond solution and consecutively look for a structure containing a nanodiamond with an SiV center exhibiting the desired spectroscopic properties. Frankly, this method relies on chance and is only feasible for the application with antenna structures due to the large number of antennas on one substrate. It is not applicable to VCSELs because of their morphology.

2. Identify nanodiamonds containing suitable SiV centers and individually relocate them to the destination structure using a nanomanipulator tip in a scanning electron microscopy to perform a pick-and-place routine. For this method to be effective, nanodiamonds must have a certain size. The obvious advantage of this method is the fact that only the very best emitters are used. Furthermore, the pick-and-place process can be monitored in real-time by the SEM. On the other hand, the electron radiation present during the pick-and-place process may damage the SiV center, introducing a risk of completely invalidating an emitter.

3. Identify nanodiamonds containing suitable SiV centers and individually relocate them to the destination structure using an atomic force microscope to perform a pick-and-place routine. While this method has the advantage that the nanodiamonds are not irradiated with electrons, the disadvantage is that

it is not possible to observe the picking process in real time. As a consequence, the area of the preselected nanodiamond has to be scanned after every pick-up attempt, which is prohibitively time consuming and therefore was not further pursued after initial trials.

In the following we detail the pick-and-place technique since it is the key technique in this chapter. We also discuss the properties of the nanomanipulator and how we identify nanodiamonds suitable for pick-and-place transfer. The pick-and-place process itself is very fickle and difficult to execute correctly. We are grateful for the guidance and support provided by C. Pauly, group of F. Mücklich, Saarland University in addition to operator the nanomanipulator setup itself.

7.1.1 Nanomanipulator

The nanomanipulator used for our experiments (Kleindiek, model MM3A-EM) has a exchangeable tungsten tip mounted inside a Thermo Scientific™ Helios NanoLab™ DualBeam™ microscope. This device combines a focussed ion beam and an electron microscope. The bent nanomanipulator tip can be seen in Figure 7.1 and has 3 degrees of freedom: up/down and left/right both in an arc up to 240°, and 12 mm in/out.

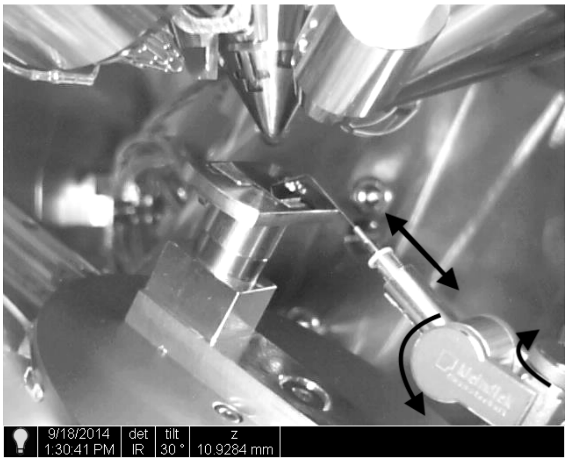

Figure 7.1: Image of the nanomanipulator mounted in the FIB. The black arrows indicate the degrees of freedom of motion of the nanomanipulator. The custom made workbench is situated in the middle of the picture. On top of it, there is a 1 cm^2 substrate with coated nanodiamonds, the nanomanipulator tip pointing to the middle of it. Behind it, there is the target vertical-cavity surface emitting laser. Perpendicular to the workbench, the objective of the focussed ion beam can be seen. The angled cone perpendicular to the top edge of the image is the objective of the electron microscope .

Before using the nanomanipulator, its tip was “sharpened” with a focused ion beam by etching away tungsten with gallium ions. Its final radius of curvature amounts to 100 nm. The sharpening enables the pick-up of nanodiamonds of a size suitable for use with photonic structures. In Figure 7.2a two sharpened tips are shown.

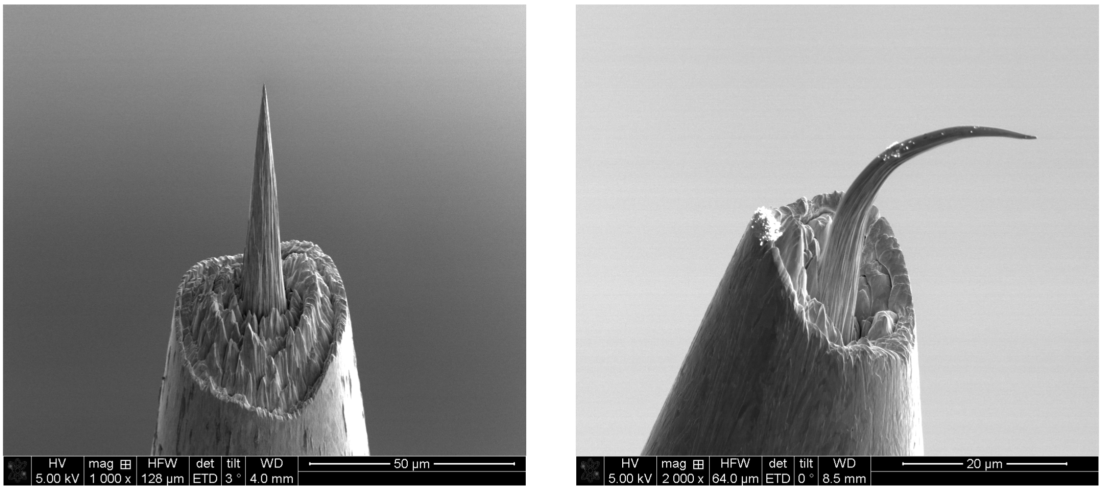

(a) **(b)**

Figure 7.2: Detail of tips used as nanomanipulators. The sharpened tip can be seen projecting out from the original structure. (a) Well-formed tip after sharpening. (b) Bend tip, silently attesting to the use of excessive force. The white dots on the tip are nanodiamonds.

7.1.2 Determination of The Position of Nanodiamonds

Using the confocal setup detailed in Chapter 3 we identified nanodiamonds containing SiV centers suitable for the use in photonic structures. However, to actually move those nanodiamonds to a target photonic structure the SEM setup described in the previous section must be used. This implies that after substrates containing suitable nanodiamonds are mounted in the SEM setup, the same nanodiamonds must be located on the substrate in order for the nanomanipulator to address them correctly. To facilitate this and help locate relevant nanodiamonds, 10 μm^2 cross markers with a nominal depth of 40 nm were milled into the iridium coating of the silicon substrate using the focussed ion beam prior to spin-coating the substrate with nanodiamond solution. The markers were arranged in a regular 11×11 grid covering an area of $0.5\,\mathrm{mm} \times 0.5\,\mathrm{mm}$. Figure 7.3a illustrates a sample array. Typically three arrays of markers were milled per substrate used.

To record the position of a nanodiamond with respect to a cross marker, we used two different methods:

In the first method the confocal setup is used with a white light source illuminating the sample from the side at an acute angle. As a result, the edges of the cross

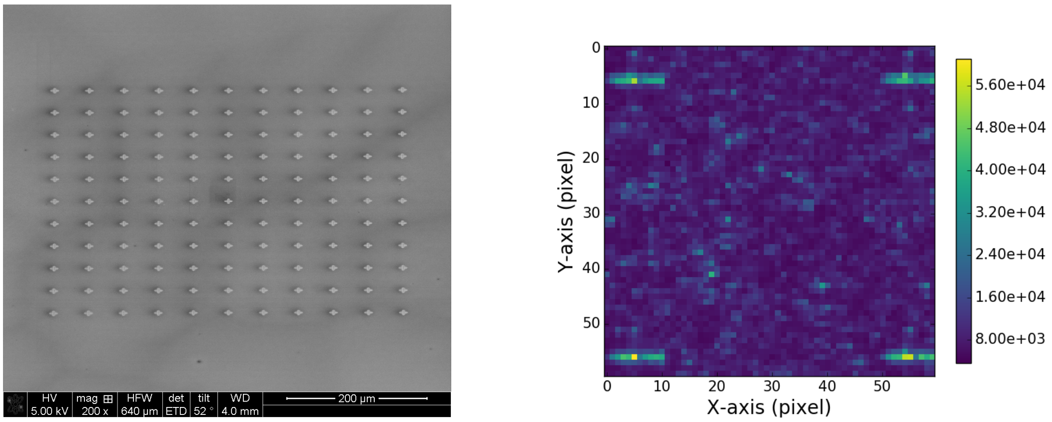

(a) **(b)**

Figure 7.3: (a) Top-view of a regular array of cross markers. (b) White light scan of an area. Cross markers can be seen in an all four corners.

markers become visible in the fluorescence light scan, see Figure 7.3b. After turning the white light lamp off, the same area is scanned again to record the fluorescence from the SiV centers. An overlay of the two images identifies the position of fluorescent SiV centers with respect to the cross markers. The disadvantage of this method is the increased time consumption, as every scan for every subregion of the sample has to be performed twice. As only fluorescence light scans are performed, no information about the size of individual nanodiamonds is available. Furthermore, it remains unknown whether nanodiamonds are present in isolation or close to each other. With this approach, such information is only available in the SEM where the pick-and-place process is conducted. It is only at this later stage, that individual nanodiamonds can be excluded as unusable for the pick-and-place process. For such nanodiamonds the time spend of characterizing its properties was unfortunately wasted.

To mitigate this problem, a more efficient method consists of scanning the substrate first using a commercial laser scanning microscope. The laser scanning microscope is a confocal microscope where the focus of a laser can be used to obtain the height of a structure. When scanning an array of cross markers a gray-scale image is obtained, where the gray value corresponds to the height deviation of a structure. As a result, both the crosses with a nominal depth of 40 nm and the nanodiamonds themselves are revealed as darker shades of gray. In contrast to the previous method, information on the size and isolation of nanodiamonds is accessible. After scanning the substrate with the laser scanning microscope, it is inserted into the confocal setup. While observing the surface with a CCD camera, a specific cross marker is chosen as the starting point for a fluorescence light scan. Comparing the laser scanning microscope image and a fluorescence light scan, fluorescent dots of the fluorescence light scan can be attributed to nanodiamonds in the laser scanning microscope scan. Figure 7.4a and Figure 7.4b illustrate the process.

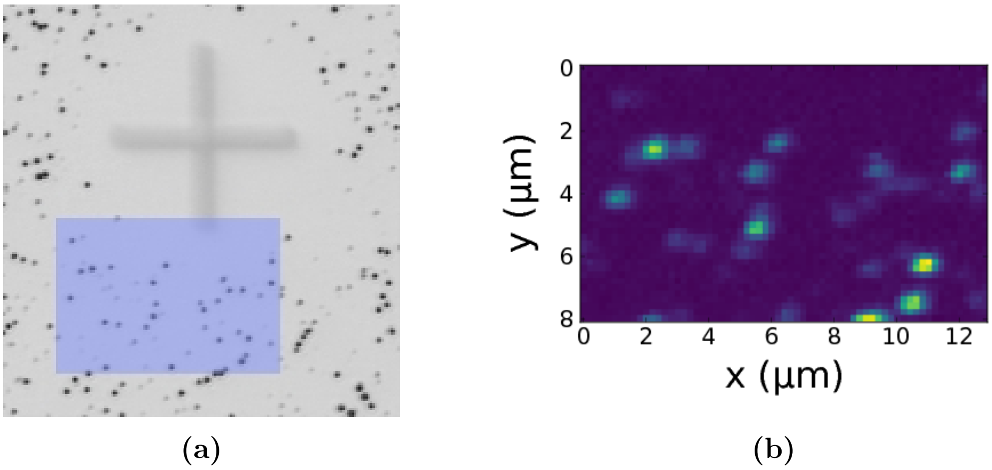

(a)

(b)

Figure 7.4: a) Picture recorded with a commercial high resolution laser scanning microscope. Cross marker is visible as well. The area shaded in blue represents the photoluminescence scan in image b). b) Photoluminescence scan of a 8 µm × 13 µm area corresponding to the blue shaded area in a).

7.1.3 The Pick-And-Place Process

The pick-and-place process [171] aims to transfer a select nanodiamond between two substrates using a nanomanipulator tip mounted inside a scanning electron microscope. The advantage of using a nanomanipulator lies in the fact that the progress of the manipulation process can be visualized directly, allowing for a good control of the operation. Figure 7.5 illustrates the process.

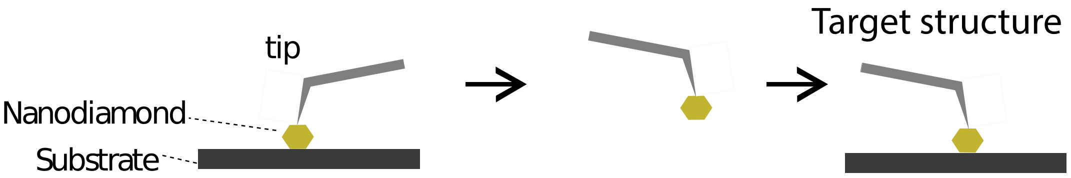

Figure 7.5: Sketch of the pick-and-place process

After we identified nanodiamonds as well-suited for transfer to the target structure, both the substrate with the nanodiamonds and the target structure were mounted inside the SEM. The process was performed using a high resolution mode with a low acceleration voltage of the SEM of 1 keV and a current of 1.7 nA. The tip is approaching the preselected target nanodiamond from above. As the SEM objective is mounted above the nanomanipulator, the proximity the nanomanipulator tip to the nanodiamond is not observable. To enable the tip of the nanomanipulator to pick up a target nanodiamond a precise approach is necessary. To facilitate this difficult procedure, the approach is divided into two stages: A coarse stage and a fine stage.

In the coarse stage the distance between tip and target nanodiamond is indirectly estimated from the shadow the tip itself casts onto the substrate and the focus area, see Figure 7.6. As the tip approaches the target, the shadow of the tip starts to coincide with the nanodiamond position. At this point the fine stage of the approach begins in order to cover the remaining distance. To precisely control the final approach the focus of the SEM is used. The SEM is focused on the nanodiamond, therefore the tip is out of focus and appears blurry. However, as the distance between the tip and the target decreases, the focus must become sharp. Thus the tip must be moved with utmost care until the focus becomes sharp at which point the tip touches the nanodiamond and pick-up can commence. While the process appears straightforward in concept, it is extremely challenging to operate the involved machinery to the required precision. As can be seen in Figure 7.2b it is easy to overshoot the target and to ruin the tip in the process.

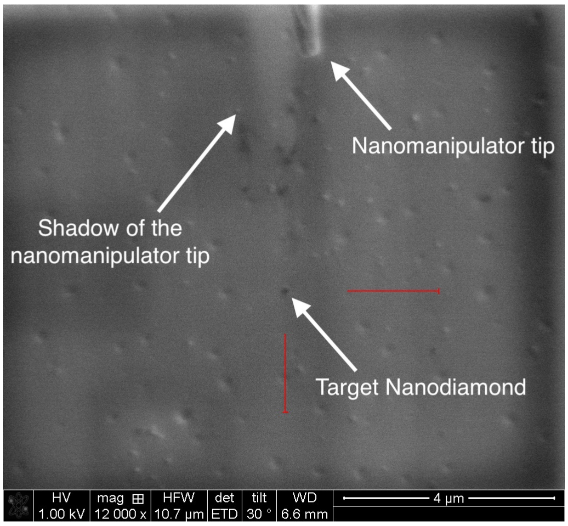

Figure 7.6: Nanomanipulator tip approaching the target nanodiamond. The shadow of the tip is visible.

When performed correctly, the nanodiamond sticks to the tip due to adhesion when the both get in contact, see Figure 7.7a. The nanomanipulator is then moved to the target structure and the approach procedure is applied in reverse. Figure 7.7b illustrates the tip of the nanomanipulator carrying a nanodiamond towards its destination structure. Depending on the material of the target structure, the nanodiamond either sticks to the structure right away due to higher adhesion forces between the nanodiamond and the target structure (as is the case for golden plasmonic antennas). Alternatively, a sideways motion of the nanomanipulator tip must be used in an attempt to strike-off the nanodiamond. Either way, with patience it is possible to place a nanodiamond in a target position within a precision of a few nanometers.

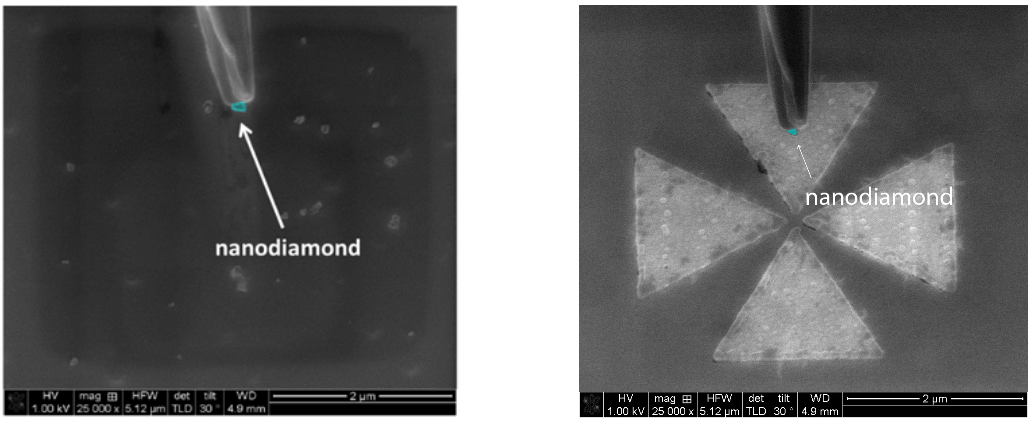

(a) **(b)**

Figure 7.7: (a) Tip of the nanomanipulator after successful pick-up of a nanodiamond. (b) Tip of the loaded nanomanipulator approaching the target structure about to deliver a nanodiamond.

7.2 Coupling SiV Centers to Vertical-Cavity Surface Emitting Lasers

In the context of metrology controllable single photon sources operating at room temperature are an extremely important prospect. Such devices are anticipated to play a key role in the development and calibration of detectors and measurement methods aiming to resolve optical flux down to single-photon resolution [41]. Such single photon sources form a cornerstone of the efforts directed towards the redefinition of the candela in terms of single photons, see discussion in Chapter 1.

Here we attempt to create a hybrid-integrated single photon source by placing a nanodiamond containing a solitary SiV center on-top of a vertical-cavity surface emitting lasers (VCSELs). Using nanodiamonds containing exactly one SiV center is a necessary requirement for the realization of a proper single photon source, however, such nanodiamonds are difficult to identify. Thus, we rely on nanodiamonds containing several SiV centers for a first poof-of-concept implementation demonstrating the validity of coupling emitters to VCSELs.

In our approach a nanodiamond containing SiV centers is situated such that the output laser beam of the VCSEL is used to optically excite the color center. Since the VCSEL laser can be controlled very well, SiV center operation can be steered reliably. Through the use of suitable optical filters allowing only SiV center fluorescence light to emerge, a hybrid-integrated single photon source can be realized in principle.

In the following we give a short discussion of VCSELs. Next we discuss the coupling of SiV centers to VCSELs and report on the optical properties of the resulting hybrid-integrated light source.

7.2.1 Vertical-Cavity Surface Emitting Lasers

A vertical-cavity surface emitting laser is a type of semi-conductor laser [172, 173]. Figure 7.8 illustrates a common design consisting of a p-layer on top and a n-layer at the bottom separated by a so-called active area. When a current is applied across the device, charge carriers migrate towards the active region. Holes act as charge carriers in the p region, whilst electrons carry charge in the n-region. The material properties of the active region is chosen such that when electrons and holes spontaneously recombine, a photon is emitted in the process. Electron-hole pairs can also dissipated via the creation of phonons leading to losses in the form of heat. To define the region for recombination to occur and to control the optical properties of the device, additional thin layers of semi-conducting material can be introduced in the active area. These result in the formation of quantum wells with associated energy levels and resulting preferred transitions with well-defined energies for the recombination of electrons and holes.

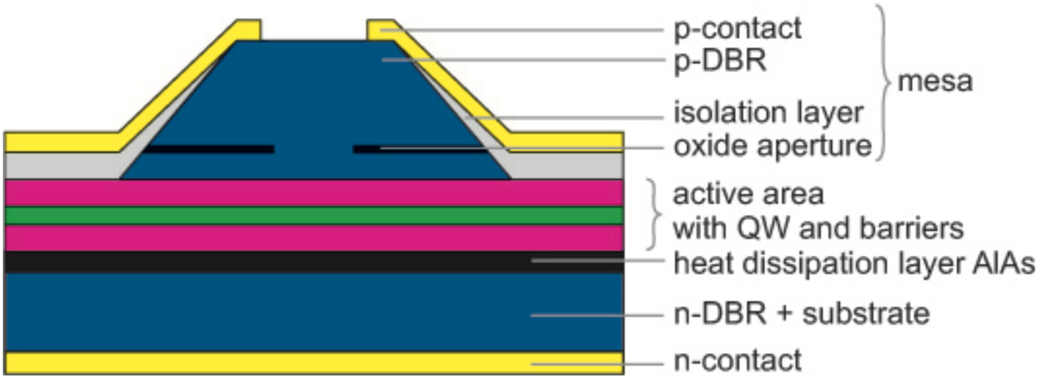

Figure 7.8: Illustration of a VCSEL laser [174]. When a current is applied across the device via contacts (yellow), holes and electrons migrate from the p-region (blue, top) and the n-region (blue, bottom) towards the active region (purple+green, center) where they recombine, emitting photons. A quantum well is inserted in the active region, shaping the recombination process. p-region and n-region are realized as DBRs forming the resonator of the laser. When enough photons are gained by via stimulated emission, a laser beam emerges from the p-region after passing an oxide aperture.

To achieve lasing, stimulated recombination and thus stimulated emission of photons is required. To facilitate this both p-region and n-region are constructed in a layered fashion allowing them to act as highly-efficient distributed Bragg reflectors (DBR). Thus the active region is sandwiched by two mirrors forming the resonator of the laser. Spontaneously emitted photons thus are temporarily trapped continuously interacting with the active region. Provided the presence of sufficient electron-hole pairs, a photon can stimulate their recombination and thus the emission of further identical photons which themselves increase the stimulated emission. If enough identical photons are gained in this process, a coherent laser beam is formed by the fraction of photons escaping the resonator through the p-region. As a result the laser beam produced by a VCSEL is perpendicular to the substrate it resides on.

VCSELs have a range of properties that make them particularity interesting for industrial applications such low power consumption, ease of fabrication and cheap production. As a result, VCSELs are utilized in a broad range of applications including fiber optic communications or precision sensing and are used widely in commonly encountered devices such as computer mice or laser printers [174].

In the context of this thesis VCSELs offer several advantages. Their output beam is perpendicular to the substrate surface and suitable to excite SiV centers. This means that nanodiamonds containing SiV centers can simply be placed on-top of the device. Furthermore their physical size is ideal for the nanodiamonds we work with. The small size of VCSELs will make it easier to deploy the resulting hybrid-integrated light sources in future applications.

7.2.2 Silicon-Vacancy Center in a Vertical-Cavity Surface Emitting Laser

To conduct our research, we received an array of red AlGaInP-based oxide-confined VCSELs from P. Michler, Stuttgart University. The array includes three individually operable VCSELs, two of which, labeled VCSEL Bm4 and VCSEL Bm2 were used in our experiments, see Figure 7.9a.

The VCSELs we obtained use a n-type DBR consisting of 50 pairs of AlAs and $Al_{0.5}Ga_{0.5}As$ mirror pairs while the p-type DBR is formed by 36 $Al_{0.95}Ga_{0.05}As$ and $Al_{0.5}Ga_{0.5}As$ [175]. The active region itself consists of 4 GaInP quantum wells. An oxide aperture in a field node of the standing wave serves as a spatial filter for maximum modal gain by confining the current and the optical mode. The active diameter which is defined by the oxide aperture is 5.8 µm.

The available VCSELs are perfect candidates for the excitation of SiV centers in a hybrid integrated single photon source for several reasons. They exhibit a circular beam profile, have low divergence angle and emit linearly polarized light. Their physical size and the fact, that their output beam is perpendicular to the substrate implies that our nanodiamonds containing nanodiamonds can simply be placed on-top of the structure's light-emitting region using pick-and-place methods, see Figure 7.9b. Thus the VCSEL's output laser can be used to optically excite SiV

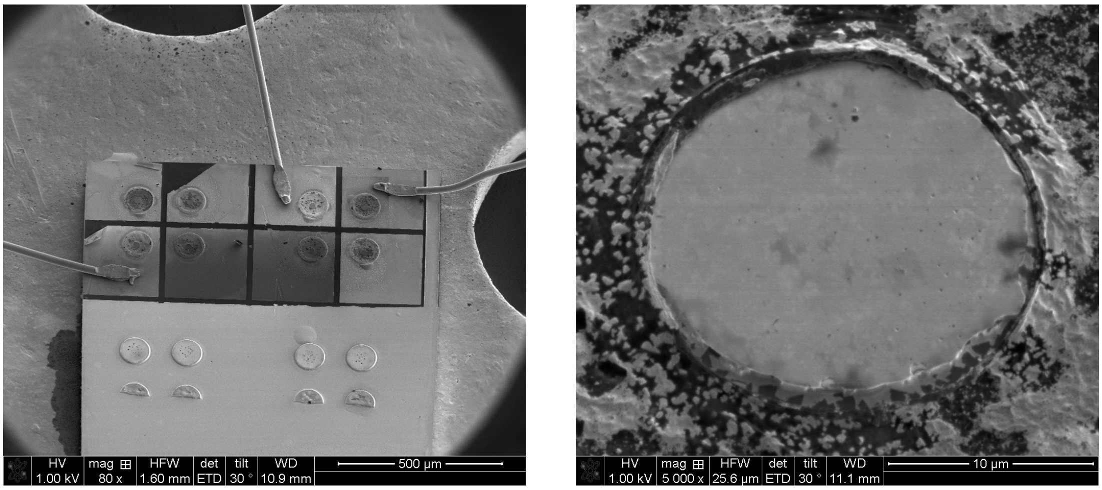

(a) **(b)**

Figure 7.9: (a) SEM image of an array of VCSELs. The three wires are the anodes, which are connected to the top layer (*p*-contact) of the VCSEL. Therefore, three of the VCSEL structures can be operated. VCSEL Bm4 is located in the top right, VCSEL Bm2 to the left of it. (b) Detail SEM image of the top of VCSEL Bm4. The circular middle part is the hole in the *p*-contact through which the top DBR is visible. The smaller active diameter measures 5.8 µm through which the laser light exits the structure and is not visible in the SEM. A successful pick-and-place operation positions a nanodiamond hosting an SiV center directly in the path of the VCSELs laser.

centers.

As a first step towards using VCSELs to excite color centers, VCSEL Bm4 was characterized by the research group providing it. To this end it was operated at currents of 1.5 mA and 3 mA and the resulting lasing wavelength was recorded. The emission spectra showed that the emitted continuous wave laser light to be around 655 nm in wavelength for both currents, see Figure 7.10a. Previous research within the authors group recorded SiV center emission intensity maxima at excitation wavelengths of 720 nm and 680 nm [176], aligning reasonably well with the output wavelength of VCSEL Bm4.

The optical output power of VCSEL Bm4 as a function of the current applied is given in Figure 7.10b. In addition, the resulting voltages are shown. It can be seen that the maximum power of $\approx 0.6\,\mathrm{mW}$ is reached for moderate currents of $\approx 4.5\,\mathrm{mA}$. While the available optical powers are small comparable to using a conventional laser, low powers are sufficient for initial explorations.

The next step consists of selecting a suitable nanodiamond containing an SiV center followed by transferring it on-top of VCSEL Bm4. To this end nanodiamonds 200 nm in size were grown with the CVD method on an iridium coated silicon

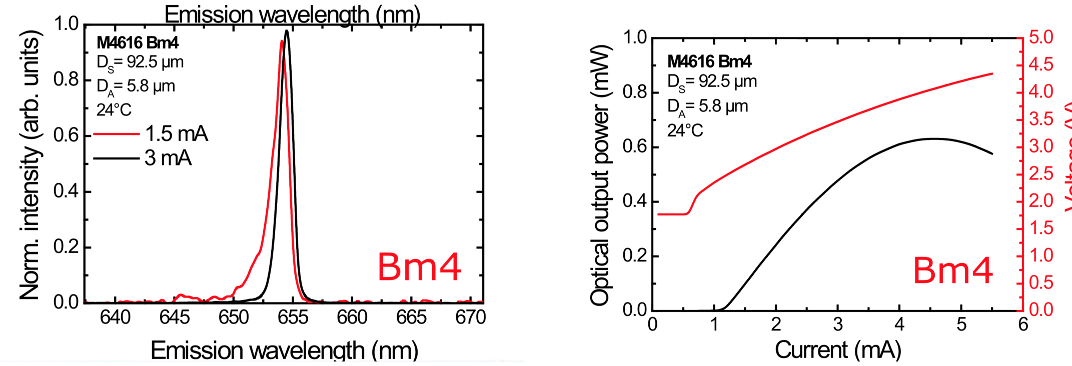

(a) **(b)**

Figure 7.10: (a) Emission spectrum of VCSEL Bm4 at two different currents. (b) Optical output power and voltage of VCSEL Bm4 in dependence of input current. Graphs extracted from a data sheet provided by P. Michler, Stuttgart University.

wafer. We refer the reader to Section 4.2 for details on the process.

Next, using the confocal setup described in Chapter 3 a nanodiamond was identified exhibiting one dominant line at 746.0 nm with a linewidth of 1.9 nm. Its position on the substrate was determined consecutively using a white light laser scan as described in Section 7.1.2. Given the position of the nanodiamond it was then transferred to VCSEL Bm4 and placed precisely in its active, i.e. light-emitting region. The process of introducing an SiV center to another structure is referred to as coupling.

After successful transfer VCSEL Bm4 was inserted into the confocal setup. Using the laser from the confocal setup we checked if the pick-and-place process caused any modification of the spectroscopic properties of the SiV center such as a decrease of the countrate or a modification of the fluorescence light spectrum. During these checks, the VCSEL itself was turned off.

As a first check, we scanned the VCSEL surface in an attempt to localize the introduced SiV center. Figure 7.11a shows the SiV center as a bright dot in the aperture of VCSEL Bm4. For comparison, a Vertical-Cavity Surface Emitting Laser without coupled SiV center exhibits solely background counts which is shown in Figure 7.11b.

The spectrum of the SiV center in the transferred nanodiamond was investigated before and after the pick-and-place process. Figure 7.12 shows that the original spectrum before nanodiamond transfer exhibits one dominant line at 746.0 nm, denoted line A. Furthermore, two minor peaks can be seen. The lower wavelength peak is denoted as line B. Interestingly, after the pick-and-place process, a different picture emerges, as shown in Figure 7.12. The once dominant line A is strongly reduced. The new dominant feature is line B. Note that the countrate of line B remained the same before and after pick-and-place.

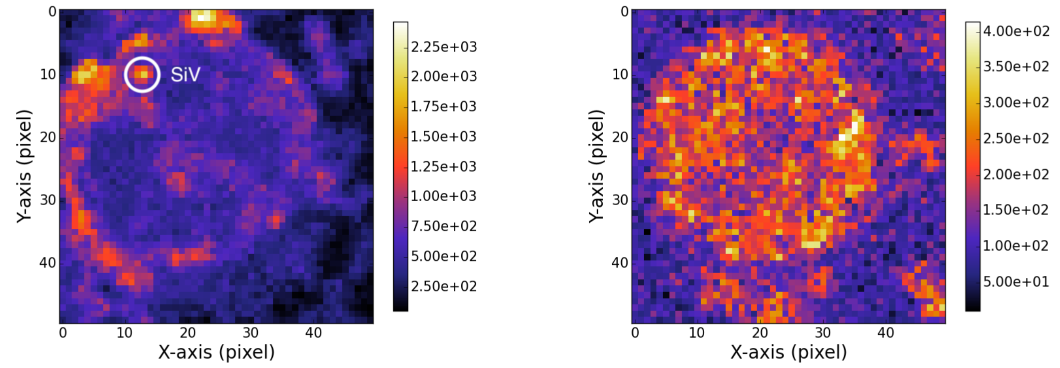

(a) **(b)**

Figure 7.11: (a) Scan of the VCSEL Bm4 with coupled nanodiamond under excitation with the laser from the confocal setup. The big visible ring is the edge of the circular aperture in the p-contact of VCSEL Bm4.The bright spot in the upper left corner corresponds to the transferred nanodiamond containing an SiV center causing a spike in the countrate. (b) Scan of the VCSEL Bm2 lacking a nanodiamond under excitation with the laser from the confocal setup. The circular aperture in the p-contact exhibits a constant countrate. Note the different color scales.

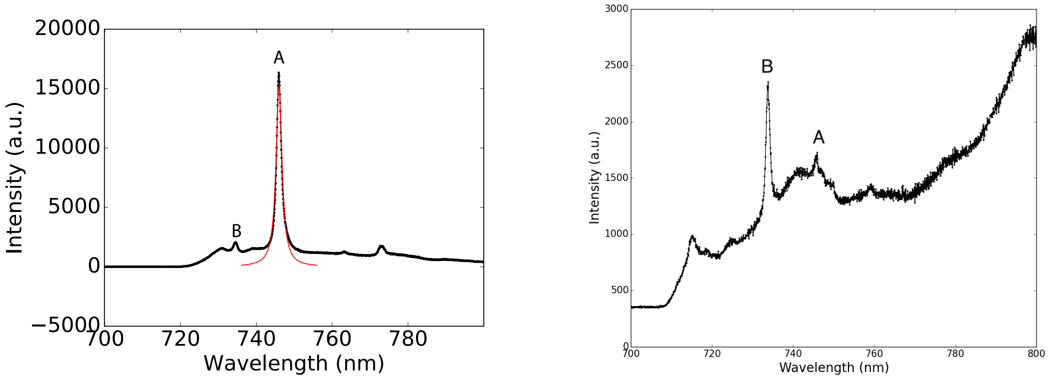

(a) **(b)**

Figure 7.12: (a) Spectrum of the preselected diamond for transfer onto VCSEL Bm4 before pick-and-place. The strong line denoted A exhibits a center wavelength of 746.0 nm and a linewidth of 1.9 nm. Line B exhibits a center wavelength of 734.5 nm and a linewidth of 3.8 nm. (b) Spectrum of the same nanodiamond after pick-and-place, excited with the same laser as before. While Line A is almost gone, line B still exists seemingly unchanged and has become the predominant line of the spectrum. We remark that due to material restrictions, different longpass filters were used for the two measurements. Measurement (a) was performed with a 720 nm longpass filter, measurement (b) with a 710 nm longpass filter.

The observed reduction of the intensity of line A is difficult to explain. One cause could be damage to the color center due to the electron radiation it was exposed to during the pick-and-place process. This is supported by previous research in this authors group recording reduced fluorescence light intensities after color centers were exposed to electron radiation [177].

With line B as remaining dominant line we then operated VCSEL Bm4 at 1.84 mA and 3.3 V, turning off the laser of the confocal setup. Thus SiV center excitation is due to the output laser of VCSEL Bm4.

For comparison, we scanned both the surface of VCSEL Bm4 including a nanodiamond as well as VCSEL Bm2 without a nanodiamond. A bandpass filter allowing light between 730 nm to 750 nm to pass was used. This filter window suppresses the VCSEL laser line at 655 nm while leaving the SiV center emission nearly unchanged. The results of the two scans are given in Figure 7.13, where the bright areas correspond to the circular VCSEL output regions. It can be seen that no difference in brightness can be established between a VCSEL with and without a nanodiamond containing a SiV center.

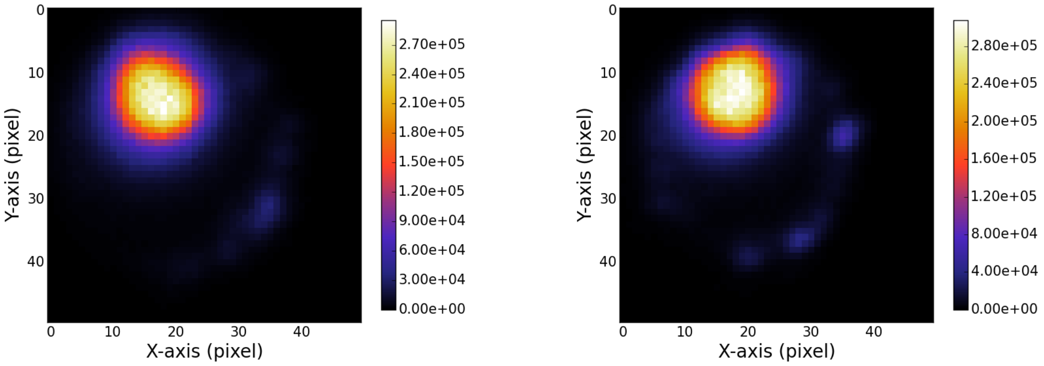

(a) **(b)**

Figure 7.13: (a) Scan of VCSEL Bm4 with nanodiamonds under laser operation in the filter window 730 nm to 750 nm. (b) Scan of the laser light stemming from VCSEL Bm2 without a coupled SiV center. The outcome of the two scans is almost identical.

For further investigations spectroscopic measurements are conducted. Since the position of the nanodiamond in VCSEL Bm4 is known, we measure the spectrum of light originating from this position. A second spectrum is obtained from VCSEL Bm2 measuring the corresponding position without a nanodiamond present. Figure 7.14 reports the results. Again no meaningful difference between the two VCSELs can be established. The lack of any distinct lines in the spectrum taken for VCSEL Bm4 which can be attributed to SiV center emission is striking.

To explain the observation, the following considerations are reasonable: The SiV

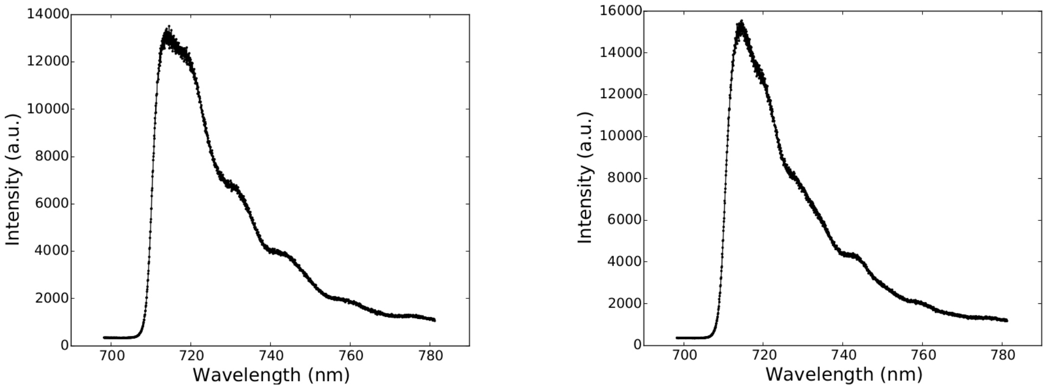

(a) **(b)**

Figure 7.14: (a) Recorded Spectrum of the SiV center in the transferred nanodiamond coupled to VCSEL Bm4 during VCSEL operation. No distinct SiV center lines are visible. (b) Recorded spectrum of VCSEL Bm2.

center is excited by the VCSEL's laser and thus emitting photons which are passing through the filter window. The same is true for photons stemming from VCSEL side band emission. Given that the emission from the side band of VCSEL Bm4 dwarfs the single photon emission of the SiV center coupled to it, the obtained results are reasonable. To confirm, the reflectivity of the DBR of VCSEL Bm4 is examined. Figure 7.15 illustrates that the DBR exhibits imperfect reflexivity in the wavelength region relevant for SiV center emission. As a result, relevant side band emissions of VCSEL Bm4 are not sufficiently suppressed to allow for SiV center emission to be detected. This in turn means that our initial attempt to realize a hybrid-integrated single photon source by coupling an SiV center to a VCSELs is thwarted by large side band emissions of the latter.

Despite a failed first attempt, a clear direction for further improvement was identified, i.e. focusing on ways to reduce VCSEL side band emission in the relevant SiV center emission regime. A promising approach to suppress the side band is to add a gold layer on top of the VCSEL acting as an additional mirror. While films of gold have a transmittance maximum at 500 nm, the transmittance minimum depends on the film's thickness [178]. Thus a gold layer could in principle be used to suppress the VCSEL side band in the SiV center emission regime. Provided such a layer can be engineered and is effective, one may expect SiV center emission to be recovered. Efforts in this direction are a required next step towards the realization of hybrid-integrated single photon sources based on SiV centers coupled to VCSELs.

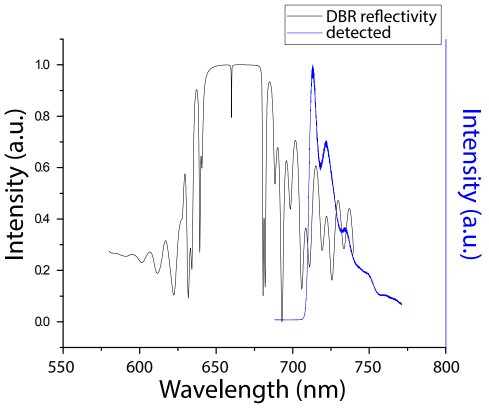

Figure 7.15: Reflectivity of the Distributed Bragg reflector (DBR) of VCSEL Bm4 [175], and a spectrum of the SiV center measured during VCSEL excitation for comparison. The reflectivity of the DBR and the VCSEL emission spectra are depicted with different scales. The shape of the measurement of the SiV center during VCSEL operation is reminiscent of the shape of the DBR reflectivity. The spectrum of the SiV center is not visible. As the emission from the SiV center is small compared to the intensity of the laser side band in the same wavelength regime, the SiV center's emission is not visible.

7.3 Coupling Nanodiamonds to Double Bowtie Antenna Structures

Plasmonic nano-antennas are very recent devices designed to efficiently convert freely propagating optical radiation into localized energy and vice versa [179–181]. Leveraging this unique property, integrating SiV centers with optical antennas creates coupled systems with a range of desirable features. These include enhanced photoluminescence emission and the ability to tailor photoluminescence spectra of the integrated emitters. The latter can be achieved by tuning the physical design parameters of the system such as antenna geometry and emitter placement.

In this chapter we report on our efforts aimed at enhancing the photoluminescence intensity of SiV centers by coupling them to plasmonic double bowtie antennas. To this end we transfer selected nanodiamonds containing SiV centers to the target antenna structure using pick-and-place methods. After successful implementation we investigate the integrated structure experimentally. In addition to that we successfully relate some of our results to theoretical predictions, and verify successful coupling of the SiV center and the antenna structure.

In the following we give a short discussion of the most important properties of optical antennas. Then we sketch the actual coupling process and report on the optical properties of the resulting integrated structure. To our knowledge, our experiments where the first attempts of coupling SiV centers in nanodiamonds to plasmonic double bowtie antennas.

7.3.1 Plasmonic Antennas

Optical nano-antennas act as converters between propagating and localized electromagnetic fields. Thus, they can be used efficiently to couple photons in and out of nano-scale objects [182]. Due to their small physical sizes, comparable or smaller than the wavelength of visible light, they are capable of focusing optical fields to sub-diffraction-limited volumes, offering the ability to manipulate electromagnetic fields at nano-scales [181, 183]. This property, dubbed sub-wavelength confinement, has successfully been exploited to enhance the excitation and emission of quantum emitters [184–187] and to modify their spectra [188]. Resulting practical applications include near-field optical microscopy [189], surface enhanced spectroscopy [190, 191] and molecular sensing [192].

A nano-antenna is a nano-structure made from materials such as noble metals like gold or silver. These metals have in common that they are very susceptible to being polarized by electro-magnetic fields. When illuminated the incident electromagnetic radiation causes electrons in the metal to behave as a plasma oscillating with respect to the atomic lattice. Thus the material is temporarily polarized until restoring forces equilibrate the charge distribution.

In other words, incident light of a given frequency induces oscillations in the free electron gas density in the surface layers of the metal. At resonance these light-induced oscillations exhibit modes of standing waves. The quasi-particles associated with these modes are known as localized surface plasmons (LSPs). For an in-depth treatment of LSPs in the context of nano-antennas we refer the reader to [113] and references therein.

Here it suffices to say, that LSPs facilitate the deciding property of optical antennas: Converting electromagnetic energy from the far-field into localized energy in the near-field. This allows, in combination with the high collection efficiencies of nano-antennas, to efficiently couple visible radiation with wavelengths of hundreds of nanometers, into small effective spatial volumes of only a few nanometers in diameter.

To create a controlled hot-spot several antenna designs are possible. In the context of this thesis we rely on double bowtie antennas available via a collaboration with N. Rahbany, group of C. Couteau, University of Technology of Troyes. Figure 7.16 illustrates the typical bowtie antenna.

This antenna design utilizes a symmetric arrangement of four identical triangle-shaped blocks, separated by a small gap. This setup allows LSP modes, associated with individual blocks, to couple with each other, resulting in the formation of an

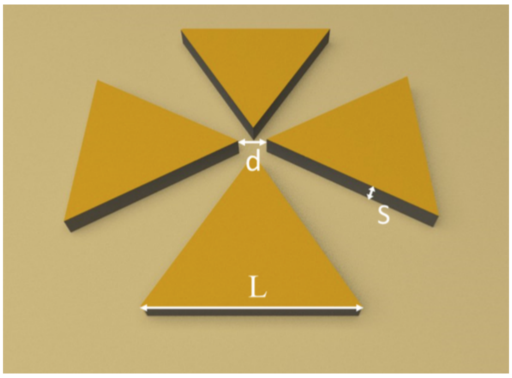

Figure 7.16: Schematic of a double bowtie antenna [113, 193].

intense hot-spot in the center area [194], see Figure 7.17. The actual electromagnetic response of a double bowtie nano-antenna depends on its physical design parameters such as gap size, material used, geometry and size. Furthermore, properties of incident light such as wavelength and polarization determine antenna operation.

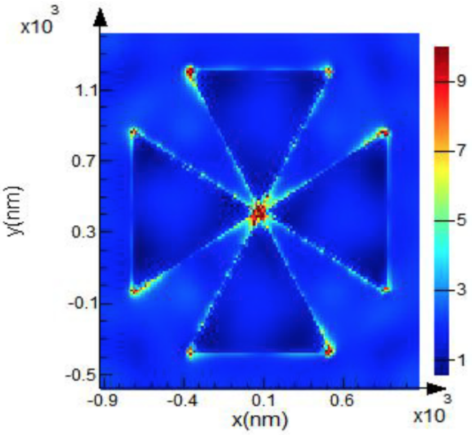

Figure 7.17: Simulation result of the electric field map of a gold double bowtie nano-antenna [113, 193]. The structure has gap of $d = 150\,\mathrm{nm}$, a side length of $L = 2\,\mu\mathrm{m}$ and a thickness of $S = 60\,\mathrm{nm}$. The center of the antenna exhibits an area of pronounced focus, the so-called hot-spot.

The enhanced electromagnetic field at the center of a metallic nano-antenna can be used to increase the spontaneous emission rate of emitters emitting at frequencies close to the resonance frequency of the antenna. This result is the known as Purcell effect [195]. The gap between the antenna arms acts as a resonant cavity providing a strong near field interaction with the emitter. This interaction modifies the density of states of the system, effectively providing additional modes for the emitter to decay into, thus amplifying its total decay rate. The amplification affects both radiative and non-radiative decay. The magnitude of the amplification for an emitter is quantified by the ratio of its enhanced decay rate to its free space decay rate, known as the Purcell factor F_p. This factor is proportional to Q/V_{eff} where Q denotes the quality of the antenna and V_{eff} the volume of the hot-spot. Thus antenna design must optimize F_p as a necessary condition for significant enhancement of fluorescence light emission.

In addition to the antenna's local field enhancement, the emitter's original quantum yield η_0 influences the overall effectiveness of the emission enhancement. From theoretical considerations [113, 196–198], the modified quantum efficiency η of the combined system consisting of emitter and antenna can be obtained as

$$\eta = \frac{\eta_0}{\frac{1-\eta_0}{F_p} + \frac{\eta_0}{\eta_{ant}}}, \tag{7.1}$$

where η_{ant} denotes the fraction of fluorescence light which is not dissipated through losses in the metal of the antenna. It is clear that an emitter with $\eta_0 \to 1$ will not profit from the Purcell effect. On the contrary, for realistic antennas with $\eta_{ant} < 1$ antenna-induced losses reduce the overall quantum yield η. Consequently poor emitters with low initial η_0 stand to profit the most from antenna-emitter coupling provided antennas are engineered well, i.e. they maximize their Purcell Factors and minimize their losses. For an in-depth review of plasmonic nano-antennas we refer the reader to [113] and references therein.

The presented considerations suggest that due to their low quantum efficiency, SiV centers are excellent candidates for coupling with antennas [42]. Thus it is promising to exploit the improved electromagnetic field at the center of a double bowtie antenna to enhance the spontaneous emission rate of SiV centers and thus improve their merit as single photon sources.

7.3.2 Plasmonic Antenna Design and Simulation

To couple SiV centers to optical antennas, we work with gold double bowtie antennas on a gold substrate. In comparison with triangular, or single bowtie antennas, double bowtie antennas offer significantly improved intensity enhancements. Antennas were provided by N. Rahbany, group of C. Couteau, University of Technology of Troyes in a joined effort to explore the possibilities of coupling SiV centers to antennas. The antennas themselves were fabricated using electron beam lithography, a technique suitable to imprint predetermined patterns onto a suitable substrate with nano-scale resolution [199]. Figure 7.18a shows a SEM image of an array of antenna structures of various designs. In Figure 7.18b a detail of an individual double bowtie antenna is shown. It can be seen that the double bowtie antenna is placed in the center of another structure, a so-called bulls-eye antenna, consisting of multiple concentric gratings. When illuminated by a laser at a proper angle, the gratings excite surface plasmon polaritons (SPPs) which are directed towards the center of the structure. If a double bowtie antenna is present in the center, SPPs can interact with the LSPs of the double bow tie, leading to an even stronger localization of electromagnetic fields in the gap of the bowtie. While this interaction certainly merits exploration in the context of enhancing SiV centers, we omit the excitation of SSPs in our first exploration of coupling of SiV centers to antennas. Thus the presence of the gratings can be ignored for our purposes. The reader interested in the details of bulls-eye antennas and their properties is referred to [113].

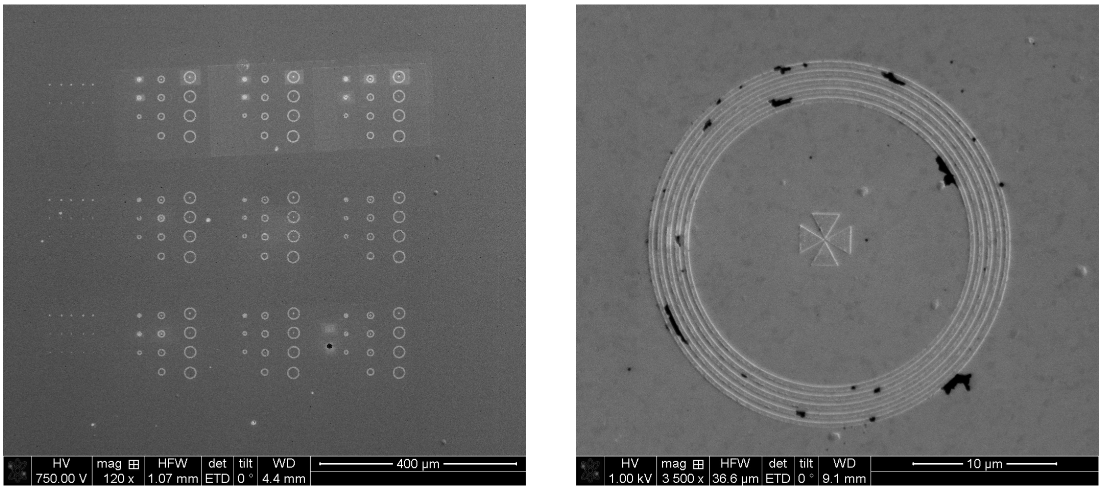

(a) **(b)**

Figure 7.18: SEM images of antenna structures. (a) Overview of a field of antenna structures exhibiting various dimensions. (b) Detail of one antenna sturcture. In the middle the double bowtie design is visible. A grating structure consisting of multiple gratings is surrounding it.

To effectively enhance the emission of an emitter by coupling it to an optical antenna, the emission wavelength must match the resonant wavelength of the antenna. In the context of SiV centers a value of 738 nm is required. Since this value can be considered constant, the design parameters of the antenna must be chosen such, that the resulting resonance matches it. An additional constraint is placed on the size of the antenna gap, since it must be big enough to accommodate nanodiamonds hosting SiV centers, the which are around 100 nm in size. However, it cannot be chosen arbitrarily big, since bigger gaps lead to larger effective volumes and thus smaller Purcell Factors.

Using finite difference time domain (FDTD) simulation deploying Lumerical Software the design parameters of gold double bowtie nano-antennas on a gold substrate were explored [113]. Although we initially attempted to simulate antennas without a nanodiamond present in the gap, it was subsequently discovered that its ab initio inclusion yielded superior results. Thus to determine usable design parameters for our purposes, an integrated system combining antenna and nanodiamond was used. To better mimic experimental conditions and associated imperfections, the nanodiamond was placed slightly off-center in the gap.

In a series of simulation it was established that a gap-size of $d = 150\,\mathrm{nm}$, a side length of $L = 2\,\mu\mathrm{m}$ and a structure thickness of $S = 60\,\mathrm{nm}$ are feasible parameters as referred to in Figure 7.16. The simulation required the index of refraction for gold which was taken from Palik [200]. The resulting geometry hosting a nanodiamond is capable of producing a suitable hot-spot when excited.

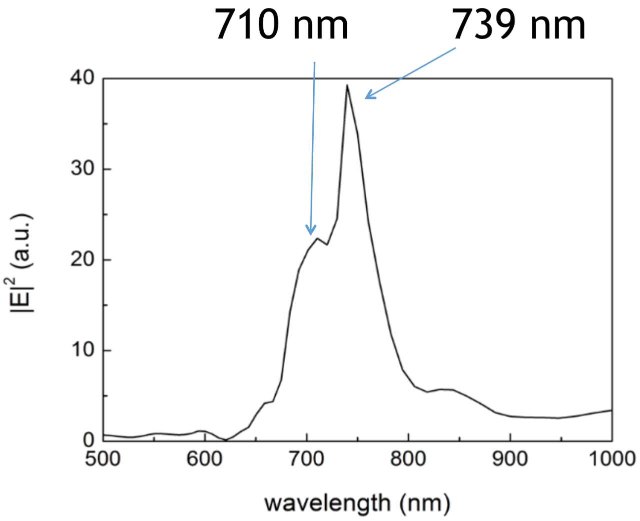

Figure 7.19: FDTD simulation of the electric field intensity of a double bowtie nano-antenna as as a function of the wavelength of incident light. Two peaks are identified. The major peak corresponds exceptionally well with SiV center emission at 738 nm. The minor peak is attributed to the presence of a nanodiamond [193].

Finally, to pin-point the resonant wavelength of the antenna hosting a nanodiamond, the electric field intensity is simulated as a function of the wavelength of the incident light. The resulting spectrum is shown in Figure 7.19. Two resonant peaks are found. The intense major peak at 739 nm coincides exceptionally well with the SiV center emission wavelength 738 nm indicating successful antenna design. In addition to the major peak, an additional minor mode at a lower wavelength of 710 nm is found [113]. We remark that if the nanodiamond in the gap of the antenna is removed from the simulations, the minor feature vanishes. Thus the additional peak is well-attributed to the presence of the nanodiamond.

In summary, the combined simulation results suggest, that the engineered system of nano-antenna and nanodiamond is well suited to effectively enhance the emission from an SiV center hosted in the nanodiamond. Next we report on the experimental realization of this preposition.

7.3.3 Silicon-Vacancy Center in a Plasmonic Double Bowtie Antenna

In the following we report on our attempts to couple SiV centers to gold double bowtie nano-antennas in order to study the properties of the resulting integrated system. Ideally, a suitable nanodiamond containing exactly one SiV center is placed in the center of the antenna. The term suitable is used to summarize both desirable spectroscopic properties such as narrow-bandwidth single-photon emission as well as technical requirements such as nanodiamond size and degree of isolation on the surface. Naturally, the odds of identifying and addressing a nanodiamond fulfilling all these criteria simultaneously are small. As a result identifying a perfect candidate for coupling is prohibitively time-consuming. Figure 7.20 shows a $0.5\,\mathrm{mm} \times 0.5\,\mathrm{mm}$ area of the surface of one of the samples which was used to identify suitable nanodiamonds. The black dots are nanodiamonds. It can be seen, that the concentration of the nanodiamonds and therefore the isolation of nanodiamonds varies. The black frames correspond to areas of which confocal scans were recorded to identify nanodiamonds emitting fluorescence light. The red dots indicate nanodiamonds which are isolated and large enough for the pick-and-place process and of which at least a photoluminescence spectrum and a saturation measurement and in some cases a $g^{(2)}$ measurement were recorded. Despite the significant area that was covered in our search, only two of the investigated candidate nanodiamonds revealed a favorable spectrum, emission saturation and at least a small dip in the $g^{(2)}$ function indicating a small amount of SiV centers.

To mitigate this difficulty we decided to relax the condition of exactly one SiV center per nanodiamond and initiate our exploratory work with nanodiamonds containing several, potentially many active SiV centers. Relying on $g^{(2)}$ measurements we identify two interesting classes of nanodiamonds. The first class consists of nanodiamonds containing large ensembles of SiV centers acting as coherent emitters. The fluorescence light received from large ensemble of emitters is mainly coherent, leading to a flat response in the $g^{(2)}(0)$ function. The second class of nanodiamonds we investigate features nanodiamonds hosting multiple SiV centers. As a result relevant $g^{(2)}(0)$ measurements report weak but discernible anti-bunching dips. Both classes have in common that relevant nanodiamond specimen are significantly easier to obtain than nanodiamonds containing single SiV centers. Thus nanodiamonds containing ensembles of SiV centers as well as nanodiamonds containing few SiV centers are both valid starting points for our work. It is likely that the experience gained during our preliminary explorations will be valuable once nanodiamonds containing single SiV centers become available.

Next we report on coupling nanodiamonds containing SiV centers to antennas. We illustrate the coupling process and its challenges and discuss relevant results regarding the coupling of nanodiamonds of the classes described above. We close the chapter with a short discussion and suggestions for further research.

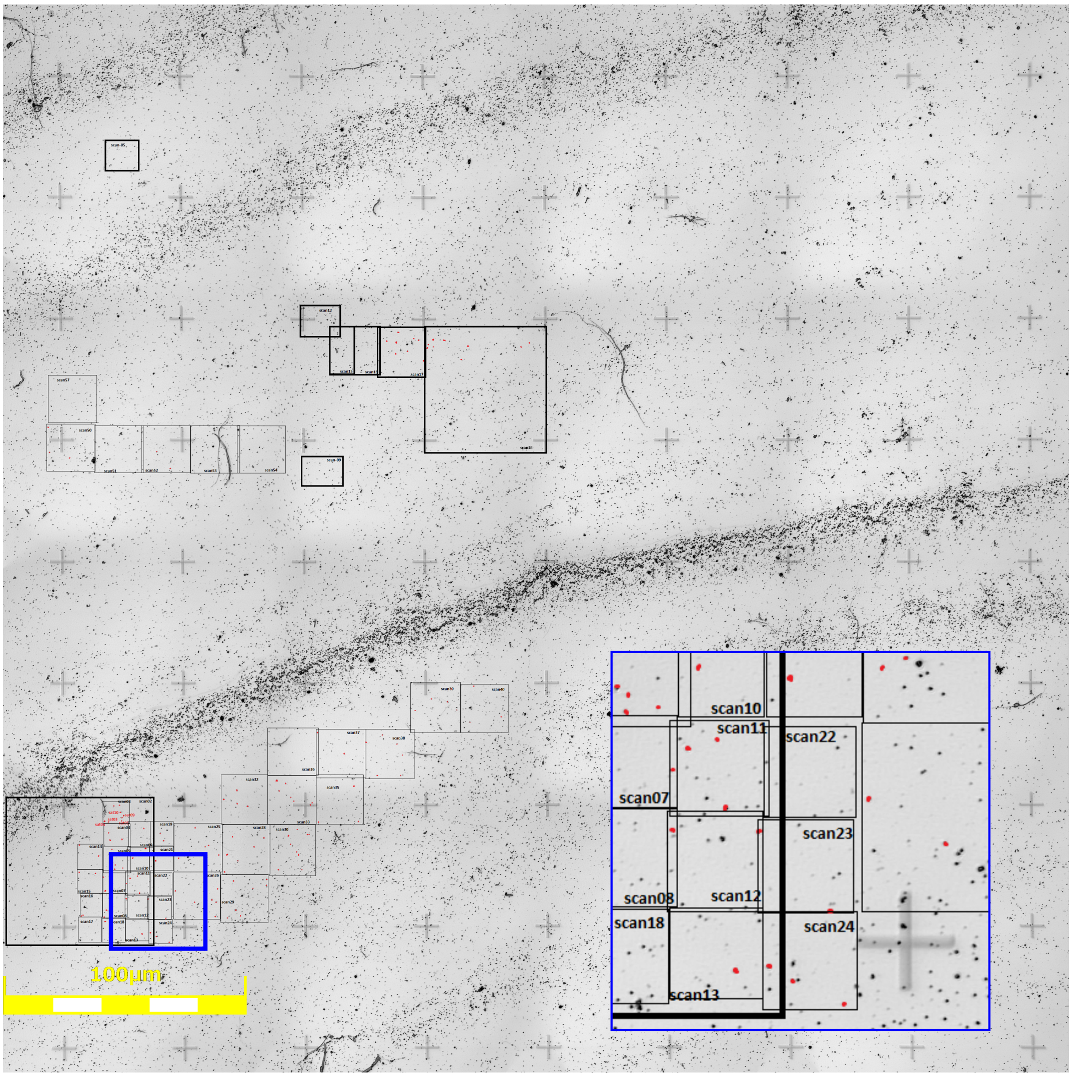

Figure 7.20: Laser scanning microscope scan of a 0.5 mm × 0.5 mm area of the investigated samples in search for suitable nanodiamonds. Black frames correspond to areas of which confocal scans were recorded to identify nanodiamonds emitting fluorescence light. Red colored dots indicate nanodiamonds which are isolated enough for the pick-and-place process and of which at least a photoluminescence spectrum and a saturation measurement and in some cases a $g^{(2)}$ measurement were recorded. The inset shows a magnification of the area framed in blue for better visibility of the red colored dots.

Nanodiamonds Containing Ensembles of SiV centers Coupled to Antennas

The nanodiamonds used for the approach of coupling ensembles of SiV centers to an antenna were wet-milled from a CVD diamond film.[1] The solution of nanodiamonds exhibiting a median size of 100 nm was spin-coated on an iridium substrate treated with Piranha etch (sample of type insitu100). To ensure that a preselected nanodiamond exhibiting preferred optical properties can reliably be located, the iridium substrate was engraved with reference cross markers produced by a focused ion beam after the spin-coating process. After spin-coating, the sample was placed in an oven for 3 h at 450 °C to oxidize the surface and remove any residual graphite and amorphous carbon. See Chapter 4 for more information.

To determine the position of nanodiamonds on the original substrate, first a scan with a commercial laser scanning microscope (LSM) was performed as described in Section 7.1.2. Figure 7.21a shows a part of an obtained LSM image. After transferring the sample into the confocal setup, confocal fluorescence light scans of the corresponding areas are performed to identify nanodiamonds containing active emitters. The scanned area is shown in Figure 7.21b. It corresponds to the area shaded blue in Figure 7.21a. Thus, upon close inspection some of the bright spots appearing in the fluorescence light scan can be associated with selected nanodiamonds in Figure 7.21a by eye. The correspondence between the SEM and LSM images in conjunction with the cross-markers on the substrates allows to precisely locate preselected nanodiamonds containing suitable emitters in the SEM.

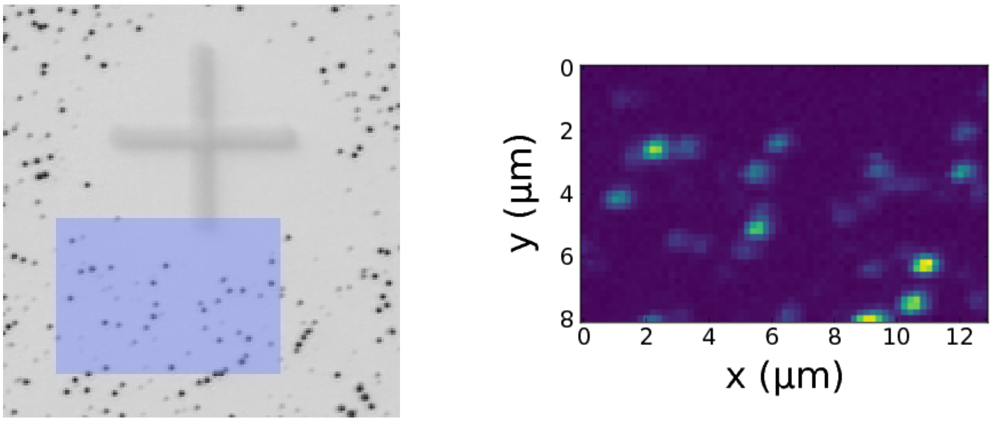

(a) **(b)**

Figure 7.21: (a) Picture recorded with a commercial high resolution laser scanning microscope. Black dots are individual nanodiamonds. The cross-marker serves as an orientation aid. The area shaded in blue represents the photoluminescence scan in image (b). (b) Photoluminescence scan of an 8 µm × 13 µm area.

---

[1] Wet-milling performed by A. Muzha, group of A. Krueger, Julius-Maximilians Universität Würzburg, diamond film grown by group of O. Williams, School of Engineering, Cardiff University.

The most promising candidate nanodiamonds are characterized by fluorescence light spectra with very narrow zero-phonon-lines and minimal phonon side band features. Figure 7.22a shows the spectrum stemming from one such preselected nanodiamond. The ZPL feature exhibits a center wavelength of $(738.6 \pm 0.1)\,\mathrm{nm}$ and a linewidth of $(5.0 \pm 0.1)\,\mathrm{nm}$, corresponding well with the ZPL of unstrained SiV centers. Photon autocorrelation measurements revealed that the nanodiamond contains an ensemble of SiV centers collectively generating coherent fluorescence light, see Figure 7.22b.

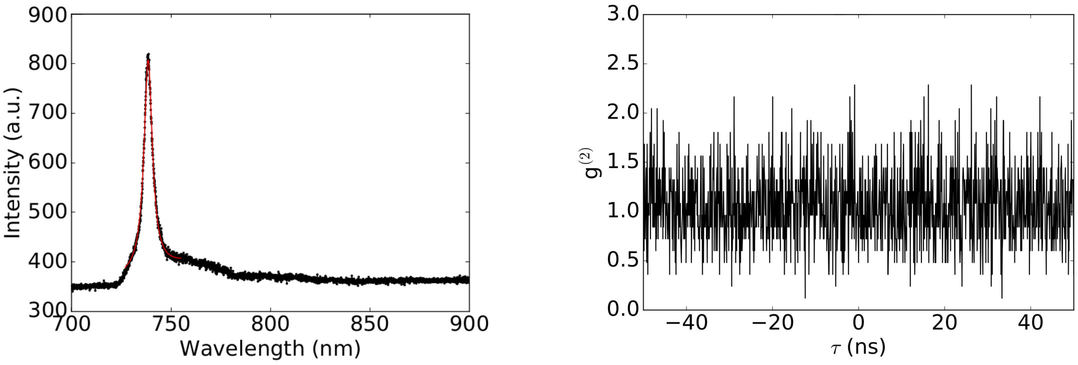

(a) **(b)**

Figure 7.22: (a) PL spectrum of the emitter in the preselected nanodiamond at room temperature. Black: experimental results; red: fit to experimental data, which yields a ZPL center wavelength of $(738.6 \pm 0.1)\,\mathrm{nm}$ and a linewidth of $(5.0 \pm 0.1)\,\mathrm{nm}$. (b) Intensity autocorrelation function recorded for the ensemble of emitters hosted by the nanodiamond. The flat response indicates the coherent nature of the fluorescence light.

After a proper candidate for coupling with an antenna has been identified, it needs to be relocated from its original substrate to the antenna. To this end the pick-and-place process introduced in Section 7.2.1 is used. A complete illustration of the steps involved is given in Figure 7.23.

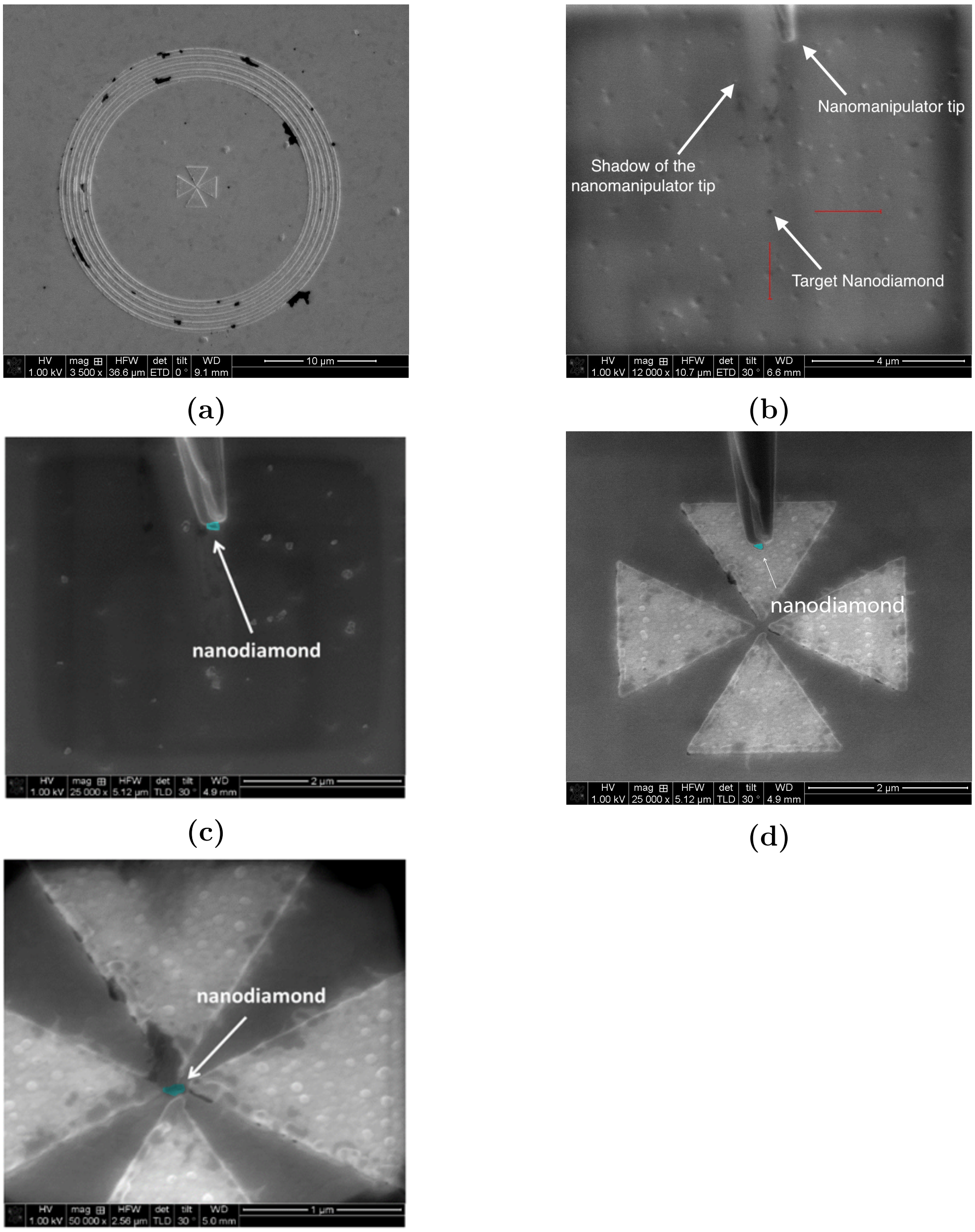

(a) **(b)** **(c)** **(d)** **(e)**

Figure 7.23: Transferring a select nanodiamond from its original substrate to the center of a nano-antenna using pick-and-place methods. For better visibility, the transferred nanodiamonds is colored blue. (a) Target gold double bowtie antenna on gold substrate. (b) Nanomanipulator tip approaching a predetermined target nanodiamond. (c) Payload nanodiamond sticks to the tip for transport. (d) Nanomanipulator tip in approach of the antenna. (e) Payload nanodiamond was placed in the gap of the double bowtie antenna.

The gold surface of the plasmonic antenna exhibited strong adhesion forces between the antenna surface and the nanodiamond. Once the nanodiamond touched the gold, it could not be picked up again with the tungsten tip. The nanodiamond first touched the antenna structure a few nanometers away from the gap and immediately sticked to the surface, on top of one of the triangles. Therefore, the nanodiamond had to be pushed into the gap with the nanomanipulator tip. This process caused some damage to the antenna structure. The damage is visible as black area at the tip of the top triangle in Figure 7.23e. Luckily, FDTD simulations of damaged antennas reveal that this modification of the antenna hardly influences the antenna resonance.

After successful placement, the antenna sample is installed in the confocal setup. The antenna itself was located during a scan of the sample surface under white light illumination. A scan of the antenna is performed in the confocal setup using a 660 nm continuous wave laser. It serves to locate the middle of the antenna structure and therefore the nanodiamond which had been placed there. An outline of the rings is visible in an overview scan of the antenna structure shown in Figure 7.24a. Zooming in to the exact center of the rings, some of the edges of the bowtie antenna are vaguely visible in Figure 7.24b.

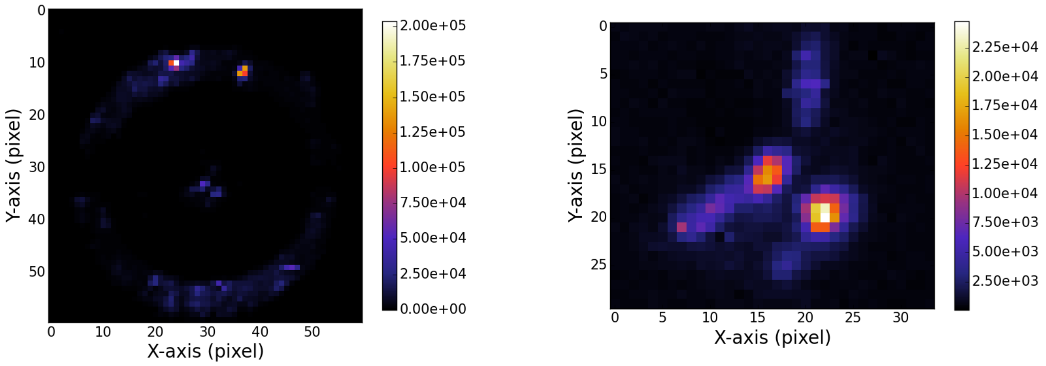

(a) (b)

Figure 7.24: (a) Confocal scan of the double bowtie antenna where a nanodiamond containing multiple SiV centers had been placed. The rings are visible. (b) Detail scan of the triangles of the same antenna structure, which make up the double bowtie antenna. While the separate triangle cannot be seen, some edges and two bright spots are visible. To identify the place of the nanodiamond we compare the middle point of the rings in (a), the point of intersection of the edges and the bright spot and conclude that the upper bright spot in (b) is the location of the nanodiamond.

These images serve to locate the nanodiamond with sufficient precision to measure PL spectra. The PL spectrum of the ensemble of SiV centers in the antenna is shown in Figure 7.25a. It can be seen that at 739 nm a major peak is present, coinciding with the major antenna resonance peak.

We verified successful coupling of the ensemble of SiV centers to the antenna by combining experimental and numerical results. In particular, we convolve the experimental PL spectrum of the nanodiamond measured before placing it in the nano-antenna, see Figure 7.22a, with the resonance spectrum of the nano-antenna obtained by means of simulations given in Figure 7.25a. The result of the convolution is the spectrum given in Figure 7.25b. The agreement with the measured spectrum in Figure 7.25a is almost perfect, indicating successful coupling of emitters and antenna.

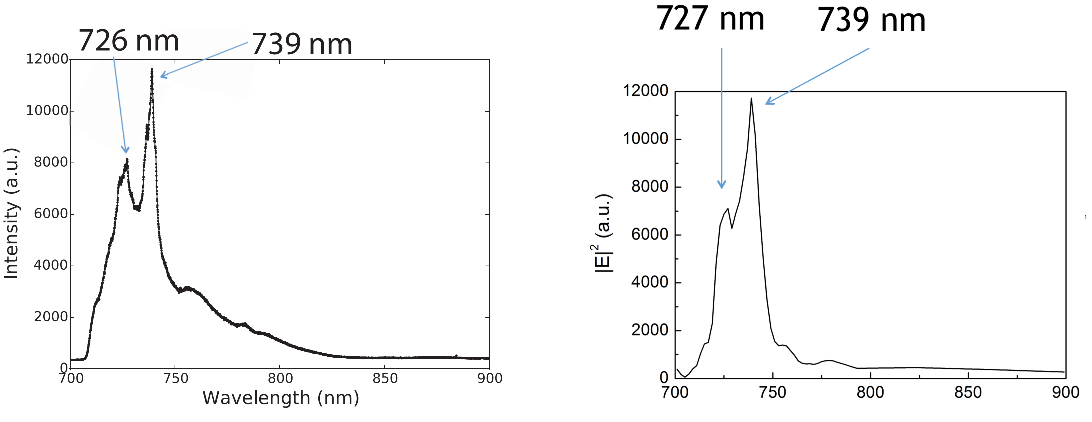

(a)

(b)

Figure 7.25: (a) Measured PL spectrum of the emitter after placing the nanodiamond into the nano-antenna, (b) Convolution of the spectrum of the measured PL spectrum of the emitter before pick-and-place, see Figure 7.22a, and the simulated resonance spectrum of the nano-antenna, see Figure 7.25a.

We remark that, any damage sustained through electron radiation during the pick-and-place process is likely not sufficient to invalidate the nanodiamond. This is expected as a large ensemble of SiV centers can easily lose several emitters without any noticeable difference in the optical properties. Needless to say, the exact opposite is true for nanodiamonds with very few hosted SiV centers making them risky to work with. Finally, keeping experimental conditions unchanged, we measure a spectrum of an identical antenna without a nanodiamond present in order to rule out surprising artifacts induced by the antenna itself. The resulting spectrum is given in Figure 7.26.

At this point one must resist the temptation of comparing the values of the intensity maxima of the spectra in Figure 7.22a and Figure 7.25a in order to determine the enhancement the ensemble of emitters experiences. These values inherently do not allow a meaningful comparison.

A meaningful comparison can in principle be achieved via intensity saturation mea-

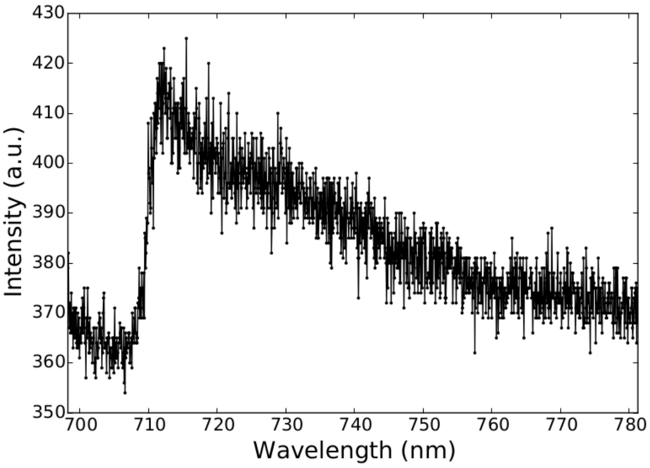

Figure 7.26: Spectrum of a gold double bowtie nano-antenna without a nanodiamond present, excited with a 660 nm continuous wave laser.

surements. By measuring the saturation intensities before and after insertion into the antenna and accounting for effects related to the polarization of emitters, the magnitude of the Purcell enhancement can be determined. Unfortunately, these methods are reserved for single emitters and do not apply for ensembles of SiV centers. Thus at this point we have no method to determine the Purcell enhancement ensembles of SiV centers experience.

In summary, in this section we showed that coupling of nanodiamonds containing ensembles of SiV centers with gold double bowtie antennas is feasible using a pick-and-place approach. Furthermore we verified that the coupling is indeed present after the nanodiamond was placed in the gap of the antenna.

Nanodiamonds Containing Few SiV Centers Coupled to Antennas

After a first successful validation of inserting nanodiamonds hosting large ensembles of SiV centers into a gold double bowtie antenna, we attempt to select nanodiamonds containing a comparatively small number of SiV centers. Suitable nanodiamonds show an anti-bunching dip in the $g^{(2)}$ function in addition to count-rate saturation. This can be regarded an intermediate step towards using nanodiamonds containing single SiV centers. We stress that in comparison to nanodiamonds hosting large ensembles of emitters, nanodiamonds containing only a few emitters are already difficult to identify. Naturally, technical requirements applying to candidate nanodiamonds such as sufficiently isolation for picking it up in the pick-and-place process and a size not larger than that of the antenna gap still need to be observed.

The starting material for the nanodiamonds used here was an electronic grade diamond film produced by the company rho-BeSt coating (now renamed to CarbonCompetence). The film was then milled in a bead-assisted sonic disintegration process[2] to nanodiamonds of a median size of approximately 100 nm. The nanodiamonds were drop-cast at 60 °C onto an iridium substrate containing cross markers. Prior to drop-casting the substrate was cleaned with Piranha etch.

As described in the previous section, a commercial laser scanning microscope (LSM) is used to identify nanodiamonds on the substrate. Using the cross markers to address their exact positions, a corresponding fluorescence light scan allow us to single out nanodiamonds with bright emission. We further test the suitability of potential candidates as follows. First, a saturation curve is recorded to establish whether the SiV centers in a nanodiamond saturate. Since saturation is a necessary albeit not sufficient condition for single-photon emission, only nanodiamonds that saturate are capable of showing an anti-bunching dip in the $g^{(2)}$ function. For nanodiamonds containing SiV centers showing saturation we then check the spectrum to assert that the emitters are indeed SiV centers. After this last check $g^{(2)}$ function measurements are established. Note that, measuring the $g^{(2)}$ function potentially requires hour-long measurements, while determining saturation requires merely seconds. Thus, in search of candidate nanodiamonds we may use the saturation properties as a quick check whether a candidate is feasible to follow up with a lengthy $g^{(2)}$ function measurement.

After a significant search, involving a sizable number of discarded candidates, a nanodiamond with a discernible anti-bunching dip was found. Figure 7.27a shows its $g^{(2)}$ function while Figure 7.27b reports its saturation curve. While the dip in the $g^{(2)}$ function is quite weak, it is present and a fitting it was possible. This indicates that the nanodiamond neither contains a single SiV center nor does it host enough SiV centers to emit coherent light. Thus we conclude that a limited number of SiV centers must be present. While it is not possible to quantify the number of emitters directly, the candidate sufficiently differs from nanodiamonds hosting large ensembles of SiV centers. Thus it is viable to take it to the stage of coupling. A photoluminescence spectrum of the emitter is shown in Figure 7.28b.

In order to relocate the identified nanodiamond to the center of a gold double bowtie antenna we repeat the pick-and-place procedure described in the previous section, see Figure 7.23. We remark at this point that since the nanodiamond in question contains fewer SiV centers as compared to the nanodiamonds hosting large ensembles of SiV centers, it is expected to be less resilient to adverse effects such as the electron radiation present during the pick-and-place process.

After a successful relocation, the sample containing the antenna is mounted in the confocal setup to investigate the properties of the combined system consisting of antenna and SiV centers. Figure 7.28a gives the spectrum of the candidate nanodiamond after being relocated to the center of a gold double bowtie antenna. Interestingly we find a multitude of individual peaks. In addition we find that the

---

[2] A. Krueger, Julius-Maximilians Universität Würzburg.

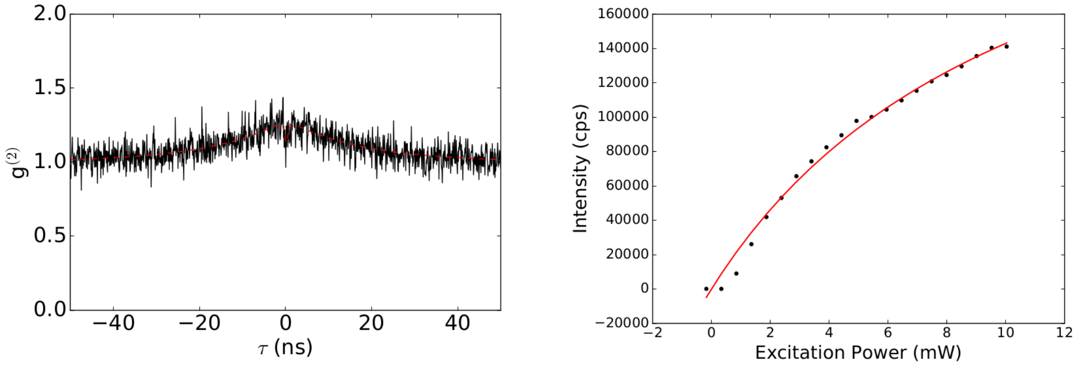

(a) **(b)**

Figure 7.27: (a) The $g^{(2)}$ function of the preselected nanodiamond believed to host a limited number of SiV centers. A dip at $g^{(2)}(0)$ is present, however its decrease is not sufficient for a single SiV center. This indicates that a limited number of SiV centers is present since the absence of a dip can only be measured under coherent emission, i.e. for larger ensembles of SiV centers. The dashed red line gives a fit to the data. (b) Saturation curve of the same emitter yielding a saturation power of (11 ± 1) mW and a saturation countrate of (300 ± 20) kcps. Data points are black, fitted curve red.

sideband appears more pronounced in relation to the intensity of the major feature after the nanodiamond has been relocated to the antenna.

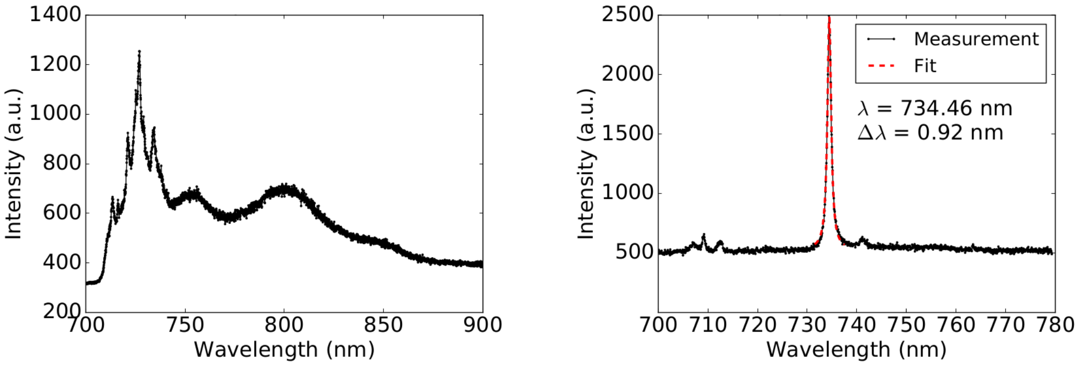

(a) **(b)**

Figure 7.28: (a) Spectrum of the preselected nanodiamond hosting few SiV centers after being relocated to the center of a double bowtie antenna. (b) Spectrum of the same nanodiamond before relocation.

To exclude the possibility that the multitude of obtained peaks are artifacts due to misalignment of the experimental setup, we rechecked the alignment which proved to be precise.

To reverify the obtained spectrum, we repeated the measurement. Unfortunately, we obtained an entirely different result, showing only a broad background seen in Figure 7.29a. After checking in the confocal scan that the measurement was performed at the correct position, we had to conclude that all of the SiV centers hosted by the nanodiamond permanently bleached after recording the spectrum seen in Figure 7.28a. It is likely that continued application of energy from the laser triggered this effect as earlier independent measurements established that SiV centers exhibit an increased likelihood of bleaching after being exposed to electron radiation [177]. Thus we conclude that the exposure to electron radiation during the pick-and-place process left the SiV centers in an unstable state susceptible to bleaching.

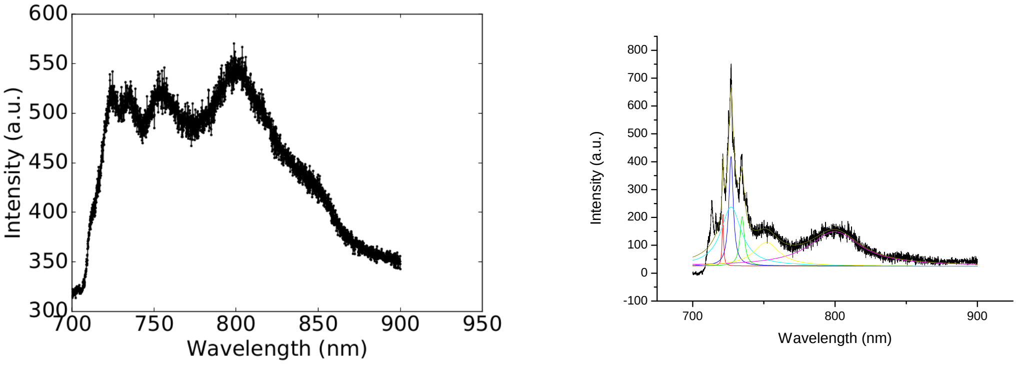

(a)

(b)

Figure 7.29: (a) Spectrum of the nanodiamond hosting few SiV centers coupled to the double bowtie antenna after the emitter bleached. (b) Background corrected spectrum of the transferred nanodiamond in the double bowtie antenna. Peaks are fitted, results of the fits are the colored lines. For background correction, the spectrum in (a) was used.

Even though the nanodiamond was invalidated for further measurements, the spectrum that was obtained remains to be discussed further. To better understand the obtained observations, we turn to FDTD calculations of the nanodiamond coupled to a gold plasmonic double bowtie antenna as described in the beginning of this chapter. The simulation result constitutes a prediction of what the spectrum in Figure 7.28a should look like. Figure 7.30 illustrates the simulation prediction and demonstrates that we have no reason to expect to see the peaks between 700 nm to 750 nm observed experimentally. Hence we must conclude that the spectrum of the nanodiamond was modified during the pick-and-place process. While it is not possible to pinpoint exactly which circumstance caused the modification, several effects could influence the observed spectra.

First, the electron radiation itself. While it lacks the energy to modify the lattice itself, it can influence the electrons present and in particular may modify the charge state of SiV centers. As was mentioned before, electron radiation was linked to increased likelihood of photo-bleaching.

Next, during the pick-and-place process it is possible that the nanodiamond collects additional contaminating matter on its surface. Contaminations may be fluorescing themselves, thus modifying the spectrum.

Yet another property of SiV centers which should not be neglected is their dipole orientation interacting with the antenna. FDTD simulations of a damaged antenna were performed with a focus on different dipole orientations. While these calculations revealed a negligible effect of the antenna damage, the outcomes vary drastically for different dipole orientations, see Figure 7.30. Figure 7.29b exhibits broad features around 750 nm and 800 nm in our experiment with few emitters, which coincide with the peaks in the simulation with dipole orientations xy and y. While the broad features could possibly be attributed to the influence of the dipole orientation of the emitter in the antenna, the major narrow peaks in Figure 7.29b remain to be explained. Future experiments aiming to investigate the effect of coupling nanodiamonds containing a single SiV center to antennas should include polarization measurements to experimentally quantify the impact of the emitter orientation.

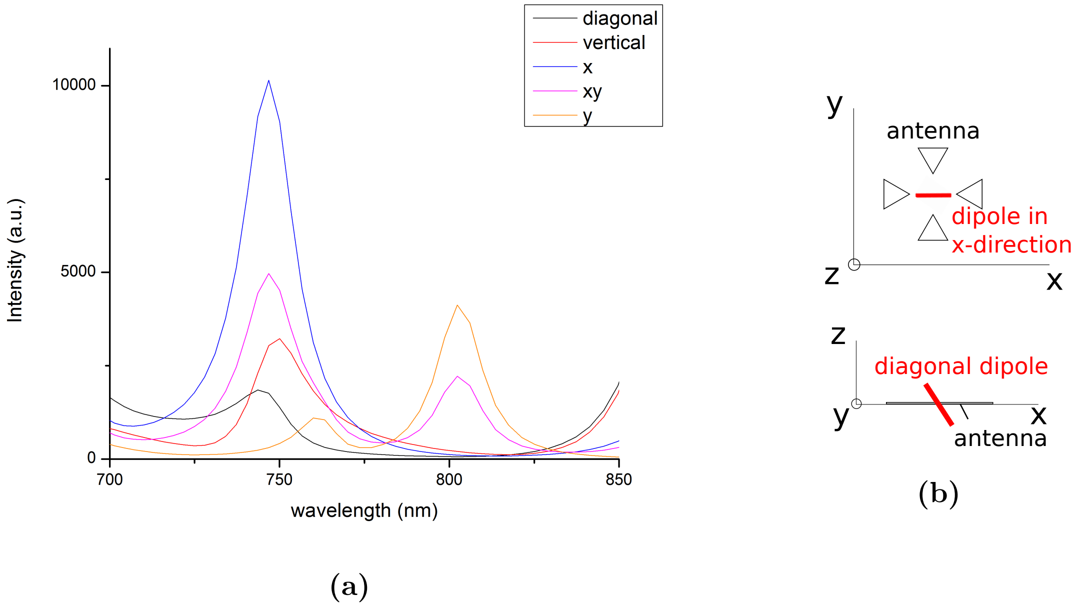

(a)

(b)

Figure 7.30: (a) FDTD simulations of a dipole in a damaged antenna with different dipole orientations. Diagonal and vertical refer to out-of-plane dipole orientations, x, xy, and y are in the plane of the antenna structure. (b) Sketch visualizing the dipole orientations used in (a).

As it stands, the most likely explanation of the recorded spectrum consists of a combination of the discussed effects.

Summary and Conclusions

In this thesis we explore selected properties of the silicon color center (SiV center) hosted in nano-sized diamond grains (nanodiamonds). Studying the silicon-vacancy center in diamond is motivated by the fact that this particular color center has surfaced as a promising candidate for realizing reliable on-demand single photon sources. Such non-classical light sources are key for the proper calibration of detectors and other instruments designed to operate reliably in the single-photon counting regime. This in turn is expected to drive a shift towards quantum based radiometric SI units, such as the quantum candela, which in the long run is expected to foster improvements in our ability to work with individual photons in a wide range of practical applications.

The SiV center has the potential to add considerable momentum to this cause. It is a stable narrow linewidth emitter, emitting single photons with high intensity. Conveniently, SiV centers operate at room temperature under ambient pressure and hence do not require extremely sophisticated experimental setups. When incorporated in nano-sized diamond, individual SiV centers can be identified and preselected according to their spectroscopic properties and transfered using pick-and-place techniques. Their narrow linewidth is a crucial advantage in the realization of photon number based measurement applications, since the efficiencies of suggested photodetectors are wavelength dependent [41].

Our work can roughly be subdivided into two larger explorations. The first, reported in Chapter 6, revolves around charting the luminescence properties of a large set of emitters, allowing us to establish distributions of selected SiV center properties. To our knowledge, our efforts result in the largest coherent examination of SiV centers in nanodiamonds to date. In contrast to that the second exploration focuses on individual nanodiamonds hosting SiV centers and our attempts to relocate them to different nano-structures in order to achieve a coupling between SiV centers and the host structure. Chapter 7 details our efforts to realize a controllable integrated single photon source by placing a nanodiamond containing SiV centers on top of a vertical-cavity surface emitting laser (VCSEL). Furthermore, we combine nanodiamonds with plasmonic nanoantennas in order to enhance the emission properties of the contained SiV centers. A detailed summary of the results obtained in both explorations follows below.

To enable our research, we synthesize nanodiamonds containing SiV centers using a variety of different techniques. Chemical vapor deposition (CVD) and high-pressure, high-temperature (HPHT) synthesis is used to fabricate nanodiamonds. In addition to the mentioned well established methods, wet-milling allows a high quantity of nanodiamonds to be produced in one process and therefore enables us to produce a sizable set of nanodiamond samples. For this technique macroscopic diamond films are broken down to diamond grains of various sizes by vibrating steel beads in a vibrational mill. We improve the quality of nanodiamond samples via annealing and oxidation. In particular Raman measurements show that contaminations due to non-diamond carbon can be significantly reduced.

To investigate the obtained nanodiamonds, i.e. to study the optical properties of embedded SiV centers we rely on optical excitation. In particular, confocal microscopy is used to collect emitted fluorescence light. Samples are scanned in search for fluorescent emitters using avalanche photo diodes. Fluorescent light is further investigated with an attached spectrometer and single emitters are identified by means of a Hanbury-Brown and Twiss setup.

With regards to the investigation of large sets of emitters we find a previously unknown strongly inhomogeneous distribution of SiV center spectra in nanodiamonds. The distribution in particular suggests a partitioning of emitters according to the wavelength and linewidth of their zero-phonon-lines (ZPL) into two groups, group V and group H.

Group H consists of ZPLs exhibiting a narrow linewidth from below 1 nm up to 4 nm and a broad distribution of center wavelengths between 710 nm and 840 nm. Compared to that, group V is comprised of ZPLs with a broad linewidth between just below 5 nm and 17 nm and center wavelengths ranging from 730 nm to 742 nm. This data is consistent with previously measured SiV spectra [48, 143]. For comparison, an SiV center in unstrained bulk diamond exhibits a linewidth of 4 nm to 5 nm at a center wavelength of 737.2 nm [107, 142]. Based on ab initio density functional theory calculations we show that both the observed blue-shifts and red-shifts of the ZPLs of group V (as compared to an ideal, unstrained SiV center) are consistently explained by strain in the diamond lattice. Further, we suggest, that group H might be comprised of modified SiV centers, the structure of which is currently unclear.

The broad distribution of emission wavelengths found here covers all earlier results on spectroscopy of SiV centers but considerably extends the range of known emission wavelengths. It further suggests that some single photon emitters in the range of 715 nm to 835 nm, previously identified as Cr-, Ni- or Ni/Si-related, could in reality be strained or perturbed SiV centers. Whereas single photon emission could be demonstrated for silicon-vacancy center of both clusters, we unveil further spectroscopic differences which set the two groups apart. For the phonon side band spectra in group V we find one prominent peak at a shift of 42 meV, which corresponds to a well-known feature assigned to non-localized lattice vibrations [99, 162]. In group H we see accumulations of peaks, at around 43 meV, 64 meV, 150 meV and 175 meV, which are consistent with sideband peaks reported in [59, 99, 161].

Investigating the time trace of SiV center photoluminescence, we find that some SiV centers exhibit fluorescence intermittence, also known as blinking, with on-times ranging from several microseconds up to 41 s. All but one single emitters in group H exhibit blinking, where only one of the emitters in group V exhibits blinking. Furthermore, we see an exponential distribution for bright-time intervals and a establish a log-normal distribution for dark-time intervals, consistent with research on single molecules [169].

After reporting the results of charting the properties of large sets of nanodiamonds and their contained SiV centers, we move on to working with individual nanodiamonds. The ability to examine SiV centers individually opens up the possibility to preselect emitters according to desired spectroscopic parameters, such as narrow linewidths, high count-rates and single photon emission.

Once such suitable candidates are identified, they can be transferred to different substrates with precision using pick-and-place methods. Although these methods are difficult to execute, SiV centers may be relocated and coupled to photonic structures where their extraordinary properties can be exploited in conjunction with photonic structures. In the scope of this thesis, nanodiamonds including suitable SiV centers were identified and coupled to two different kinds of structures: Vertical-Cavity Surface Emitting Lasers (VCSELs) and plasmonic nanoantennas.

Red AlGaInP-based oxide-confined VCSELs are perfect candidates for the excitation of SiV centers in a hybrid integrated single photon source. Their physical size and the fact, that their output beam is perpendicular to the substrate implies that candidate nanodiamonds containing SiV centers can simply be placed on top of the light-emitting region of the structure. Then, the VCSELs output laser can be used to optically excite SiV centers, steering emission of the SiV center indirectly via the electrical operation of the VCSEL. Through the use of suitable optical filters allowing only SiV center fluorescence light to emerge, a controlled single photon source can be realized in principle.

Although our initial attempt to realize a hybrid-integrated single photon source by coupling SiV centers to a VCSEL is thwarted by large side band emissions of the latter, a clear direction for further improvements was identified. In particular it seems promising to explore the idea of putting an additional gold layer on-top of the VCSEL. If well-engineered it could be used as a mirror to suppress the VCSEL side band in the relevant SiV center emission regime. Proper sideband suppression would open the door for an electrically driven, small scale single photon source. This system is interesting in the context of metrological applications, as it constitutes a promising building block for a portable device ready to calibrate single photon detectors. Furthermore, recently suggested methods for the absolute calibration of optical power levels could likely take advantage of SiV centers coupled to VCSELs [41].

With the experience gained by coupling individual nanodiamonds and their emitters to VCSELs, we proceed to explore the possibilities of combining SiV centers with plasmonic nanoantennas. Nanoantennas are very recent nano-scale devices designed to efficiently convert freely propagating optical radiation into localized energy and vice versa. Here we use gold double bowtie antennas on a gold substrate. This design allows the creation of a focused electromagnetic field in the gap in the center of the antenna, a so-called hot-spot. Placing emitters in such a hot-spot is known to increase their spontaneous emission rate provided their emission frequency is close to the resonance frequency of the antenna. This is known as Purcell effect and is used to improve the emission intensity of single emitters [195]. Recently this effect has been successfully used to improve the emission intensity of SiV centers by coupling them to optical cavities, nano-particles or solid-immersion lenses [201–204].

In our work we aim at placing a suitable nanodiamond hosting an SiV center in the hot-spot of a double bowtie antenna in order to enhance the emission of the hosted SiV centers. The term suitable is used to summarize both desirable spectroscopic properties such as narrow-bandwidth saturated single-photon emission as well as technical requirements such as nanodiamond size and sufficient degree of isolation on the surface to enable pick-and-place. Feasible physical design parameters for the antenna meeting these requirements were determined using finite difference time domain (FDTD) simulations. Their resonance frequencies were calculated numerically and suitable antennas fabricated. We remark at this point, that a meaningful quantification of the Purcell emission enhancement induced by the coupling can in principle be achieved via intensity saturation measurements. By measuring the saturation intensities before and after insertion into the antenna and accounting for effects related to the polarization of emitters, the magnitude of the Purcell enhancement can be determined. Unfortunately, these methods are reserved for single emitters and do not apply for ensembles of SiV centers. Naturally, the odds of identifying and addressing a nanodiamond fulfilling all criteria simultaneously are small. As a result identifying a perfect candidate for coupling is prohibitively time-consuming.

To mitigate this difficulty we decided to relax the condition of exactly one SiV center per nanodiamond and initiate our exploratory work with nanodiamonds containing several, potentially many active SiV centers. Relying on $g^{(2)}$ function measurements we identify two interesting classes of nanodiamonds. The first class consists of nanodiamonds containing large ensembles of SiV centers acting as coherent emitters, which yield a flat response in the $g^{(2)}$ function. The second class of nanodiamonds we investigate features nanodiamonds hosting a small number of SiV centers. As a result relevant $g^{(2)}$ function measurements exhibit weak but discernible anti-bunching dips. Both classes have in common that relevant nanodiamond specimen are significantly easier to obtain than nanodiamonds containing single SiV centers. Thus nanodiamonds containing ensembles of SiV centers as well as nanodiamonds containing few SiV centers are both valid starting points for our exploration. To our knowledge, our experiments were the first attempts of coupling

SiV centers to plasmonic bowtie antennas.

We begin by selecting a suitable nanodiamond containing a large ensemble of SiV centers and measure its spectrum in isolation. Our measurements of the SiV centers hosted by a nanodiamond coupled to the double bowtie antenna agree very well with predictions from FDTD simulations, asserting successful coupling facilitated by the pick-and-place method. The remarkable agreement of the theoretical prediction and the experimentally recorded spectra for an ensemble of SiV centers in a nanodiamond make our simulation assisted approach very useful and a promising candidate for future explorations of antenna-emitter coupling.

Next we report our attempts to couple nanodiamonds hosting a limited number of SiV centers to plasmonic gold double bowtie antennas. Suitable nanodiamonds show an anti-bunching dip in the $g^{(2)}$ function in addition to count-rate saturation. This can be regarded an intermediate step towards using nanodiamonds containing single SiV centers.

Analogous to the process of coupling nanodiamonds with large ensembles of SiV centers, we begin by recording the spectrum of the nanodiamond in isolation. Next we relocate the nanodiamond in question to the center of the antenna using the pick-and-place method. Having assembled the integrated system, we record its spectrum in order to compare it with the simulation-assisted prediction focusing on dipole orientation effects. While some minor peaks of the measured spectrum can be associated with the simulation prediction, the major peaks seemed to have bleached.

While it is not possible to pinpoint exactly which circumstance caused the modification, several effects could influence the observed spectra. These include damage through electron radiation as well as additional fluorescing surface contaminations the nanodiamond might have picked up during the pick-and-place process. It also seems logical to assume that nanodiamonds containing only a few SiV centers are less resilient to radiation damage than nanodiamonds containing large ensembles of SiV centers. A property of SiV centers which should not be neglected is their dipole orientation interacting with the antenna. Conducting dedicated FDTD simulations with a focus on different dipole orientations indicated a dramatic effect on the resulting spectra. Therefore, future experiments aiming to investigate the effect of coupling nanodiamonds containing single SiV centers to antennas should include polarization measurements to experimentally quantify the impact of the emitter orientation.

Finally, we want to take a step back and discuss our results regarding SiV centers in the context of the quest for reliable on-demand single photon sources. One of the properties that make SiV centers interesting single photon sources for the purpose of calibrating detectors is their narrow linewidth zero-phonon-line. Since detectors may have different sensitivity at different wavelengths, the actual wavelength of the zero-phonon-line can become important. The preselection of emitters is an extremely tedious and time consuming process, in particular when nanodiamonds are required that contain a single SiV center. However, we showed that it is possible to preselect emitters according to their optical properties, and that candidate nanodiamonds tailored to a particular application can be found. In particular, the existence of group H containing emitters with zero-phonon-lines of various wavelengths is interesting. An analogous argument is true for group V with regards to the center wavelength of emitters.

In addition to questions of applications, our results regarding the distribution of SiV center properties raise further fundamental questions. While a consistent explanation of the data in group H is still missing, we managed to tie the observed variety of the emitters in group V to varying strain in the nanodiamonds.

In our work we also explored the possibility of combining nanodiamonds containing SiV centers with other nano-structures in order to create a hybrid-integrated single photon source. To this end we utilize pick-and-place methods to relocate selected nanodiamonds to target structures. Coupling nanodiamonds to VCSELs is a promising approach to create a single photon source which is controlled via the operation of the VCSELs. In our work we demonstrated the first steps towards this goal. While we also identified the first roadblock preventing us from realizing a functioning hybrid integrated single photon source for now, a promising approach to overcome the persisting challenges was suggested.

While coupling SiV centers to VCSELs was aimed at increasing the control over the resulting single photon source, coupling to antennas aims at changing the spectroscopic properties of the emitters via their interaction with the antenna. Here we managed to demonstrate successful coupling of a nanodiamond containing an ensemble of SiV centers and an antenna. While at this point we were not able to properly quantify the enhancement emitters experience through the coupling, the combination of numerical FDTD simulations and experimental methods has been established as a valuable method to predict the emission of the coupled system. Thus we recommend this method to be incorporated in future attempts of coupling SiV centers to antennas to create enhanced single photon sources.

In conclusion, our research aims to contribute to the development of reliable on-demand single photon sources based on SiV centers in nanodiamonds in two major ways. First, we establish properties of SiV centers over large sample sets of nanodiamonds. In doing so, we add to the understanding of this type of color center with the intention of subsequently improving our abilities to use SiV centers as constituents of integrated single photon sources. To proceed in this direction we use individual nanodiamonds and couple their hosted SiV centers to various nanostructures. We demonstrate successful coupling and identify valuable suggestions for further research. Our contributions add momentum to the development of single photon sources, to the development of novel calibration standards and photon detectors and ultimately, to the universal adoption of the quantum candela.

Bibliography

[1] Bureau International des Poids et Mesures, *SI Brochure: The International System of Units (SI)*, Accessed: 2018-05-30, 2014.

[2] P. W. Petley, "The atomic units, the kilogram and the other proposed changes to the si", *Metrologia*, vol. 44, p. 69, 2007.

[3] M. Milton, *Highlights in the work of the BIPM during 2017*, Accessed: 2018-05-30, 2017.

[4] J. C. Zwinkels, E. Ikonen, N. P. Fox, *et al.*, "Photometry, radiometry and the candela: Evolution in the classical and quantum world", *Metrologia*, vol. 47, R15, 2010.

[5] J. Y. Cheung, C. J. Chunnilall, E. R. Woolliams, *et al.*, "The quantum candela: a re-definition of the standard units for optical radiation", *Journal of modern optics*, vol. 54, pp. 373–396, 2007.

[6] N. P. Fox and J. P. Rice, "Absolute radiometers", *Optical radiometry. series: Experimental methods in the physical sciences*, vol. 41, pp. 35–96, 2005.

[7] *Qu-candela project, iMERA programme*, Accessed: 2018-05-30, 2011.

[8] Bureau International des Poids et Mesures, *On the future revision of the SI*, Accessed: 2018-05-30, 2014.

[9] G. Buller and R. Collins, "Single-photon generation and detection", *Measurement science and technology*, vol. 21, p. 012 002, 2009.

[10] M. Eisaman, J. Fan, A. Migdall, *et al.*, "Invited review article: Single-photon sources and detectors", *Review of scientific instruments*, vol. 82, 2011.

[11] N. Sangouard and H. Zbinden, "What are single photons good for?", *Journal of modern optics*, vol. 59, pp. 1458–1464, 2012.

[12] C. J. Chunnilall, I. P. Degiovanni, S. Kück, *et al.*, "Metrology of single-photon sources and detectors: A review", *Optical engineering*, vol. 53, p. 081 910, 2014.

[13] *JRP EXL02 - SIQUTE, EURAMET programme*, Accessed: 2018-05-30, 2012.

[14] S. Scheel, "Single-photon sources - An introduction", *Journal of modern optics*, vol. 56, pp. 141–160, 2009.

[15] C. H. Bennett and G. Brassard, "Quantum cryptography: Public key distribution and coin tossing.", *Theor. comput. sci.*, vol. 560, pp. 7–11, 2014.

[16] A. Beveratos, R. Brouri, T. Gacoin, *et al.*, “Single photon quantum cryptography”, *Physical review letters*, vol. 89, p. 187 901, 2002.

[17] R. Alléaume, F. Treussart, G. Messin, *et al.*, “Experimental open-air quantum key distribution with a single-photon source”, *New journal of physics*, vol. 6, p. 92, 2004.

[18] L. Childress, J. Taylor, A. S. Sørensen, *et al.*, “Fault-tolerant quantum communication based on solid-state photon emitters”, *Physical review letters*, vol. 96, p. 070 504, 2006.

[19] H. Bernien, L. Childress, L. Robledo, *et al.*, “Two-photon quantum interference from separate nitrogen vacancy centers in diamond”, *Physical review letters*, vol. 108, p. 043 604, 2012.

[20] W. Pfaff, B. Hensen, H. Bernien, *et al.*, “Unconditional quantum teleportation between distant solid-state quantum bits”, *Science*, vol. 345, pp. 532–535, 2014.

[21] N. Gisin, G. Ribordy, W. Tittel, *et al.*, “Quantum cryptography”, *Reviews of modern physics*, vol. 74, p. 145, 2002.

[22] A. Migdall, S. V. Polyakov, J. Fan, *et al.*, *Single-photon generation and detection: Physics and applications*. Academic Press, 2013, vol. 45.

[23] Y. Shih, “Entangled biphoton source-property and preparation”, *Reports on progress in physics*, vol. 66, p. 1009, 2003.

[24] D. Klyshko, “Utilization of vacuum fluctuations as an optical brightness standard”, *Soviet journal of quantum electronics*, vol. 7, p. 591, 1977.

[25] S. Fasel, O. Alibart, S. Tanzilli, *et al.*, “High-quality asynchronous heralded single-photon source at telecom wavelength”, *New journal of physics*, vol. 6, p. 163, 2004.

[26] M. Ware and A. Migdall, “Single-photon detector characterization using correlated photons: The march from feasibility to metrology”, *Journal of modern optics*, vol. 51, pp. 1549–1557, 2004.

[27] G. Brida, I. Degiovanni, M. Genovese, *et al.*, “An extremely low-noise heralded single-photon source: A breakthrough for quantum technologies”, *Applied physics letters*, vol. 101, p. 221 112, 2012.

[28] M. Bock, A. Lenhard, C. Chunnilall, *et al.*, “Highly efficient heralded single-photon source for telecom wavelengths based on a PPLN waveguide”, *Optics express*, vol. 24, p. 23 992, 2016.

[29] J. Řeháček, Z. Hradil, O. Haderka, *et al.*, “Multiple-photon resolving fiber-loop detector”, *Physical review A*, vol. 67, p. 061 801, 2003.

[30] G. Brida, I. P. Degiovanni, M. Genovese, *et al.*, “Experimental test of nonclassicality for a single particle”, *Optics express*, vol. 16, pp. 11 750–11 758, 2008.

[31] A. Kuhn, M. Hennrich, and G. Rempe, “Deterministic Single-Photon Source for Distributed Quantum Networking”, *Physical review letters*, vol. 89, pp. 4–7, 2002.

[32] J. C. Loredo, N. A. Zakaria, N. Somaschi, *et al.*, “Scalable performance in solid-state single-photon sources”, *Optica*, vol. 3, pp. 433–440, 2016.

[33] N. Somaschi, V. Giesz, L. De Santis, *et al.*, “Near-optimal single-photon sources in the solid state”, *Nature photonics*, vol. 10, p. 340, 2016.

[34] I. Aharonovich, D. Englund, and M. Toth, “Solid-state single-photon emitters”, *Nature photonics*, vol. 10, pp. 631–641, 2016.

[35] Z. Yuan, B. E. Kardynal, R. M. Stevenson, *et al.*, “Electrically driven single-photon source.”, *Science*, vol. 295, pp. 102–5, 2002.

[36] S. Buckley, K. Rivoire, and J. Vučković, “Engineered quantum dot single-photon sources”, *Reports on progress in physics*, vol. 75, p. 126 503, 2012.

[37] K. Lee, X. Chen, H. Eghlidi, *et al.*, “A planar dielectric antenna for directional single-photon emission and near-unity collection efficiency”, *Nature photonics*, vol. 5, p. 166, 2011.

[38] X.-W. Chen, S. Götzinger, and V. Sandoghdar, “99% efficiency in collecting photons from a single emitter”, *Optics letters*, vol. 36, pp. 3545–3547, 2011.

[39] S. Ates, I. Agha, A. Gulinatti, *et al.*, “Improving the performance of bright quantum dot single photon sources using temporal filtering via amplitude modulation”, *Scientific reports*, vol. 3, p. 1397, 2013.

[40] X. Ding, Y. He, Z.-C. Duan, *et al.*, “On-demand single photons with high extraction efficiency and near-unity indistinguishability from a resonantly driven quantum dot in a micropillar”, *Phys. rev. lett.*, vol. 116, p. 020 401, 2016.

[41] A. Vaigu, G. Porrovecchio, X. L. Chu, *et al.*, “Experimental demonstration of a predictable single photon source with variable photon flux”, *Metrologia*, vol. 54, pp. 218–223, 2017.

[42] E. Neu, M. Agio, and C. Becher, “Photophysics of single silicon vacancy centers in diamond: Implications for single photon emission”, *Optics express*, vol. 20, pp. 19 956–19 971, 2012.

[43] E. Neu, R. Albrecht, M. Fischer, *et al.*, “Electronic transitions of single silicon vacancy centers in the near-infrared spectral region”, *Physical review B*, vol. 85, p. 245 207, 2012.

[44] M. W. Doherty, N. B. Manson, P. Delaney, *et al.*, “The nitrogen-vacancy colour centre in diamond”, *Physics reports*, vol. 528, pp. 1–45, 2013.

[45] B. Rodiek, M. Lopez, H. Hofer, *et al.*, “Experimental realization of an absolute single-photon source based on a single nitrogen vacancy center in a nanodiamond”, *Optica*, vol. 4, p. 71, 2017.

[46] S. Lindner, A. Bommer, A. Muzha, *et al.*, "Strongly inhomogeneous distribution of spectral properties of silicon-vacancy color centers in nanodiamonds", *New journal of physics*, vol. 20, p. 115 002, 2018.

[47] J. S. Riedrich-Möller, "Deterministic coupling of single color centers to monolithic photonic crystal cavities in single crystal diamond", PhD thesis, Saarland University, Saarbrücken, Germany, 2014.

[48] E. K. Neu, "Silicon vacancy color centers in chemical vapor deposition diamond: New insights into promising solid state single photon sources", PhD thesis, Saarland University, Saarbrücken, Germany, 2012.

[49] J. N. Becker, "Silicon vacancy colour centres in diamond: Coherence properties and quantum control", PhD thesis, Universität des Saarlandes, 2017.

[50] D. Steinmetz, "Ni/Si-basierte Farbzentren in Diamant als Einzelphotonenquellen Dissertation", PhD thesis, Saarland University, Saarbrücken, Germany, 2011.

[51] C. Hepp, "Electronic structure of the silicon vacancy color center in diamond", PhD thesis, Universität des Saarlandes, 2014.

[52] F. P. Bundy, "Pressure-temperature phase diagram of elemental carbon", *Physica A: Statistical mechanics and its applications*, vol. 156, pp. 169–178, 1989.

[53] R. Telling, C. Pickard, M. Payne, *et al.*, "Theoretical strength and cleavage of diamond", *Physical review letters*, vol. 84, p. 5160, 2000.

[54] T. Saotome, K. Ohashi, T. Sato, *et al.*, "Thermal expansion of a boron-doped diamond single crystal at low temperatures", *Journal of physics: Condensed matter*, vol. 10, pp. 1267–1272, 1998.

[55] W. Demtröder, *Experimentalphysik 3: Atome, Moleküle und Festkörper.* Springer Verlag, 2000.

[56] C. D. Clark, P. J. Dean, and P. V. Harris, "Intrinsic Edge Absorption in Diamond", *Proceedings of the royal society A: Mathematical, physical and engineering sciences*, vol. 277, pp. 312–329, 1964.

[57] W. Saslow, T. K. Bergstresse, and M. L. Cohen, "Band structure and optical properties of diamond", *Physical review letters*, vol. 16, pp. 354–356, 1966.

[58] R. P. Mildren, J. E. Butler, and J. R. Rabeau, "CVD-diamond external cavity Raman laser at 573 nm", *Optics express*, vol. 16, p. 18 950, 2008.

[59] A. M. Zaitsev, *Optical properties of diamond: A data handbook.* Springer Science & Business Media, 2013.

[60] A. Beveratos, R. Brouri, T. Gacoin, *et al.*, "Nonclassical radiation from diamond nanocrystals", *Physical review A*, vol. 64, p. 61 802, 2001.

[61] W. Kaiser and W. L. Bond, "Nitrogen, a major impurity in common type I diamond", *Physical review*, vol. 115, pp. 857–863, 1959.

[62] C. M. Breeding and J. E. Shigley, “The type classification system of diamonds and its importance in gemology”, *Gems & Gemology*, vol. 45, pp. 96–111, 2009.

[63] J. Walker and J. Walkert, “Optical absorption and luminescence in diamond”, *Rep. prog. phys.*, vol. 42, pp. 1606–1659, 1979.

[64] B. Massarani, J. C. Bourgoin, and R. M. Chrenko, “Hopping conduction in semiconducting diamond”, *Physical review B*, vol. 17, pp. 1758–1769, 1978.

[65] M. L. Markham, J. M. Dodson, G. A. Scarsbrook, *et al.*, “CVD diamond for spintronics”, *Diamond and related materials*, vol. 20, pp. 134–139, 2011.

[66] G. Balasubramanian, P. Neumann, D. Twitchen, *et al.*, “Ultralong spin coherence time in isotopically engineered diamond”, *Nature materials*, vol. 8, pp. 383–387, 2009.

[67] P. W. May, “Diamond thin films: a 21st-century material”, *Philosophical transactions of the royal society A: Mathematical, physical and engineering sciences*, vol. 358, pp. 473–495, 2000.

[68] M. Keller, B. Lange, K. Hayasaka, *et al.*, “Continuous generation of single photons with controlled waveform in an ion-trap cavity system”, *Nature*, vol. 431, pp. 1075–1078, 2004.

[69] P. Michler, A. Kiraz, C. Becher, *et al.*, “A quantum dot single-photon turnstile device.”, *Science*, vol. 290, pp. 2282–5, 2000.

[70] B. Lounis and M. Orrit, “Single-photon sources”, *Reports on progress in physics*, vol. 68, pp. 1129–1179, 2005.

[71] T. A. Kennedy, J. S. Colton, J. E. Butler, *et al.*, “Long coherence times at 300 K for nitrogen-vacancy center spins in diamond grown by chemical vapor deposition”, *Applied physics letters*, vol. 83, pp. 4190–4192, 2003.

[72] A. D. Greentree, B. A. Fairchild, F. M. Hossain, *et al.*, “Diamond integrated quantum photonics”, *Materials today*, vol. 11, pp. 22–31, 2008.

[73] I. Aharonovich and E. Neu, “Diamond nanophotonics”, *Advanced optical materials*, vol. 2, pp. 911–928, 2014.

[74] S. Prawer and I. Aharonovich, *Quantum information processing with diamond: Principles and applications.* Woodhead Publishing, 2014, p. 367.

[75] N. B. Manson, J. P. Harrison, and M. J. Sellars, “Nitrogen-vacancy center in diamond: Model of the electronic structure and associated dynamics”, *Physical review B - condensed matter and materials physics*, vol. 74, pp. 1–11, 2006.

[76] F. Jelezko, I. Popa, A. Gruber, *et al.*, “Single spin states in a defect center resolved by optical spectroscopy”, *Applied physics letters*, vol. 81, pp. 2160–2162, 2002.

[77] C. Santori, D. Fattal, S. M. Spillane, *et al.*, “Coherent population trapping in diamond N-V centers at zero magnetic field”, *CLEO/QELS 2006*, vol. 14, pp. 7986–7994, 2006.

[78] A. Sipahigil, K. D. Jahnke, L. J. Rogers, *et al.*, “Indistinguishable Photons from Separated Silicon-Vacancy Centers in Diamond”, *Physical review letters*, vol. 113, p. 113 602, 2014.

[79] T. Müller, C. Hepp, B. Pingault, *et al.*, “Optical signatures of silicon-vacancy spins in diamond”, *Nature communications*, vol. 5, p. 3328, 2014.

[80] B. Pingault, J. N. Becker, C. H. H. Schulte, *et al.*, “All-Optical Formation of Coherent Dark States of Silicon-Vacancy Spins in Diamond”, *Physical review letters*, vol. 113, p. 263 601, 2014.

[81] L. J. Rogers, K. D. Jahnke, M. H. Metsch, *et al.*, “All-optical initialization, readout, and coherent preparation of single silicon-vacancy spins in diamond”, *Physical review letters*, vol. 113, p. 263 602, 2014.

[82] J. P. Goss, P. R. Briddon, and M. J. Shaw, “Density functional simulations of silicon-containing point defects in diamond”, *Physical review B - condensed matter and materials physics*, vol. 76, p. 075 204, 2007.

[83] U. F. S. D’Haenens-Johansson, a. M. Edmonds, B. L. Green, *et al.*, “Optical properties of the neutral silicon split-vacancy center in diamond”, *Physical review B*, vol. 84, p. 245 208, 2011.

[84] C. Hepp, T. Müller, V. Waselowski, *et al.*, “Electronic Structure of the Silicon Vacancy Color Center in Diamond”, *Physical review letters*, vol. 112, p. 036 405, 2014.

[85] E. Neu, D. Steinmetz, J. Riedrich-Möller, *et al.*, “Single photon emission from silicon-vacancy colour centres in chemical vapour deposition nano-diamonds on iridium”, *New journal of physics*, vol. 13, p. 25 012, 2011.

[86] A. Collins, M. Thomaz, and M. I. B. Jorge, “Luminescence decay time of the 1.945 ev centre in type ib diamond”, *Journal of physics c: Solid state physics*, vol. 16, p. 2177, 1983.

[87] A. Gali and J. R. Maze, “Ab initio study of the split silicon-vacancy defect in diamond: Electronic structure and related properties”, *Physical review B - condensed matter and materials physics*, vol. 88, p. 235 205, 2013.

[88] K. Iakoubovskii, G. Adriaenssens, N. Dogadkin, *et al.*, “Optical characterization of some irradiation-induced centers in diamond”, *Diamond and related materials*, vol. 10, pp. 18–26, 2001.

[89] K. Iakoubovskii and G. Adriaenssens, “Optical detection of defect centers in CVD diamond”, *Diamond and related materials*, vol. 9, pp. 1349–1356, 2000.

[90] M. C. Rossi, S. Salvatori, F. Galluzzi, *et al.*, “Emission and excitation spectra of silicon-related luminescent centers in CVD-grown diamond films”, *Diamond and related materials*, vol. 6, pp. 1564–1567, 1997.

[91] T. Müller, I. Aharonovich, L. Lombez, *et al.*, “Wide-range electrical tunability of single-photon emission from chromium-based colour centres in diamond”, *New journal of physics*, vol. 13, p. 075 001, 2011.

[92] P. Siyushev, V. Jacques, I. Aharonovich, *et al.*, “Low-temperature optical characterization of a near-infrared single-photon emitter in nanodiamonds”, *New journal of physics*, vol. 11, p. 113 029, 2009.

[93] K. Iakoubovskii, “Optical Study of Defects in Diamond”, PhD thesis, Katholieke Universiteit Leuven, Leuven, Netherlands, 2000.

[94] T. Feng and B. D. Schwartz, “Characteristics and origin of the 1.681 ev luminescence center in chemical-vapor-deposited diamond films”, *Journal of applied physics*, vol. 73, pp. 1415–1425, 1993.

[95] G. Davies, “The Jahn-Teller effect and vibronic coupling at deep levels in diamond”, *Reports on progress in physics*, vol. 44, pp. 787–830, 1981.

[96] A. M. Zaitsev, “Vibronic spectra of impurity-related optical centers in diamond”, *Physical review B*, vol. 61, pp. 12 909–12 922, 2000.

[97] S. A. Solin and A. K. Ramdas, “Raman Spectrum of Diamond”, *Physical review B*, vol. 1, pp. 1687–1698, 1970.

[98] M. H. Grimsditch, E. Anastassakis, and M. Cardona, “Effect of uniaxial stress on the zone-center optical phonon of diamond”, *Physical review B*, vol. 18, pp. 901–904, 1978.

[99] H. Sternschulte, K. Thonke, R. Sauer, *et al.*, “1.681-eV luminescence center in chemical-vapor-deposited homoepitaxial diamond films”, *Physical review B*, vol. 50, pp. 14 554–14 560, 1994.

[100] B. Huttner, N. Imoto, N. Gisin, *et al.*, “Quantum cryptography with coherent states”, *Physical review A*, vol. 51, pp. 1863–1869, 1995.

[101] E. Condon, “The franck-condon principle and related topics”, *American journal of physics*, vol. 15, pp. 365–374, 1947.

[102] J. L. Duligall, M. S. Godfrey, K. A. Harrison, *et al.*, “Low cost and compact quantum key distribution”, *New journal of physics*, vol. 8, p. 249, 2006.

[103] M. Nothaft, S. Höhla, F. Jelezko, *et al.*, “Electrically driven photon antibunching from a single molecule at room temperature”, *Nature communications*, vol. 3, p. 628, 2012.

[104] E. Neu, C. Hepp, M. Hauschild, *et al.*, “Low-temperature investigations of single silicon vacancy colour centres in diamond”, *New journal of physics*, vol. 15, p. 043 005, 2013.

[105] C. D. Clark, H. Kanda, I. Kiflawi, *et al.*, “Silicon defects in diamond”, *Phys. rev. b*, vol. 51, pp. 16 681–16 688, 1995.

[106] L. J. Rogers, K. D. Jahnke, T. Teraji, *et al.*, “Multiple intrinsically identical single-photon emitters in the solid state.”, *Nature communications*, vol. 5, p. 4739, 2014.

[107] A. Dietrich, K. D. Jahnke, J. M. Binder, *et al.*, “Isotopically varying spectral features of silicon-vacancy in diamond”, *New journal of physics*, vol. 16, p. 113 019, 2014.

[108] R. H. Webb, “Confocal optical microscopy”, *Reports on progress in physics*, vol. 59, p. 427, 1996.

[109] C. Santori, D. Fattal, and Y. Yamamoto, *Single-photon devices and applications*. Wiley-VCH, 2010, p. 223.

[110] R. H. Brown and R. Q. Twiss, “Correlation between photons in two coherent beams of light”, *Nature*, vol. 177, pp. 27–29, 1956.

[111] R. H. Brown and R. Twiss, “A test of a new type of stellar interferometer on sirius”, *Nature*, vol. 178, pp. 1046–1048, 1956.

[112] A. M. Fox, *Quantum optics: An introduction*. Oxford University Press, 2006, p. 378.

[113] N. Rahbany, “Towards integrated optics at the nanoscale: Plasmon-emitter coupling using plasmonic structures”, PhD thesis, Troyes, France, 2016.

[114] R. D. Younger, K. A. McIntosh, J. W. Chludzinski, *et al.*, “Crosstalk analysis of integrated Geiger-mode avalanche photodiode focal plane arrays”, *Advanced photon counting techniques III*, vol. 7320, 2009.

[115] R. F. Davis, *Diamond films and coatings: Development, properties, and applications*. Noyes Pub., 1993.

[116] H. Liander and E. Lundblad, “Artificial diamonds”, *Asea Journal*, vol. 28, pp. 97–98, 1955.

[117] F. Bundy, H. T. Hall, H. Strong, *et al.*, “Man-made diamonds”, *Nature*, vol. 176, p. 51, 1955.

[118] H. Bovenkerk, F. Bundy, R. Chrenko, *et al.*, “Errors in diamond synthesis”, *Nature*, vol. 365, p. 19, 1993.

[119] H. Bovenkerk, F. Bundy, H. Hall, *et al.*, “Preparation of diamond”, *Nature*, vol. 184, p. 1094, 1959.

[120] M. Schwander and K. Partes, “A review of diamond synthesis by CVD processes”, *Diamond and related materials*, vol. 20, pp. 1287–1301, 2011.

[121] R. Balmer, J. Brandon, S. Clewes, *et al.*, “Chemical vapour deposition synthetic diamond: Materials, technology and applications”, *Journal of physics: Condensed matter*, vol. 21, p. 364 221, 2009.

[122] S. Ferro, “Synthesis of diamond”, *Journal of materials chemistry*, vol. 12, pp. 2843–2855, 2002.

[123] S. Koizumi, C. Nebel, and M. Nesladek, *Physics and applications of cvd diamond*. John Wiley & Sons, 2008.

[124] T. Tachibana, Y. Yokota, K. Hayashi, *et al.*, "Growth of {111}-oriented diamond on pt/ir/pt substrate deposited on sapphire", *Diamond and related materials*, vol. 10, pp. 1633–1636, 2001.

[125] P. Lin-Chung, "Local vibrational modes of impurities in diamond", *Physical review B*, vol. 50, p. 16 905, 1994.

[126] J. W. Arblaster, "Crystallographic Properties of Iridium", *Platinum metals review*, vol. 54, pp. 93–102, 2010.

[127] S. Gsell, M. Fischer, R. Brescia, *et al.*, "Reduction of mosaic spread using iridium interlayers: A route to improved oxide heteroepitaxy on silicon", *Applied physics letters*, vol. 91, p. 061 501, 2007.

[128] S. Gsell, T. Bauer, J. Goldfuß, *et al.*, "A route to diamond wafers by epitaxial deposition on silicon via iridium/yttria-stabilized zirconia buffer layers", *Applied physics letters*, vol. 84, p. 4541, 2004.

[129] O. A. Williams and M. Nesládek, "Growth and properties of nanocrystalline diamond films", *Phys. status solidi*, vol. 203, pp. 3375–3386, 2006.

[130] J. Robertson, "Diamond-like amorphous carbon", *Materials science and engineering reports*, vol. 37, pp. 129–281, 2002.

[131] J. Robertson, "Advances in Physics Amorphous carbon", *Advances in physics*, vol. 35, pp. 317–374, 1986.

[132] S. Prawer and R. J. Nemanich, "Raman spectroscopy of diamond and doped diamond", *Philosophical transactions of the royal society A: Mathematical, physical and engineering sciences*, vol. 362, pp. 2537–2565, 2004.

[133] J. O. Orwa, K. W. Nugent, D. N. Jamieson, *et al.*, "Raman investigation of damage caused by deep ion implantation in diamond", *Physical review B - condensed matter and materials physics*, vol. 62, pp. 5461–5472, 2000.

[134] I. Ford, "Model of the Competitive Growth of Amorphous-Carbon and Diamond Films", vol. 78, pp. 510–513, 1995.

[135] D. S. Olson, M. A. Kelly, S. Kapoor, *et al.*, "Sequential deposition of diamond from sputtered carbon and atomic hydrogen", *Journal of applied physics*, vol. 74, pp. 5167–5171, 1993.

[136] M. S. Dresselhaus and R. Kalish, *Ion Implantation in Diamond, Graphite and Related Materials*. Springer Berlin Heidelberg, 1992, vol. 22.

[137] A. C. Ferrari and J. Robertson, "Raman spectroscopy of amorphous, nanostructured, diamond–like carbon, and nanodiamond", *Philosophical transactions of the royal society of London A: Mathematical, physical and engineering sciences*, vol. 362, pp. 2477–2512, 2004.

[138] C. Widmann, W. Müller-Sebert, N. Lang, *et al.*, “Homoepitaxial growth of single crystalline CVD-diamond”, *Diamond and related materials*, vol. 64, pp. 1–7, 2016.

[139] E. J. D. Liscia, F. Álvarez, E. Burgos, *et al.*, “Stress Analysis on Single-Crystal Diamonds by Raman Spectroscopy 3D Mapping”, *Materials sciences and applications*, vol. 04, pp. 191–197, 2013.

[140] K. Bray, R. Sandstrom, C. Elbadawi, *et al.*, “Localization of narrowband single photon emitters in nanodiamonds”, *Acs applied materials & interfaces*, vol. 8, pp. 7590–7594, 2016.

[141] P. Zapol, M. Sternberg, L. A. Curtiss, *et al.*, “Tight-binding molecular-dynamics simulation of impurities in ultrananocrystalline diamond grain boundaries”, *Physical review B*, vol. 65, p. 045 403, 2001.

[142] C. Arend, J. N. Becker, H. Sternschulte, *et al.*, “Photoluminescence excitation and spectral hole burning spectroscopy of silicon vacancy centers in diamond”, *Physical review B*, vol. 94, p. 045 203, 2016.

[143] J. Benedikter, H. Kaupp, T. Hümmer, *et al.*, “Cavity-Enhanced Single-Photon Source Based on the Silicon-Vacancy Center in Diamond”, *Physical review Applied*, vol. 7, p. 024 031, 2017.

[144] E. Neu, C. Arend, E. Gross, *et al.*, “Narrowband fluorescent nanodiamonds produced from chemical vapor deposition films”, *Appl. phys. lett.*, vol. 98, p. 243 107, 2011.

[145] P. Deák, B. Aradi, M. Kaviani, *et al.*, “Formation of NV centers in diamond: A theoretical study based on calculated transitions and migration of nitrogen and vacancy related defects”, *Physical review B*, vol. 89, p. 075 203, 2014.

[146] M. Kaviani, P. Deák, B. Aradi, *et al.*, “Proper surface termination for luminescent near-surface NV centers in diamond”, *Nano letters*, vol. 14, pp. 4772–4777, 2014.

[147] G. Kresse and J. Hafner, “Ab initio molecular dynamics for liquid metals”, *Physical review B*, vol. 47, p. 558, 1993.

[148] G. Kresse and J. Furthmü"ller, “Efficiency of ab-initio total-energy calculations using a plane-wave basis set”, *Physical review B*, vol. 54, pp. 15–50, 1996.

[149] G. Kresse and J. Furthmüller, “Efficient iterative schemes for ab initio total-energy calculations using a plane-wave basis set”, *Physical review B*, vol. 54, p. 11 169, 1996.

[150] G. Kresse and D. Joubert, “From ultrasoft pseudopotentials to the projector augmented-wave method”, *Physical review B*, vol. 59, p. 1758, 1999.

[151] J. P. Perdew, K. Burke, and M. Ernzerhof, “Generalized gradient approximation made simple”, *Physical review letters*, vol. 77, p. 3865, 1996.

[152] A. Gali, E. Janzén, P. Deák, *et al.*, "Theory of spin-conserving excitation of the N - V(-) center in diamond", *Physical review letters*, vol. 103, p. 186 404, 2009.

[153] J. Heyd, G. E. Scuseria, and M. Ernzerhof, "Hybrid functionals based on a screened Coulomb potential", *The journal of chemical physics*, vol. 118, pp. 8207–8215, 2003.

[154] A. V. Krukau, O. A. Vydrov, A. F. Izmaylov, *et al.*, "Influence of the exchange screening parameter on the performance of screened hybrid functionals", *The journal of chemical physics*, vol. 125, p. 224 106, 2006.

[155] G. Henkelman, B. P. Uberuaga, and H. Jónsson, "A climbing image nudged elastic band method for finding saddle points and minimum energy paths", *The journal of chemical physics*, vol. 113, pp. 9901–9904, 2000.

[156] G. Thiering and A. Gali, "Ab initio magneto-optical spectrum of group-IV vacancy color centers in diamond", *Physical review X*, vol. 8, p. 021 063, 2018.

[157] P. Hess, "The mechanical properties of various chemical vapor deposition diamond structures compared to the ideal single crystal", *Journal of applied physics*, vol. 111, p. 3, 2012.

[158] O. A. Williams, A. Kriele, J. Hees, *et al.*, "High young's modulus in ultra thin nanocrystalline diamond", *Chemical physics letters*, vol. 495, pp. 84–89, 2010.

[159] G. Thiering and A. Gali, "Complexes of silicon, vacancy, and hydrogen in diamond: A density functional study", *Physical review B*, vol. 92, p. 165 203, 2015.

[160] K. D. Jahnke, A. Sipahigil, J. M. Binder, *et al.*, "Electron-phonon processes of the silicon-vacancy centre in diamond", *New journal of physics*, vol. 17, p. 43 011, 2015.

[161] E. Neu, M. Fischer, S. Gsell, *et al.*, "Fluorescence and polarization spectroscopy of single silicon vacancy centers in heteroepitaxial nanodiamonds on iridium", *Physical review B*, vol. 84, p. 205 211, 2011.

[162] F. P. Larkins and A. M. Stoneham, "Lattice distortion near vacancies in diamond and silicon", *Journal of physics C: Solid state physics*, vol. 4, pp. 143–153, 1971.

[163] E. Londero, G. Thiering, L. Razinkovas, *et al.*, "Vibrational modes of negatively charged silicon-vacancy centers in diamond from ab initio calculations", *Physical review B*, vol. 98, p. 035 306, 3 2018.

[164] K. M. Fu, C. Santori, P. E. Barclay, *et al.*, "Observation of the dynamic Jahn-Teller effect in the excited states of nitrogen-vacancy centers in diamond", *Physical review letters*, vol. 103, p. 256 404, 2009.

[165] U. Jantzen, A. B. Kurz, D. S. Rudnicki, *et al.*, "Nanodiamonds carrying silicon-vacancy quantum emitters with almost lifetime-limited linewidths", *New journal of physics*, vol. 18, p. 073 036, 2016.

[166] C. Bradac, T. Gaebel, N. Naidoo, *et al.*, "Observation and control of blinking nitrogen-vacancy centres in discrete nanodiamonds.", *Nature nanotechnology*, vol. 5, pp. 345–9, 2010.

[167] A. M. Berhane, C. Bradac, and I. Aharonovich, "Photoinduced blinking in a solid-state quantum system", *Physical review B*, vol. 96, p. 041 203, 2017.

[168] A. L. Efros and D. J. Nesbitt, "Origin and control of blinking in quantum dots", *Nature nanotechnology*, vol. 11, pp. 661–671, 2016.

[169] N. Z. Wong, A. F. Ogata, and K. L. Wustholz, "Dispersive Electron-Transfer Kinetics from Single Molecules on TiO 2 Nanoparticle Films", *The journal of physical chemistry C*, vol. 117, pp. 21 075–21 085, 2013.

[170] W. J. Albery, P. N. Bartlett, C. P. Wilde, *et al.*, "A general model for dispersed kinetics in heterogeneous systems", *Journal of the american chemical society*, vol. 107, pp. 1854–1858, 1985.

[171] A. W. Schell, G. Kewes, T. Schröder, *et al.*, "A scanning probe-based pick-and-place procedure for assembly of integrated quantum optical hybrid devices", *Review of scientific instruments*, vol. 82, p. 073 709, 2011.

[172] I. Melngailis, "Longitudinal injection-plasma laser of InSb", *Applied physics letters*, vol. 6, pp. 59–60, 1965.

[173] A. Ibaraki, S. Ishikawa, S. Ohkouchi, *et al.*, "Pulsed oscillation of GaAlAs-GaAs surface-emitting injection laser", *Electronics letters*, vol. 20, pp. 420–422, 1984.

[174] S. Weidenfeld, M. Wiesner, M. Eichfelder, *et al.*, "Beam profile and polarization characteristics of red VCSELs with oxide-defined aperture", *Annual report institut für halbleiteroptik und funktionelle grenzflächen*, pp. 34–35, 2009.

[175] S. Weidenfeld, H. Niederbracht, M. Eichfelder, *et al.*, "Transverse mode and polarization characteristics of AlGaInP-based VCSELs with integrated multiple oxide apertures", in *Proc. spie*, K. Panajotov, M. Sciamanna, A. Valle, *et al.*, Eds., vol. 8432, 2012, p. 843 205.

[176] P. Elens, Master's thesis, Saarland University, Saarbrücken, Germany, 2013.

[177] A. Meyer, *Einfluss von Elektronenstrahlung auf die Fluoreszenzeigenschaften von Silizium-Fehlstellen-Zentren in Diamant*, Bachelor's Thesis, Saarbrücken, Germany, 2014.

[178] A. Axelevitch, B. Gorenstein, and G. Golan, "Investigation of Optical Transmission in Thin Metal Films", *Physics procedia*, vol. 32, pp. 1–13, 2012.

[179] P. Bharadwaj, B. Deutsch, and L. Novotny, “Optical Antennas”, *Advances in optics and photonics*, vol. 1, p. 438, 2009.

[180] C. A. Ballanis, *Antenna theory analysis and design.* John Willey and Son’s Inc., New York, 1997.

[181] W. Ding, R. Bachelot, R. E. de Lamaestre, *et al.*, “Understanding near/far-field engineering of optical dimer antennas through geometry modification”, *Optics express*, vol. 17, pp. 21 228–21 239, 2009.

[182] A. G. Curto, G. Volpe, T. H. Taminiau, *et al.*, “Unidirectional emission of a quantum dot coupled to a nanoantenna.”, *Science*, vol. 329, pp. 930–933, 2010.

[183] T. Taminiau, F. Stefani, F. B. Segerink, *et al.*, “Optical antennas direct single-molecule emission”, *Nature photonics*, vol. 2, p. 234, 2008.

[184] T. H. Taminiau, F. D. Stefani, and N. F. van Hulst, “Enhanced directional excitation and emission of single emitters by a nano-optical yagi-uda antenna”, *Optics express*, vol. 16, pp. 10 858–10 866, 2008.

[185] T. H. Taminiau, F. Stefani, and N. F. van Hulst, “Single emitters coupled to plasmonic nano-antennas: Angular emission and collection efficiency”, *New journal of physics*, vol. 10, p. 105 005, 2008.

[186] S. Kühn, U. Håkanson, L. Rogobete, *et al.*, “Enhancement of single-molecule fluorescence using a gold nanoparticle as an optical nanoantenna”, *Physical review letters*, vol. 97, p. 017 402, 2006.

[187] O. Muskens, V. Giannini, J. Sanchez-Gil, *et al.*, “Strong enhancement of the radiative decay rate of emitters by single plasmonic nanoantennas”, *Nano letters*, vol. 7, pp. 2871–2875, 2007.

[188] M. Ringler, A. Schwemer, M. Wunderlich, *et al.*, “Shaping emission spectra of fluorescent molecules with single plasmonic nanoresonators”, *Physical review letters*, vol. 100, p. 203 002, 2008.

[189] F. Keilmann and R. Hillenbrand, “Near-field microscopy by elastic light scattering from a tip”, *Philosophical transactions-royal society of London series A mathematical physical and engineering sciences*, vol. 362, pp. 787–806, 2004.

[190] K. Kneipp, Y. Wang, H. Kneipp, *et al.*, “Single molecule detection using surface-enhanced raman scattering (SERS)”, *Physical review letters*, vol. 78, p. 1667, 1997.

[191] J. Martin, M. Kociak, Z. Mahfoud, *et al.*, “High-resolution imaging and spectroscopy of multipolar plasmonic resonances in aluminum nanoantennas”, *Nano letters*, vol. 14, pp. 5517–5523, 2014.

[192] E. M. Larsson, J. Alegret, M. Käll, *et al.*, “Sensing characteristics of NIR localized surface plasmon resonances in gold nanorings for application as ultrasensitive biosensors”, *Nano letters*, vol. 7, pp. 1256–1263, 2007.

[193] N. Rahbany, W. Geng, S. Blaize, *et al.*, “Integrated plasmonic double bowtie and ring grating structure for enhanced electric field confinement”, *Nanospectroscopy*, vol. 1, pp. 61–66, 2015.

[194] P. Ghenuche, S. Cherukulappurath, T. H. Taminiau, *et al.*, “Spectroscopic mode mapping of resonant plasmon nanoantennas”, *Physical review letters*, vol. 101, p. 116 805, 2008.

[195] E. M. Purcell, “Spontaneous emission probabilities at radio frequencies”, in *Confined electrons and photons*, vol. 340, Springer, 1995, pp. 839–839.

[196] A. Mohammadi, V. Sandoghdar, and M. Agio, “Gold nanorods and nanospheroids for enhancing spontaneous emission”, *New journal of physics*, vol. 10, p. 105 015, 2008.

[197] A. Mohammadi, F. Kaminski, V. Sandoghdar, *et al.*, “Fluorescence enhancement with the optical (bi-) conical antenna”, *The journal of physical chemistry c*, vol. 114, pp. 7372–7377, 2010.

[198] E. Wientjes, J. Renger, A. G. Curto, *et al.*, “Nanoantenna enhanced emission of light-harvesting complex 2: The role of resonance, polarization, and radiative and non-radiative rates”, *Physical chemistry chemical physics*, vol. 16, pp. 24 739–24 746, 2014.

[199] R. Pease, “Electron beam lithography”, *Contemporary physics*, vol. 22, pp. 265–290, 1981.

[200] G. Ghosh, *Handbook of optical constants of solids: Handbook of thermo-optic coefficients of optical materials with applications*. Academic Press, 1998.

[201] J. Riedrich-Möller, C. Arend, C. Pauly, *et al.*, “Deterministic coupling of a single silicon-vacancy color center to a photonic crystal cavity in diamond.”, *Nano letters*, vol. 14, pp. 5281–7, 2014.

[202] J. C. Lee, I. Aharonovich, A. P. Magyar, *et al.*, “Coupling of silicon-vacancy centers to a single crystal diamond cavity”, *Optics express*, vol. 20, pp. 8891–8897, 2012.

[203] S. Orlanducci, I. Cianchetta, E. Tamburri, *et al.*, “Effects of au nanoparticles on photoluminescence emission from si-vacancy in diamond”, *Chemical physics letters*, vol. 549, pp. 51–57, 2012.

[204] J. Hadden, J. Harrison, A. Stanley-Clarke, *et al.*, “Strongly enhanced photon collection from diamond defect centers under microfabricated integrated solid immersion lenses”, *Applied physics letters*, vol. 97, p. 241 901, 2010.